Bralower, T.J., Premoli Silva, I., Malone, M.J., et al., 2002
Proceedings of the Ocean Drilling Program, Initial Reports Volume 198

9. SITE 1213[1]

Shipboard Scientific Party[2]

PRINCIPAL RESULTS

Background

Site 1213 is the southernmost and deepest site on the Shatsky Rise depth transect, located in lower bathyal (3883 m) water depth on the southern flank of the Southern High of Shatsky Rise. The site is close to the oldest part of the rise with underlying basement formed in the Tithonian (Late Jurassic). The major goals of Site 1213 drilling were to core a relatively deepwater mid- (Barremian–Cenomanian) and Lower Cretaceous sequence as well as to obtain fresh volcanic rocks from the underlying basement. The correlation of seismic lines down the southern flank of Shatsky Rise suggested that a relatively thick mid- and Lower Cretaceous section exists at a relatively shallow burial depth (Fig. **F1**; see line 17B in oversized Figure **F8**, p. 14, in Klaus and Sager, this volume). Basement was thought to lie between 400 and 600 meters below seafloor (mbsf), depending on velocity estimates. Thus the lower part of the Cretaceous section and basement can be recovered without time-consuming drilling through extensive chalk/ooze-chert sequences.

F1. Interpretation of seismic reflection across Site 1213, p. 40.

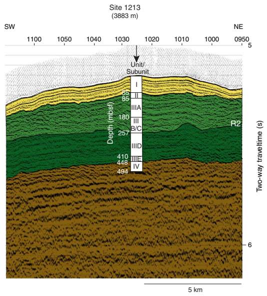

Holes 1213A and 1213B were cored with the rotary core barrel (RCB). Hole 1213A was terminated at 198.9 mbsf after the coring wireline parted. The lithology at the base of this hole consists of chert, porcellanite, and radiolarite of middle Albian age. A total of 447.8 m of sedimentary rock was penetrated in Hole 1213B, with claystones near the base of the hole containing nannofossils and radiolarians of earliest Berriasian age. Core recovery in chert-bearing units was low. Underlying the sedimentary package, plutonic rocks totaling 46.6 m in thickness were penetrated, and higher recovery was obtained than in the sedimentary sequence. Hole 1213B was terminated when the rate of penetration decreased significantly and the recovered material was considered sufficiently unaltered for detailed geochemical and radiometric

---

[1] Examples of how to reference the whole or part of this volume.
[2] Shipboard Scientific Party addresses.

Ms 197IR-109

analyses. Finally, a full suite of logs was to be collected through the whole sequence. The triple combination (triple combo) tool reached 431 mbsf but experienced several tight passes in the hole. With the approach of severe tropical storm Krosa combined with the poor hole conditions, it was considered too risky to deploy the Formation MicroScanner (FMS)-sonic logging tool.

Summary of Results

Coring at Site 1213 recovered four lithologic units. Sedimentary units are divided based on composition and color. Lithologic Unit I (0–54.6 mbsf) consists of olive-gray to pale yellowish brown nannofossil ooze, clayey nannofossil ooze, and nannofossil clay that ranges from the Holocene to lower Pliocene (0–5.0 Ma). This unit contains minor amounts of diatoms, foraminifers, and ash. Subunit IIA (54.6–66.1 mbsf) comprises pale orange nannofossil ooze and brown chert of Santonian age (84.8–85.5 Ma). Moderate to pale yellow-brown chert and light brown and pale orange porcellanite of middle to late Cenomanian age (94.1–96.8 Ma) are grouped in Subunit IIB (66.1–85.4 mbsf).

Subunit IIIA (85.4–179.6 mbsf) of early Cenomanian to middle Albian age (96.8–106 Ma) contains medium dark gray chert, gray, greenish gray, and pale orange porcellanite, and light greenish gray limestone. A mixture of chert, shades of brown and red in color, and pale orange to gray-orange and pale yellow-brown porcellanite and radiolarite with an age range from early middle Albian to late Aptian (106–119.5 Ma) are grouped in Subunit IIIB (179.6–256.8 mbsf). Subunit IIIC (256.8–266.4 mbsf) corresponds to olive-black to greenish black organic carbon–rich (C_{org}-rich) clayey porcellanite, dusky green radiolarian porcellanite, and minor altered tuff. This unit is early Aptian in age (119.5–120.5 Ma). Gray chert, white to yellowish gray porcellanite, and light greenish gray and olive-gray nannofossil chalk to clayey nannofossil chalk of Hauterivian to late Berriasian age constitute Subunit IIID (266.4–410.3 mbsf). Subunit IIIE (410.3–447.8 mbsf) of late Berriasian to earliest Berriasian age contains brown, gray, grayish red, and pale to moderate brown chert, yellowish gray and light pale orange porcellanite, and brown claystone with nannofossils. A limonitic claystone breccia is found at the base of this subunit. Throughout the sedimentary section, porcellanite, limestone, and claystone have variable amounts of radiolarians and nannofossils. In many intervals nannofossil biostratigraphy was conducted on chalk adhered to the sides of chert nodules. This sediment indicates the nature of the unrecovered intervals. Finally, Unit IV (447.8–494.4 mbsf) contains at least three separate units of dark greenish gray, sparsely phyric or fine-grained diabase with chilled basaltic margins and thin interbedded pieces of altered chert.

Preliminary investigations of the almost 500-m cored sequence at Site 1213 yields a detailed 140-m.y. history of the deep south flank of Shatsky Rise. The record from this site provides a new perspective to the evolution of the plateau. True basaltic basement was not recovered at this site; instead, we cored a sequence of diabase units with chilled margins and interbedded sediment that are interpreted as sills intruded during a widespread posteruptive plutonic event. Limonitic breccias overlie these intrusives, providing evidence for hydrothermal activity associated with sill intrusion. The earliest sediments of pelagic origin are radiolarian-rich horizons that were deposited under high-productivity surface water conditions in well-aerated deep waters that were swept by currents. These sediments have been transformed during burial to porcellanite and chert. At times, lower productivity conditions led to deposition of nannofossil ooze, which is now chalk in the deep record.

The early history of Shatsky Rise was interrupted by separate intervals of dysoxia/anoxia in the Valanginian and early Aptian that led to deposition of C_{org}-rich sediments. Evidence for the Valanginian event is found in southern Europe (Lini et al., 1992). To our knowledge, however, this is the first record of this event in the Pacific Ocean as well as in the pelagic realm. C_{org}-rich sediments deposited during the well-known Aptian Oceanic Anoxic Event (OAE1a) were also found at Site 1207 on the Northern High.

The Barremian is only represented by one sample, at the top of Core 198-1213B-9R, and clearly most of the stage corresponds to an unconformity (between Cores 8R and 9R). This interval was also unconformable at Site 1214 (see **"Site 1214,"** p. 51, in "Principal Results" in the "Leg 198 Summary" chapter). The calcite compensation depth (CCD) in the Barremian is thought to have been relatively deep (e.g., Thierstein, 1979), certainly no shallower than the paleodepths of these sites at this time (2–2.5 km). Thus, the hiatus was most likely a result of a deepwater erosional event that scoured away the southern margin of Shatsky Rise.

The remainder of the mid-Cretaceous after the early Aptian was a return to better-oxygenated conditions with variation in productivity leading to deposition of radiolarian oozes (porcellanites and chert in the record) and nannofossil ooze (limestone). A hiatus occurred in the late Cenomanian to Santonian interval, the result of a widespread erosional episode that affected a wide area on the Southern High (Sliter, 1992) (see **"Site 1212,"** p. 42, in "Principal Results" in the "Leg 198 Summary" chapter). After a short depositional episode in the Santonian, a long hiatus lasted until the late Miocene. This episode was likely a result of a combination of erosion of the exposed, deep flank of the Southern High and carbonate dissolution at frequent times when the CCD shoaled above the depth of the site.

Highlights

Anoxic Events in the Early Aptian and Valanginian

Lower Aptian C_{org}-rich horizons were recovered in Core 198-1213B-8R. The horizons include olive-black to greenish black clayey porcellanites and radiolarian porcellanites with minor tuff (see **"Lithostratigraphy,"** p. 53, in "Specialty Syntheses" in the "Leg 198 Summary" chapter). Three C_{org} analyses yielded contents of 2.9, 10.2, and 25.2 wt%. The sample with the highest C_{org} content is a clayey porcellanite. Gamma ray and uranium logs show that the lower Aptian C_{org}-rich units are ~3 m thick. Total recovery of carbonaceous and noncarbonaceous in this interval (Core 198-1213B-8R) is just over 1 m. Thus, the recovery of organic-rich rocks is <30%.

Characterization of the organic matter from the most C_{org}-rich lower Aptian samples indicates it is algal and bacterial in origin and that some of this organic matter was produced by haptophytes and some by cyanobacteria. The haptophyte alkenones identified are some of the oldest known records of these compounds. The character and preservation of the bacterial material are also evidence for the existence of microbial mats at the time of deposition. Finally, the excellent preservation of organic compounds indicates deposition in highly dysoxic or anoxic conditions (see **"Geochemistry,"** p. 61, in "Specialty Syntheses" in the "Leg 198 Summary" chapter).

Section 198-1213B-8R-1 is mostly noncalcareous; however, a sample at the top, Sample 198-1213B-8R-1, 3 cm, contains the nannofossil *Eprolithus floralis* but lacks *Rhagodiscus achlyostaurion* and *Prediscosphaera columnata* and thus correlates to late Aptian Zone NC7. Sample 198-1213B-9R-1, 17 cm, lacks *Hayesites irregularis, Calcicalathina oblongata,* and *Cruciellipsis cuvillieri,* and thus correlates to upper Hauterivian–Barremian Zone NC5 (see **"Biostratigraphy,"** p. 18). Discrete intervals in Section 198-1213B-8R-1 have abundant radiolarians. Diagnostic radiolarian faunas in these samples are similar to assemblages observed in the Livello Selli in the Cismon core from the southern Alps of Italy (Premoli Silva et al., 1999). Thus, nannofossils, and particularly radiolarians, bracket the age of the carbonaceous horizons and provide a firm correlation with C_{org}-rich units of OAE1a from central Italy (the Selli level), the Italian and Swiss Alps, Sicily, France (the Goguel level), Site 641 in the eastern North Atlantic, and northern Mexico (i.e., Bréhéret, 1988; Weissert and Lini, 1991; Bralower et al., 1994; Erba, 1994; Menegatti et al., 1998; Erba et al., 1999; Bralower et al., 1999). In the Pacific, C_{org}-rich horizons of OAE1a age are also found at Sites 463 (Mid-Pacific Mountains) and 866 (Resolution Guyot) (Sliter, 1989; Jenkyns, 1995) and elsewhere on Shatsky Rise at Sites 305 and 1207 (see **"Site 1207,"** p. 16, in "Principal Results" in the "Leg 198 Summary" chapter for a more detailed discussion). C_{org}-rich lower Aptian sedimentary rocks from Sites 1207 and 1213 provide evidence for the nature of environmental changes in a truly pelagic regime during OAE1a.

Two C_{org}-rich levels in the Valanginian have considerably lower C_{org} contents than the lower Aptian horizons. A level in the lowermost Valanginian has 3.1 wt% C_{org}; one in the mid-Valanginian contains 2.5 wt%. These horizons also contain clear evidence of bioturbation indicating that deep waters were sufficiently oxygenated to support a benthic community. The horizons do not show up on gamma ray logs suggesting that they are thin. The mid-Valanginan horizon is significant as it appears to be broadly similar in age to organic-rich units that had not previously been observed outside Tethys (e.g., Lini et al., 1992). The presence of a positive carbon isotope excursion that correlates to this event suggested that it was more widespread or global in extent (e.g., Weissert and Lini, 1991). Although recovery at Site 1213 does not allow us to characterize the temporal distribution of organic-rich units, this record extends the known geographic distribution of organic-rich sediments considerably.

Chert Record

Although poorly recovered, pieces of chert in the Site 1213 section yield valuable information on variations in redox conditions through the Cretaceous. Nodules with orange, red, and brown hues indicate deposition and diagenesis in oxidizing environments, whereas those with olive-green to black hues indicate more reducing conditions during deposition and burial (see **"Lithostratigraphy,"** p. 53, in "Specialty Syntheses" in the "Leg 198 Summary" chapter). The color stratigraphy suggests that oxygenated conditions prevailed in the early Berriasian, late Aptian through middle Albian, and, when combined with data from other Leg 198 sites, from the late Cenomanian through the Maastrichtian. Reducing conditions prevailed in the Berriasian through the early

Aptian and in the late Albian to middle Cenomanian. Similar trends were observed at Sites 1207, 305, 306, and 1214 (see "Site 1214," p. 51, in "Principal Results" in the "Leg 198 Summary" chapter) for coeval portions of the sequence, suggesting that for much of the Cretaceous, the entire Shatsky Rise experienced similar redox conditions at bathyal depths. Minor variations exist, however. At Site 1207, generally reducing conditions seem to persist until the late Aptian, with oxidizing conditions characterizing the early to middle Albian and from the late Albian through the Turonian.

Important Neocomian Reference Section in the Pacific

Site 1213 contains one of a handful of Neocomian pelagic sections in the Pacific Ocean. Although the section is generally poorly recovered, nannofossils are well preserved, and radiolarians are diverse and moderately well preserved. These groups should provide precise correlations with Neocomian sections worldwide. Planktonic foraminiferal occurrence is very rare. However, shore-based investigations have the potential to map out some of the earliest evolution of this group.

Shipboard nannofossil biostratigraphy has proven challenging due to the absence of important Neocomian marker taxa, especially the nannoconids. This group, which has a poorly understood affinity, are centerpieces of the biostratigraphy of the Jurassic/Cretaceous boundary interval in particular (e.g., Bralower et al., 1989). Their absence at Site 1213 is intriguing as they are abundant in samples from Site 463 in the Mid-Pacific Mountains (Erba, 1994). At another site, Site 167 on Magellan Rise, nannoconids are absent except in the lowermost three cores (Roth, 1973). This group is also absent in assemblages that we interpret as Berriasian in Holes 49 and 50 on the deep western flank of Shatsky Rise (Fischer, Heezen, et al., 1971). What are the major controls on the distribution of nannoconids in the Pacific? Nannoconids are generally most common in continental-margin and epicontinental locations (e.g., Roth and Bowdler, 1981; Roth and Krumbach, 1986). In the Atlantic Ocean, this group is common in sites along the margins but absent in the deep sea except where transported by turbidity currents. Nannoconids are thought to be oligotrophic (e.g., Erba, 1994), and possibly to represent calcareous dinoflagellate cysts (Busson and Noël, 1991).

The record of nannoconids in the Pacific is complex. Their abundance at relatively shallow Site 463 and at Site 167 in its early (shallow) history, and absence at deeper Site 1213, suggests that water depth may be a factor controlling their distribution. Alternatively, at Site 1213 and other sites, the abundance of radiolarians throughout the section might indicate high-productivity conditions hostile to oligotrophic organisms, including the nannoconids. However, at Site 463, radiolarians are often abundant along with nannoconids (Schaaf, 1981; Erba, 1994). Most likely, a variety of environmental parameters influenced the distribution of this group.

Recovery of "Basement" of Shatsky Rise

Coring in Hole 1213B terminated in mafic igneous rocks on the flanks of southern Shatsky Rise. In all, 46.4 m of igneous section was cored, with 33.4 m recovered (72%). Six cores, 198-1213B-28R through 33R, recovered mostly massive diabase and basalt from Subunits IVA, IVB, and IVC, with each subunit thought to be a separate sill. The igneous rocks are predominantly hypocrystalline, fine-grained diabase

(97.6%) with a small amount of sparsely phyric, aphanitic basalt (2%) at contacts. The diabase groundmass consists mainly of euhedral to subhedral plagioclase and intervening subhedral pyroxene and olivine, with minor glass. Alteration in the igneous section ranges from minor to moderate. Plagioclase and pyroxene crystals are locally altered to clay, and in thin section, glassy groundmass has been ubiquitously devitrified and/or altered to clay minerals. Basaltic material in the section occurs at subunit contacts, symmetrically disposed around pieces of metasediment that mark the subunit boundaries. From the chilled contacts, the basalt grades toward more coarse-grained diabase in the unit centers, where the groundmass approaches medium grained.

The sills must be earliest Berriasian age or younger, since this is the age of the host sediment. Paleomagnetic data show that two subunits have positive magnetic inclinations, whereas the third, basal subunit has a negative inclination, implying both normal and reversed magnetic polarities are recorded in the igneous section. This mixture indicates that the sills must have formed either before or after the Cretaceous Long Normal Superchron (i.e., the Cretaceous Quiet Zone; 121–83 Ma). On the seismic profile along which Hole 1213B was drilled, the seismic "basement" has an odd character that may be related to the presence of intrusive, rather than extrusive, igneous rock at the sediment-igneous rock contact (see line 17B in oversized Figure F8, p. 14, in Klaus and Sager, this volume). The "basement" reflector, that being the deepest continuous seismic horizon, is weaker than elsewhere on Shatsky Rise, and other stronger reflectors occur beneath it. These deeper reflectors were not considered "basement" because they are not continuous along the profile, as is the weaker, shallower horizon. The cored section suggests that the weak "basement" horizon denotes the top of the sills, whereas the deeper reflectors may be the top of the extrusive lava pile.

BACKGROUND AND OBJECTIVES

Site 1213 is located on the southern flank of the Southern High of Shatsky Rise at 3883 m water depth. Basement under the site formed in the latest Jurassic within Magnetochron M20 (~145 Ma) and is close to the oldest part of Shatsky Rise (Nakanishi et al., 1989). Site 1213 is the southernmost and deepest site on the Shatsky Rise transect.

The site is located on seismic line TN037-17B (see Fig. F35, p. 125, in the "Leg 198 Summary" chapter). Correlation of this profile with the summit region of the Southern High and the seismic units of Sliter and Brown (1993) is somewhat uncertain. Precoring interpretation suggested a relatively thin seismic Unit 1 (Neogene) with prominent reflectors unconformably overlying a thin Unit 3 (Upper Cretaceous) with dipping and somewhat discontinuous reflectors and a relatively thick Unit 4 (mid-Cretaceous) and Unit 5 (Lower Cretaceous). The paleodepth of Site 1213 was ~2.8 km in the mid-Cretaceous, assuming normal subsidence rates for oceanic crust (e.g., Thierstein, 1979).

The major goals of Site 1213 drilling were to core a relatively deep-water Upper Cretaceous and Lower Cretaceous sequence as well as to obtain fresh volcanic rocks from basement underlying the sedimentary sequence for geochemical and radiometric analyses. Because this section exists at shallow burial depths, it can be reached without coring through an extensive ooze-chert sequence. Moreover, from the seismic profile, basement appears to be shallow at this site, between 400 and

600 mbsf, depending on velocity estimates for the deep sedimentary section. The site will be contained in broad leg-based objectives that include

1. Reconstructing changes in the properties of surface and deep waters including the character and stability of intermediate and deepwater circulation and vertical thermal gradients during Cretaceous intervals of extreme warmth.
2. Understanding water column stratification during mid-Cretaceous Oceanic Anoxic Events (OAEs) as well as obtaining complete records of organic-rich sediments suitable for detailed paleontological and geochemical investigations. These data will allow us to determine more fully the response of marine biotas to abrupt environmental changes and to constrain changes in carbon and nutrient cycling during the OAEs. The Shatsky Rise transect hopefully will allow us to determine whether the organic-rich sediment distribution conforms to an oxygen minimum zone model or to a deep basinal model.
3. Investigating the significance of unconformities in the stratigraphic section. Are they related to local changes in currents or to regional/basinal fluctuations in the CCD?
4. Determining fluctuations in the CCD through the Cretaceous, comparing them to other records from the North Pacific as well as from other ocean basins, and interpreting them in a paleoceanographic framework.
5. Recovering volcanic rocks from Shatsky Rise, thus providing samples to determine the age and geochemistry of basement. Compositional data from Shatsky Rise basement and other large igneous provinces will also be compared in light of the different models for their formation.

OPERATIONS

Transit from Site 1212 to Site 1213

The 56-nmi transit to Site 1213 took 6.0 hr at an average speed of 8.6 kt. Upon arriving on site, the thrusters and hydrophones were lowered and the ship was switched over to dynamic positioning mode, initiating operations at Site 1213 at 0606 hr on 2 October 2001.

Site 1213

Hole 1213A

An RCB bottom-hole assembly (BHA) was assembled and run to 3902.4 meters below rig floor (mbrf), and Hole 1213A was spudded at 1425 hr on 2 October. The first core recovered 8.43 m of sediment, indicating a seafloor depth of 3894.0 mbrf, or 3882.8 meters below sea level. RCB coring continued to 198.9 mbsf, with an average recovery for the 21 RCB cores of 21.7% (Table T1). After deploying core barrel 21R, the sinker bars on the forward core line were being run in the hole when the hole packed off without warning. Before the driller could shut down the circulating pumps, the pressure built up enough to blow the sinker bars back up into the line wiper, unseating this assembly. During this event, the core line failed just above the rope socket, and the sinker

T1. Coring summary, p. 90.

bars fell to the bottom of the drill string on top of the previously deployed core barrel. The core line was repaired, and a second set of sinker bars was attached. While the repair was being made to the wireline, Core 21R was cut. The first attempt to engage the rope socket with the overshot failed, and two more wireline runs were made using a core barrel–core catcher assembly. All attempts failed to engage the rope socket, and coring had to be terminated. The drill string was retrieved after a brief loss of circulation and rotation, ending drilling at Hole 1213A at 0300 hr on 4 October.

Hole 1213B

The ship was offset 30 m to the north, and Hole 1213B was spudded with the RCB at 1155 hr on 4 October. We drilled ahead to 189.7 mbsf to provide approximately a one-core overlap with Hole 1213A. Below 189.7 mbsf, RCB coring advanced the hole to 447.8 mbsf through largely a chert/chalk interval, with an average recovery of 10.5%. From 447.8 to 494.4 mbsf, RCB coring continued through diabase and basalt with good recovery (71.7%) at a slow rate ranging from 1.5 to 2.0 m/hr. Coring operations were terminated when the depth objectives were achieved (~50 m into igneous rock).

Following coring operations, the hole was prepared for logging, including a wiper trip to 90.6 mbsf and circulation of 40 bbl of drilling mud before and after the wiper trip. After releasing the bit, 165 bbl of logging mud was circulated, and the drill string was tripped back and positioned at 105.4 mbsf. The first logging run with the triple combo tool string was only able to reach ~431 mbsf. While logging up from that depth several tight spots were noted, including one at ~190 mbsf that required working the tool for ~30 min. The tool had to be turned off during this process, so no logs were obtained between 190 mbsf and the base of the pipe.

We did not deploy the second tool string, the FMS-sonic, because of the questionable hole conditions and the approach of severe tropical storm Krosa into the operational area. With the storm forecast to come within 150 nmi of the location, it was necessary that the drill string be recovered and the drill collars stowed before conditions worsened. After rigging down the logging equipment, the drill string was retrieved, clearing the rig floor at 1900 hr on 9 October, concluding operations at Site 1213. After securing the ship for transit, we departed on a southerly heading to avoid the approaching storm.

LITHOSTRATIGRAPHY

Description of Lithologic Units

Two holes were rotary cored at Site 1213 on the southern flank of the Southern High of Shatsky Rise at a water depth of 3883 m—the deepest water depth of any site drilled during Leg 198. The drilled section totaled 494.4 m. The objectives of this site were to core through a thin Quaternary–Neogene drape to recover a Lower Cretaceous sequence inferred to be present from seismic reflection records and to penetrate and recover basaltic “basement.” It was hoped that the recovery of C_{org}-rich horizons, which were deposited during early Aptian OAE1a, at this deeper-water site would serve for comparison with similar units obtained at Site 1207, so that the deposition of such C_{org}-rich units in a pelagic environment could be better documented. Basaltic basement has never been recovered during previous Deep Sea Drilling Project (DSDP) or Ocean Drilling Program (ODP) drilling at Shatsky Rise, with the exception of a basalt pebble recovered at the bottom of Hole 50. Basement recovery is essential for testing models of the origin and evolution of Shatsky Rise that suggest it is the product of a migrating hotspot. All of these objectives, to some extent, were achieved at Site 1213.

As at Site 1207 (and at Leg 32 Sites 305 and 306), core recovery was hampered by the presence of significant chert within the Cretaceous sequence. Chert was first encountered at ~64.7 mbsf in Hole 1213A, according to the driller's log, and was recovered in Section 198-1213A-7R-CC and in nearly every core thereafter to the bottom of the sedimentary section at 447.8 mbsf. In fact, chert and associated porcellanite are our main records of sedimentary environments in the Lower Cretaceous sequence. Recovery averaged ~20% at Site 1213 but was less than this throughout most of the Cretaceous section (Fig. **F2**). Of particular interest is the recovery of at least a partial record equivalent to the early Aptian OAE1a in Core 198-1213B-8R for which C_{org} contents of 2.87, 10.23, and 25.17 wt% were obtained (see **"Organic Geochemistry,"** p. 26). Limestone and chalk, with varying carbonate content, were also recovered intermittently in the Cretaceous sequence. The record for the Berriasian through mid-Cenomanian is sufficient to conclude that deposition occurred largely above the CCD at this site through all but the interval during OAE1a. With the exception of short episodes during the early Aptian, Valanginian, and Berriasian when thin intervals of laminated, C_{org}-rich sediments were deposited, the recovered strata were bioturbated and C_{org} poor. Much of the Barremian lies within an unconformity or condensed interval (see **"Biostratigraphy,"** p. 18).

F2. Core recovery, lithology, lithologic units, age with corresponding biostratigraphic zonations, and percent carbonate, p. 41.

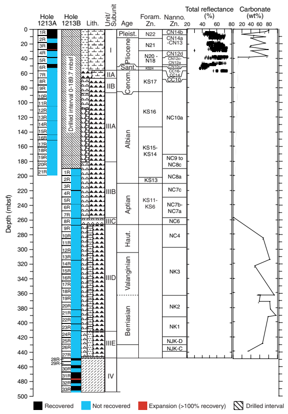

"Basement" recovery was in the form of diabase sills. Thus, we cannot ascertain the age of these units until radiometric ages are obtained. The presence of sills suggests that Shatsky Rise has had a prolonged eruptive history. Therefore, the objective of recovering normal extrusive basaltic rocks associated with the formation of Shatsky Rise volcanic edifice remains elusive.

The stratigraphic sequence at Site 1213 has been subdivided into four major lithologic units. Unit I, of Holocene to early Pliocene age, consists primarily of interbedded (cyclic) nannofossil ooze with clay and clayey nannofossil ooze. Unit II, at a depth of 56.4–85.4 mbsf, primarily consists of Santonian to Cenomanian pale orange nannofossil ooze and chert characterized by red hues. At depths of 85.4–447.8 mbsf, chert, porcellanite, and limestone primarily compose Unit III. This unit, which is early Cenomanian to Berriasian in age, is subdivided into five subunits (A–E), mainly on the basis of systematic changes in chert and porcellanite color. Unit IV comprises at least three diabase sill units totaling ~46 m.

Lithologic Unit I

Interval: 198-1213A-1R-1, 0 cm, through 6R-CC
Depth: 0.0 to 56.4 mbsf in Hole 1213A
Age: Holocene to early Pliocene

Lithologic Unit I is not subdivided into any subunits. This unit is relatively thin in comparison to the same lithology encountered at other Leg 198 sites. Unfortunately, the rotary drilling caused considerable disturbance, in places severely limiting our ability to discern primary structures and textures in the cores. The primary lithology varies from bioturbated light olive-gray (5Y 6/1) to pale yellowish brown (10YR 6/2) nannofossil ooze with clay interbedded with clayey nannofossil ooze. Carbonate contents range between 35 and 80 wt% (Fig. F2). Diatoms, foraminifers, pyrite, and ash are the most abundant accessory components with diatoms occurring only in the top 9 m. In comparison to other Leg 198 sites, no pale green "diagenetic laminae" were observed. Moderate yellowish brown (10YR 5/4) to dark yellowish brown (10YR 4/2) nannofossil clay with carbonate contents of 10–35 wt% occurs in the lowermost few meters (Fig. F3) of Unit I, just above a major unconformity between the Neogene and Upper Cretaceous.

F3. Composite digital photograph and color reflectance red/blue (680/420 nm) ratio, Core 198-1213A-6R and Section 7R-1, p. 42.

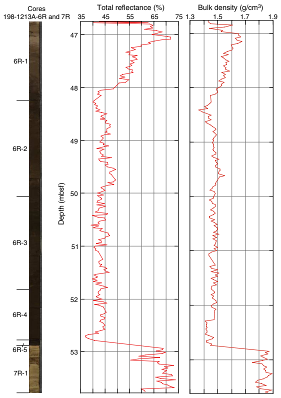

Lithologic Unit II

Interval: 198-1213A-7R-1, 0 cm, through 9R
Depth: 56.4 to 85.4 mbsf in Hole 1213A
Age: Santonian to early Cenomanian

In Unit II, nannofossil ooze was recovered only in Section 198-1213A-7R-1. The grayish orange (10YR 7/4) ooze in this core exhibits striking and unusual color banding of dark yellowish orange (10YR 6/6) to light brown (5YR 5/6) interposed with grayish orange ooze on a 1- to 3-cm scale (Fig. F3). The darker bands are more clay rich and somewhat indurated relative to the nannofossil ooze and are commonly underlain and/or overlain by a thin interval of very pale orange (10YR 8/2) nannofossil ooze.

Subunit IIA

Unit II is separated into two subunits, primarily on the basis of the relative abundance of chert. Subunit IIA (Core 198-1213A-7R), from 56.4 to 66.1 mbsf, consists of Santonian (possibly upper Coniacian) very pale orange (10YR 8/2) nannofossil ooze and moderate brown (5YR 3/4) to dusky brown (5YR 2/2) chert that was recovered at 64.7 mbsf, according to the driller's log.

Subunit IIB

Subunit IIA is underlain by Subunit IIB (Cores 198-1213A-8R and 9R), which extends from 66.1 to 85.4 mbsf. This subunit is early to middle Cenomanian in age and consists primarily of moderate yellowish brown (10YR 5/4), dark yellowish brown (10YR 4/2), and light brown (5YR 5/6) chert, and associated very pale orange (10YR 8/2) porcellanite.

Lithologic Unit III

Intervals: 198-1213A-10R through 21R (end of hole) and 198-1213B-1R through 27R
Depth: 85.4 mbsf in Hole 1213A to 447.8 mbsf in Hole 1213B
Age: early Cenomanian through Berriasian

Subunit IIIA

Unit III is subdivided into five subunits, mainly on the basis of chert color and changes in associated lithologies. Subunit IIIA (Cores 198-1213A-10R to 19R) extends from 85.4 to 179.6 mbsf and is early Cenomanian to late Albian in age. It consists of medium dark gray (N5) to dark gray (N4) chert associated or interbedded with light gray (N7), light greenish gray (5GY 8/1), and very pale orange (10YR 8/2) porcellanite and light greenish gray (5GY 8/1) limestone (primarily in Cores 198-1213A-12R to 19R).

Subunit IIIB

Subunit IIIB (Cores 198-1213A-20R through 21R and Cores 198-1213B-1R through 7R) encompasses the interval from 179.6 to 256.8 mbsf and is early late Albian–early late Aptian in age. Primary lithologies are light to moderate brown (5YR 5/6 to 5YR 3/4), grayish brown (5YR 3/2), moderate reddish brown (10R 4/6), and dusky red (10R 4/6) chert associated with very pale orange (10YR 6/2) to grayish orange (10YR 7/4) and pale yellowish brown (10YR 6/2) porcellanite.

Subunit IIIC

Subunit IIIC (Core 198-1213B-8R), of early Aptian age, occurs between 256.8 and 266.4 mbsf. This subunit is characterized by interbedded C_{org}-rich clayey porcellanite and radiolarian porcellanite, mostly olive black (5Y 2/1) to greenish black (5G 2/1) and dusky green (5G 3/2), with minor altered tuff. Although C_{org} contents of selected samples are high (Fig. F4), there is no clear evidence of fine lamination that would indicate deposition under an anaerobic water column (Figs. F5, F6). Bioturbation is moderate to intense in this interval.

Subunit IIID

Subunit IIID (Cores 198-1213B-9R through 23R) lies between 266.4 and 410.3 mbsf, extending from the Hauterivian to the Berriasian. Medium gray (N5) through dark gray (N3) chert, white (N9) to yellowish gray (5Y 8/1) porcellanite, and mostly light greenish gray (5GY 8/1) with some olive-gray (5Y 4/1) nannofossil chalk to clayey nannofossil chalk are the primary lithologies recovered. Incomplete recovery prohibits conclusions regarding the pervasiveness of carbonate cycles, but some longer chalk intervals indicate substantial variations in carbonate content over tens of centimeters (Fig. F7). Bioturbation is moderate to intense throughout this subunit (Fig. F8). One interval exhibits features suggesting soft-sediment deformation, possibly a small slump (Fig. F9).

Subunit IIIE

Subunit IIIE (Cores 198-1213B-24R through 27R), of Berriasian age, is the lowermost of the sedimentary units recovered at Site 1213. This subunit encompasses the interval at 410.3–447.8 mbsf and consists of brownish gray (5YR 6/1), grayish red (10R 4/2), and pale to moderate brown (5YR 5/2 and 5YR 6/4) chert, yellowish gray (5Y 8/1) and very pale orange (10YR 8/2) porcellanite, and moderate brown (5YR 6/4) to pale brown (5YR 5/2) claystone with nannofossils. A silicified goethitic claystone breccia (Fig. F10) at the base of Core 198-1213B-27R exhibits colliform features. A thin section of this sample exhibits possible microbial structures (Fig. F11).

Lithologic Unit IV

Interval: 198-1213B-28R through 33R
Age: Unknown
Depth: 447.8–494.4 mbsf in Hole 1213B

Lithologic Unit IV consists of mafic igneous rocks, dark greenish gray (5G 4/1) diabase or dolerite (97.6%) and dark gray (N3) basalt (2.0%), with intervening metasedimentary rocks (0.4%) (Tables T2, T3). This

F4. Digital photograph showing the early OAE1a equivalent and associated sediment, p. 43.

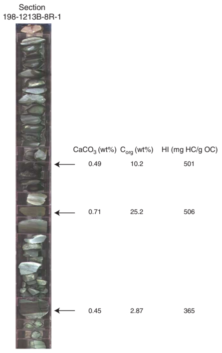

F5. Pieces of early Aptian relatively C_{org}-rich radiolarian claystone of Subunit IIIC, p. 44.

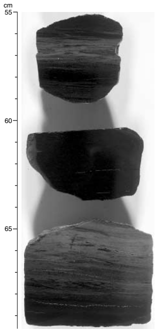

F6. Homogeneous, black radiolarian claystone of early Aptian age, p. 45.

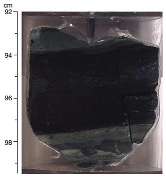

F7. Bioturbated Berriasian chalk-nannofossil claystone cycle in Subunit IIID, p. 46.

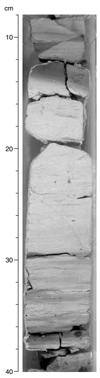

unit is further subdivided on the basis of lithologic patterns into at least three subunits (A–C) thought to represent at least three intrusive events separated by "baked" sediment (Fig. **F12**). The uppermost chilled margin of Unit IV is pictured in Figure **F13,** and baked contacts are shown in Figures **F14** and **F15.**

Rock names are based on hand specimen and thin section description. No bulk chemical data were collected to define the chemistry of the igneous rocks, but one bulk X-ray diffraction (XRD) of the diabase confirms the presence of clinopyroxene (diopside and/or titanium-aluminum clinopyroxene), plagioclase feldspar (calcian albite and/or sodian anorthite), and clay minerals (montmorillonite/smectite alteration products of minerals and glassy groundmass) observed in thin section. The term diabase is applied to the lighter, more phaneritic parts of the core, and basalt is applied to the darker, more aphanitic, and less crystallized rocks. Diabase crystallinity (crystal size) is not uniform through a given subunit, with the most coarsely crystalline diabase present in the middle of the subunits. The diabase is generally fine grained but locally ranges to medium grained. Where contacts between basalt and diabase are preserved, they appear to be gradational (Fig. **F15**). Thin section observations confirm the subtle gradation between diabase and basalt in the core (Figs. **F16, F17, F18**).

The diabase appears relatively fresh in hand specimen with primarily fine-grained phaneritic texture. There are few phenocrysts, with the rock mainly composed of felted groundmass of euhedral to subhedral plagioclase microlites and intervening subhedral to anhedral pyroxene, olivine, and glass. Thin sections prepared from these units show the rock to be largely hypocrystalline (mostly crystals) to nearly holocrystalline (5% glassy groundmass). These rocks exhibit subophytic (Fig. **F18**) to intergranular textures (Fig. **F16**). Plagioclase crystals are ≤1.8 mm long, averaging from 0.7 to 0.8 mm. Olivine and clinopyroxene crystals are generally smaller, averaging up to 0.7 mm in the subophytic diabase and up to 0.5 mm in the intergranular diabase. Additional minerals include opaque crystals of ilmenite/magnetite(?) that are locally skeletal. Both pyroxene and olivine are relatively colorless and therefore differentiated primarily on the absence/presence of cleavage. In all instances, the glassy groundmass is devitrified and/or altered to green/brown clay minerals. Plagioclase crystals often exhibit fine hairline fractures filled by birefringent clay minerals. Patches of clay and carbonate with relict cleavage in some samples suggest replacement of a mineral phase, possibly pyroxene (Fig. **F15**).

In hand specimen, the basalt ranges from aphyric to sparsely phyric to moderately phyric with glassy to microcrystalline groundmass and dominantly millimeter-sized phenocrysts (Figs. **F13, F14, F15**). Only one thin section of basalt was made to preserve this material for post-cruise studies. One gradational basalt sample (198-1213B-30R-4, 39–41 cm) shows mainly intersertal (hyalophitic) texture but ranges to intergranular in some crystal-rich areas. A basalt sample with seriate texture exhibits quench textures: swallow-tail plagioclase crystals and fibrous bundles of crystallites (Sample 198-1213B-31R-1, 7–10 cm; Fig. **F16**). Alternatively, the latter could be devitrification products of the once glassy, now altered groundmass. This sample is cut by a smectite-filled vein and contains amygdules filled by fibrous smectite. The plagioclase crystals are moderately to extremely altered (Fig. **F16**) to green clay minerals (smectite?).

Sparse (<1% by volume) irregular to rounded glomeroporphyritic clusters are present throughout Unit IV (at 56 and 59 cm in Fig. **F15;**

F8. Highly bioturbated fabric of Berriasian radiolarian chalks and clayey chalks of Subunit IIID, p. 47.

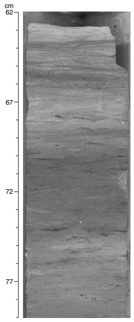

F9. Soft-sediment deformation, probably a small slump unit, in clayey chalks of Subunit IIID, p. 48.

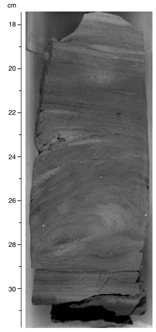

F10. X-ray diffractogram for hydrothermal alteration breccia, p. 49.

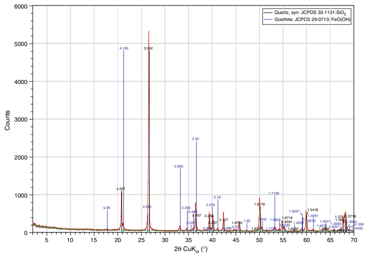

F11. Photomicrographs showing possible microbial structures enclosed in quartz crystal cement, p. 50.

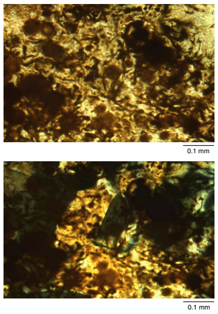

also see Figs. **F18, F19, F20**). These clusters range up to 1 cm in size and are mainly composed of fine-grained plagioclase and pyroxene. In thin section, the glomeroporphyritic clusters are composed of plagioclase feldspar crystals ≤2 mm long that are separated by patches of pyroxene and opaque minerals. In one instance, extinction under cross-polarized light migrated from crystal to crystal, suggesting that the crystals may be xenoliths rather than magmatic crystal aggregates.

In hand specimen, vesicles are essentially limited to the intervals of basalt, and these are often completely filled (amygdules) by calcite and/or green clay minerals (Fig. **F16**). The vesicles are round to irregular in shape and range up to 1.5 mm in diameter. Vesicle content, up to a few percent of the rock volume, was noted to increase toward inferred upper and lower contacts with metasedimentary rocks.

The vein systems are oriented subvertically (e.g., Subunit IVA) to subhorizontally (Fig. **F21**). They are filled by dark green clay minerals, white calcite, or mixtures of the two, locally with pyrite and rarely with quartz. The veins are sometimes monomineralic, but the larger ones are often zoned (Fig. **F22**), exhibiting crack-seal textures. The largest vein, in Section 198-1213B-33R-4, is vuggy and only partly filled by calcite. Slickensides and vein offsets suggest that there has been some microfault displacement along these features.

Two fragments of nonvolcanic rock are present within Unit IV (disregarding possible downhole contamination at the tops of some cores). These loose fragments are "sandwiched" between intervals of basalt, but with no preserved contacts (Figs. **F12, F13, F14**). Thin sections of these fragments show them to be silicified burrowed shale/phyllite with volcanic ash (Sample 198-1213B-30R-4, 66–69 cm) and metachert (Sample 198-1213B-32R-4, 65–74 cm). Petrographic evidence for thermal alteration of these sedimentary rocks includes a well-developed uniform extinction in the shale/phyllite (with nicols crossed) and microcrystalline (0.1 mm) subequal crystals of quartz (recrystallized) encompassing fibrous bundles of sillimanite or possibly tremolite/actinolite within the metachert (Fig. **F23**).

Open fractures in the core are likely drilling induced and are often localized along thin veins. Some dark seams, expansion fractures(?), were noted. These are more closely spaced in the basalt contact zones (a few millimeters apart) and become more widely spaced (a few centimeters apart) into the adjacent diabase, where they eventually disappear. This relationship suggests that their development may be associated with the rate of cooling. In thin section, these dark seams are filled with greenish brown clay minerals.

Interpretation

Hiatuses

Sedimentation on this part of Shatsky Rise appears to have been continuous during the Early through mid-Cretaceous (see **"Biostratigraphy,"** p. 18). However, there are at least two intra-Cretaceous unconformities represented by the absence of upper Cenomanian through at least lower Coniacian strata between Cores 198-1213A-8R and 7R and most or all of the Barremian between Cores 1198-1213B-8R and 9R. A barren interval in the base of Core 198-1213A-6R overlies definite Santonian nannofossil ooze in Core 7R, and this, in turn, is overlain by lower Pliocene ooze in the upper part of Core 6R. The oxidized, clay-rich bands in the Santonian ooze may reflect slow deposition above the

T2. Mineralogy and texture of diabase and basalt estimated from thin section, p. 92.

T3. Mineralogy and lithology of metamorphosed sediment, p. 94.

F12. Diabase units and numbered core pieces, p. 51.

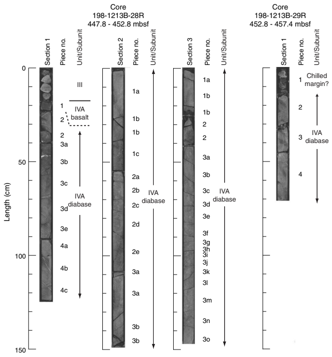

F13. Chilled margin above diabase and overlain by "baked" chert, p. 59.

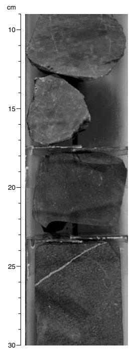

F14. Basalt recovered near metamorphosed sedimentary rock with burrow structures, p. 60.

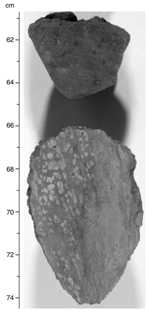

unconformity with the Cenomanian. In seismic reflection lines (see "Background and Objectives," p. 6) over Site 1213, Cretaceous reflectors can be observed terminating against a more flat-lying pelagic drape that presumably reflects the Neogene–Quaternary sequence. However, it is not easily discerned whether the condensed Santonian–Coniacian interval is part of the pelagic drape. If that is the case, it would appear that the slight angular unconformity between the Santonian–Coniacian and older Cretaceous strata represents an erosional unconformity, perhaps resulting from enhanced deep currents sweeping the flanks of Shatsky Rise, rather than a dissolution horizon. This hypothesis is supported by the fact that the mid-Cretaceous sequence was present, but poorly recovered, at Site 1207 on the Northern High. However, enhanced rates of carbonate dissolution at deeper depths could have undermined the slope sediment buttress and caused slumping of sediments at shallower depths on the Southern High. Enhanced carbonate dissolution during a CCD rise in the early Aptian (see below) may also be invoked to explain the missing Barremian at Sites 1213 and 1214.

A second unconformity or condensed interval occurs between the Santonian and Neogene. This stratigraphic gap is widespread, having been encountered at Sites 1207 and 1208 on the Northern and Central Highs where most of the Paleogene and uppermost Cretaceous are missing on the basis of age calibration of seismic reflection records. It is likely that this unconformity also represents the erosive effects of deep currents sweeping the upper Shatsky Rise that waned somewhat in the Miocene. Most of the Upper Cretaceous and Paleogene were recovered, however, at all sites on the Southern High except at Site 1213. Again, carbonate dissolution could have played a role.

Carbonate Preservation and Diagenesis

Unit III encompasses the Berriasian through mid-Cenomanian. Relatively high carbonate contents persist in the nonchert lithologies recovered through this interval, suggesting that deposition occurred above the CCD except during the early Aptian (see below). We do not have a definitive indication of paleowater depth, but it is very likely that the seafloor depth was shallower than at present, particularly during the Early Cretaceous (Fig. F25). The earliest sedimentary rock above the diabase of Unit IV is red nannofossil claystone with carbonate content of 34 wt%, the lowest carbonate content of the Cretaceous with the exception of the lower Aptian C_{org}-rich interval. Carbonate contents generally increase upward from the basal Berriasian but vary considerably. Recovery of chalk was better in part of Subunit IIID, particularly in Cores 198-1213B-20R through 24R, and the recovered intervals reveal carbonate cycles on scales of 10–20 cm, although there is insufficient continuous material to establish a specific periodicity or pattern. These cycles may represent either variation in carbonate dissolution or productivity inasmuch as we would not expect strong variation in dilution by terrigenous material in this pelagic setting. Radiolarians appear to be concentrated in more C_{org}-rich intervals of some of the cycles (e.g., in Section 198-1213B-22R-1), which could indicate higher siliceous productivity; however, it is not clear that radiolarian relative abundance can be related directly to primary production (see below). Radiolarians are also associated with chert and porcellanite, which, in part, replace carbonate.

It is also interesting that, with the exception of replacement of chalks by porcellanite throughout the sequence and some limestone pieces re-

F15. Symmetrical basalt contact zones around a fragment of metachert, p. 61.

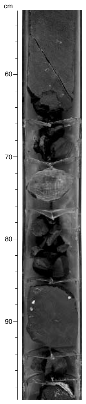

F16. Basalt exhibiting sparsely phyric texture, p. 62.

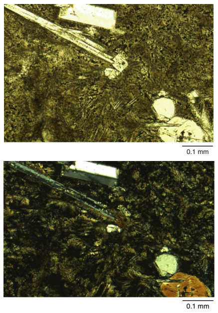

F17. Diabase showing intersertal to subophitic texture, p. 63.

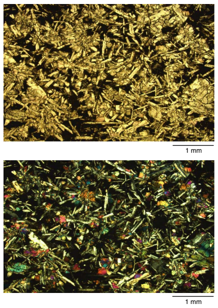

F18. Diabase showing subophytic texture with light plagioclase crystals, p. 64.

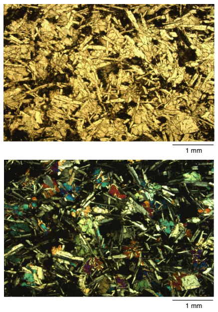

covered in Subunit IIIA, the diagenetic grade of carbonates did not go beyond "chalk" downhole. The lack of limestone in the pre-Cenomanian sequence must be a function of a continually shallow burial depth throughout the depositional history of this part of Shatsky Rise, possibly as a result of several erosional episodes. The presence of limestone in the lower Cenomanian Subunit IIIA remains unexplained.

Biogenic Silica Deposition and Diagenesis

Radiolarites, most occurring as porcellanite, are common throughout the Cretaceous of Site 1213. Chert is nearly ubiquitous as well, and much of the silica must have been derived from radiolarian dissolution. In the Berriasian through Hauterivian, radiolarians in chalks commonly have been replaced by calcite, and some were filled later with chalcedony. There is evidence for relatively early silica cementation because chert commonly preserves burrows without compactional flattening, whereas burrows in chalks, particularly clayey chalks, are characterized by compactional flattening. However, breakage of radiolarians in radiolarian-rich intervals can be observed in some samples. A breccia of slightly disturbed chert rip-up clasts, cemented by chalcedony, is present in Core 198-1213B-3R and suggests formation of an early "firmground," providing further support for early silica diagenesis. We interpret chert color generally to reflect the oxidation state of associated sediments. For example, red and brown chert hues accompany very pale orange to pale orange chalks and oozes and black to gray chert hues typically are associated with white to grayish green chalks and porcellanites. In some cases, however, we observed contrasting colors. For example, in Sample 198-1213B-24R-1, 115–121 cm, a very irregularly bounded reddish colored chert nodule is set in a grayish green chalk. It is difficult to understand how chert could form from postdepositional fluids that carried oxygen and only affected areas of otherwise reduced sediments where chert precipitation occurred. More likely, the quartz precipitated early, prior to postdepositional reduction of the sediment, thereby preserving a reddish, oxidized hue.

Some radiolarian-rich porcellanites exhibit signs of reworking by bottom traction currents, including ripple cross-lamination and parallel laminae to flaser structure. Such features are most common in Cores 198-1213B-4R through 6R in conjunction with oxic conditions. In general, the locally high concentrations of radiolarian tests likely indicate winnowing and concentration by currents.

The abundance of radiolarian-rich strata and chert recovered from the Cretaceous section at Site 1213 might suggest high productivity of siliceous biogenic material and could be related to the near paleoequatorial location of Shatsky Rise through most of the Cretaceous. On the other hand, in the Cretaceous, radiolarian abundance could be a function of enhanced preservation in silica-rich deepwater masses as indicated by radiolarian-rich strata widespread in the Pacific and Tethyan basins.

Cretaceous Redox Variations

Orange, red, and brown hues in cherts, porcellanites, and, to some extent, chalks, are characteristic of Subunits IIIE and IIIB. Cherts in Subunits IIID and IIIA have gray hues, and the porcellanites and chalks recovered from these intervals are primarily of grayish green to olive-green hue. Subunit IIIC represents the lower Aptian C_{org}-rich interval

F19. Striped areas thought to be pyroxene (olivine?) crystals replaced by clay minerals, p. 65.

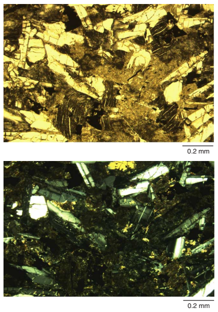

F20. Large glomeroporphyritic cluster of plagioclase crystals, p. 66.

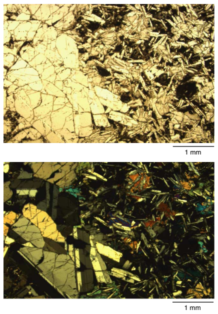

F21. Diabase cut by a zoned calcite- and smectite-filled vein, offset by several thin filled veins, p. 67.

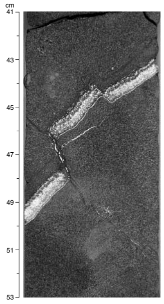

F22. Complex veins showing an early phase of botryoidal to bladed carbonate, p. 68

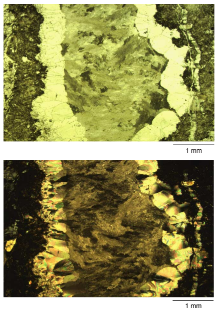

for which no chert was recovered, but the porcellanites and clayey porcellanites are dark colored and C_{org} rich. Thus, we can outline a trend from the oxidizing conditions that prevailed in the basal Berriasian to reducing conditions in the remainder of the Berriasian through early Aptian. This was followed by oxidizing conditions in the late Aptian through middle Albian, a return to reducing conditions in the late Albian to early Cenomanian, and oxidizing conditions in the early Cenomanian and later Cretaceous, at least as far as the recovered section permits inferences to be made.

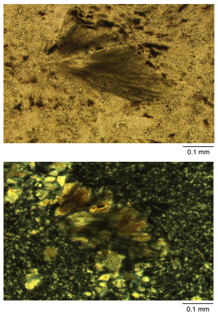

F23. Radiating fibrous crystals encased in microcrystalline quartz, p. 69.

Most of the more reduced intervals are not necessarily related to lower oxygen concentrations in deep water because higher sedimentation rates can drive redox reactions by promoting initial preservation of small amounts of organic matter and limiting penetration of oxygen across the sediment/water interface. In particular, the Berriasian interval was deposited at a rapid rate (see **"Sedimentation and Accumulation Rates,"** p. 25), as was the upper Albian through lower Cenomanian, and both intervals are characterized by chert hues reflecting reducing conditions. Most of the sequence is not particularly pyritic (megascopic observation), and C_{org} contents are low with the exception of one thin, irregularly laminated clayey chalk with 3.13 wt% C_{org} in Sample 198-1213B-19R-1, 112–113 cm. This is true of most of the recovered section above, except for a 1-cm interval of Valanginian clayey, radiolarian chalk (Sample 198-1213B-15R-1, 9–10 cm, with 2.54 wt% C_{org}) and the lower Aptian C_{org}-rich interval.

The Valanginian relatively C_{org}-rich layer has been heavily bioturbated and exhibits no characteristics indicative of seafloor anoxia. However, if short-term anoxia did occur, any fine lamination could have been destroyed by subsequent bioturbation. Biostratigraphic determinations place the age of the recovered interval within the interval of the Valanginian positive carbon isotope excursion (Lini et al., 1992) for which there are, to date, no known exceptionally widespread C_{org}-rich deposits. It is possible that we recovered only one of a number of such beds in the Valanginian at Site 1213. Apparently, the C_{org}-rich intervals are too thin to capture in downhole log signatures (see **"Downhole Measurements,"** p. 32), so we cannot document the possible significance of Valanginian events here.

The lower Aptian Selli equivalent was partially sampled at Site 1207 (Core 198-1207-44R) and consists of a faintly laminated radiolarian claystone containing as much as 34 wt% C_{org}. In Core 198-1213B-8R, we recovered a sequence of radiolarites, porcellanites, and radiolarian claystones that contain high amounts of C_{org} and correspond to OAE1a (e.g., Bralower et al., 1994) or the Selli event. Several C_{org} determinations were made, and a maximum of 25.2 wt% was obtained. Recovery of this interval is fragmentary, and there are few continuous core pieces to examine. There are a number of individual C_{org}-rich units, most of which have been heavily bioturbated and homogenized such that evidence of any original fine lamination has been destroyed. The claystones and porcellanites commonly appear somewhat coarsely laminated because of abundant flattened, dark, horizontal burrows. Nonetheless, one must infer from the high contents of C_{org} and high pyrolysis hydrogen indices (>500) (see **"Organic Geochemistry,"** p. 26) that conditions were at least intermittently anaerobic at the seafloor. The downhole logs suggest that the interval in question was as much as 7 m thick overall, but the main interval of C_{org}-rich sediment occurs between 257 and 260 mbsf. This is exhibited as a double peak of higher gamma ray and resistivity values and as higher uranium and potassium values in the spectral gamma log for this interval (see **"Downhole Measurements,"** p. 32).

The difference in present water depths of Sites 1207 (3101 m) and 1213 (3882 m) is nearly 800 m, and a larger depth difference may have characterized the early Aptian because of the younger crustal age of northern Shatsky Rise (Chron M12 at ~133 Ma vs. Chron M21 at ~147 Ma for southern Shatsky Rise). Thus, one could envision that an extensive zone of water-column anoxia prevailed in the region during the early Aptian. On the basis of plate tectonic reconstructions, the southern Shatsky Rise would have been located under the paleoequator at ~120 Ma. As a result, high rates of C_{org} production in surface water masses may have prevailed over the site. Sediment of Cores 198-1213B-8R and 198-1207B-44R is very low in carbonate, suggesting that the CCD rose above the depth of both sites during the event. This scenario is similar to that in the North Atlantic Basin (e.g., Arthur and Dean, 1986; Bralower et al., 1994). At the same time, radiolarians are quite abundant through this interval, suggesting high rates of siliceous production. The combination of relative lack of dilution by carbonate or clay, high C_{org} fluxes, and enhanced preservation under low-oxygen conditions probably produced the extraordinary C_{org} concentrations in this interval.

The change to oxidizing conditions in the early Aptian through middle Albian at Site 1213, following early OAE1a, can also be identified using chert coloration (Table **T4**) at Site 1207. Likewise, a return to reducing conditions in sediments of Cenomanian age, and post-Cenomanian oxic conditions are seen at both sites. These trends may be related to global trends in deepwater oxygen concentration but are not clearly related to paleolatitude changes inasmuch as Shatsky Rise remained in a potential region of high productivity through the Cenomanian at least (see **"Background and Objectives,"** p. 6).

T4. Downhole variation in colors of recovered chert, p. 95.

Hydrothermal Alteration

Several interesting features appear in Cores 198-1213B-26R and 27R that we interpret as resulting from deformation and fluid circulation induced by diabase sills that intruded into the sedimentary sequence. The most obvious of these features is the breccia at the base of Section 198-1213B-27R-1. This breccia consists of 1- to 3-cm fragments of relatively soft goethitic clay held together by a stockwork of fine veins of chalcedony as confirmed by XRD data (Fig. **F10**). We suggest that this unit resulted from a clay-rich sediment that was brecciated during intrusion of one or more diabase sills then altered by warm, silica- and iron-rich fluids arising from the cooling diabase. It is possible that these fluids percolated further upward through fractures and created zones of reduction along fractures in dominantly red nannofossil claystones observed in Core 198-1213B-27R, as well as diffuse pale blue and yellowish orange alterations along fractures in chert of Core 26R. These fluids may have also nourished microbial communities within the pores of the brecciated sediment.

Diabase Sill Units

The igneous rocks recovered at Site 1213 are massive, without fragmental or pillow structures. The basalt intervals are thought to represent chilled margins of a series of intrusive dikes/sills (Subunits IVA–

IVC). Gradational changes in crystallinity within the subunits, from outer chilled margins (basalt) to more coarsely crystalline and more holocrystalline interiors (diabase), are consistent with mafic magma intrusion. A fibrous mineral in the metachert fragment is likely metamorphic, given its inclusion within multiple quartz crystals within coarser (0.1 mm) mosaics associated with relict burrow mottles; burrows in Unit III cherts are often filled with more porous porcellanite and therefore would have likely been the focus of hot fluid migration during contact metamorphism. The symmetry of the basalt/diabase transition around metasedimentary rock fragments in the cores suggests that these represent country rock that hosted the intrusions. Expansion fracture patterns in the basalt, localization of vesicles near contacts, and observed quench textures in the basalts also support an intrusion interpretation.

The shallowest intrusion (Subunit IVA) is ~20 m thick, the medial intrusion (Subunit IVB) is ~14 m thick, and the basal intrusion (Subunit IVC) is, at a minimum, 7 m thick on the basis of a comparison of cored intervals vs. recovered material. There is little apparent textural or compositional difference among the three subunits, but the paleomagnetic signature of the last core (Core 198-1213B-33R) indicates that it may be much older (see **"Paleomagnetism,"** p. 24). A thin section of the diabase from this last core (Fig. **F24**) shows this rock to contain large, zoned, and altered plagioclase phenocrysts unlike any observed in thin sections from Cores 198-1213B-28R to 32R. This sample also appears to be altered in general. No intrusive contact relationships were recovered in Core 198-1213B-32R, where recovery was only 70%. The presence of rubble zones and large mineralized fractures within the base of Cores 198-1213B-32R and 33R are also consistent with a fault contact interpretation.

F24. Large plagioclase phenocryst that is complexly zoned, p. 70.

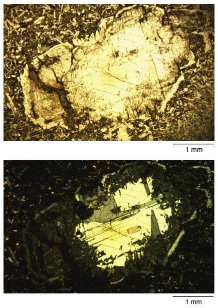

BIOSTRATIGRAPHY

Two holes were rotary drilled at Site 1213 on the Southern High of Shatsky Rise. Sediments from the upper Pleistocene to basal Berriasian were recovered overlying a series of diabase sills (see **"Lithostratigraphy,"** p. 8). In Hole 1213A, sediments were recovered from the upper Pleistocene to middle Albian. Hole 1213B was cored from the middle Albian. Based on nannofossil and planktonic foraminiferal datums, it was determined that two major unconformities are present in this part of the Shatsky Rise, separating the lower Pliocene–lower Santonian and lower Santonian–lower Cenomanian (see **"Sedimentation and Accumulation Rates,"** p. 25). The basal Aptian to Hauterivian interval likely contains an unconformity or highly condensed sequence.

Calcareous nannofossils are generally abundant and moderately to well preserved throughout the sediments of Holes 1213A and 1213B. Neogene planktonic foraminifers are moderately preserved, and abundances are generally low because of selective dissolution and fragmentation, whereas in the Cretaceous sequence, which mainly consists of chert and porcellanite with rare interbedded limestone, planktonic foraminifers are rare and generally poorly preserved.

All core catcher samples were examined, and supplementary samples were used to refine datums and the stratigraphy in and around critical intervals and unconformities. The main calcareous nannofossil and foraminiferal datums are summarized in Tables **T5** and **T6.**

T5. Calcareous nannofossil datums, ages, and depths, p. 96.

T6. Planktonic foraminifer datums, ages, and depths, p. 97.

Radiolarians, which are very abundant from the upper Albian to the basal Berriasian or uppermost Tithonian sequence in Hole 1213B, were examined in selected samples to refine the age estimate provided by nannofossils and planktonic foraminifers.

Studies of benthic foraminifers were conducted on core catcher samples from Holes 1213A and 1213B. They are well preserved and common in the Neogene section and moderately preserved and rare to few in abundance in the Cretaceous. Stratigraphic ranges of benthic foraminifers are summarized in Tables T7 and T8. Neogene paleodepth estimates (Fig. F25) are based on the work of Pflum and Frerichs (1976), Woodruff (1985), and van Morkhoven et al. (1986). For the Cretaceous section, estimates are mainly based on Sliter (1977, 1980), Kaiho (1998), and Holbourn et al. (2001), as well as backtracked paleodepth curves from the DSDP and ODP data of Kaiho (1999).

T7. Cenozoic and Cretaceous benthic foraminifers, Hole 1213A, p. 98.

T8. Cretaceous benthic foraminifers, Hole 1213B, p. 99.

F25. Estimated paleodepth, p. 71.

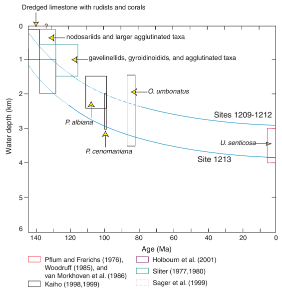

Calcareous Nannofossils

Neogene

The Neogene section ranges from the upper Pleistocene (Subzone CN14b) to lower Pliocene (Subzone CN10c). This interval appears to be relatively complete and has high sedimentation rates typical of upper Neogene sections on Shatsky Rise. The oldest nannofossil-bearing Neogene sample (Sample 198-1213A-6R-3, 94 cm) is assigned to Subzone CN10c based on the co-occurrence of *Amaurolithus delicatus, Ceratolithus rugosus,* and *Discoaster tamalis.* An interval of barren brown clay (interval 198-1213A-6R-4, 94 cm, through Section 6R-CC) overlies the Cretaceous section.

Cretaceous

The Cretaceous section ranges from the Santonian (Zone CC15–CC17) to lower Berriasian or uppermost Tithonian (Subzone NJK–C). The Santonian sediments (e.g., Samples 198-1213A-7R-1, 3 cm; 7R-1, 90 cm; and 7R-CC) contain moderately etched nannofossil assemblages, including *Lithastrinus grillii.* The absence of robust, younger coccoliths, such as *Arkhangelskiella cymbiformis* and *Aspidolithus parcus,* allows us to assign this interval to Zones CC15–CC17 (UC11 and UC12). This interval overlies a relatively biostratigraphically complete Cenomanian (Zone UC3) to basal Berriasian or uppermost Tithonian (Subzone NJK–C) section characterized by chert, porcellanite, and chalk that were generally poorly recovered. In many cores, enough chalk was recovered to provide adequate sample material; however, in some cases, sediment had to be scraped from chert pieces. All cores yield nannofossils.

The youngest part of the chert-bearing sequence is Cenomanian (UC3) (Sample 198-1213A-8R-CC) based on the presence of *Lithraphidites acutus.* A complete lower Cenomanian to lower Aptian succession was recovered through interval 198-1213A-8R-CC to 198-1213B-8R-CC. The lower Cenomanian to upper Albian (Zone NC10) is particularly thick.

An organic-rich interval was recovered in Core 198-1213B-8R, and nannofossil biostratigraphy suggests an early Aptian age within Zone NC6, supporting the correlation of this interval with the OAE1a Selli event. The organic-rich sedimentary rocks are barren of nannofossils, but a carbonate layer from a chert piece high in the core (Sample 198-1213B-8R-1, 3 cm) yields the lowest downhole occurrence (i.e., first occurrence [FO]) of *E. floralis,* marking the base of Zone NC7 (lower Aptian). The next fossiliferous sample below the barren interval (Sample 198-1213B-9R-1, 17 cm) is tentatively assigned to the lower Barremian, based upon the abundance of *Zeugrhabdotus scutula,* an acme that is used to define a zone (correlative with Subzones NC5d and NC5e) in the Boreal region (Bown et al., 1998). However, the reliability of this acme zone is untested away from the Boreal area, and the age of the sample could conceivably range from late Hauterivian to Barremian. In any case, there is almost certainly at least one unconformity representing much of the Barremian and perhaps the uppermost Hauterivian. The lack of continuous core in this interval prevents further biostratigraphic refinement.

The first downhole occurrence of *C. cuvillieri* is observed in Sample 198-1213B-9R-1, 47 cm, and marks the base of Zone NC5 (upper Hauterivian). This species was the only "standard" Neocomian marker taxon recorded in Hole 1213B. The absence of *C. oblongata, Lithraphidites bollii, Tubodiscus verenae,* and nannoconids greatly hinders the biostratigraphic subdivision of the Neocomian at Site 1213. These absences must be due to paleoecological factors because the nannofossil preservation is moderate to good and species richness remains relatively high throughout. In fact, this section represents one of the best deep-sea nannofossil records for the Neocomian time interval. Nannofossil biostratigraphy thus relied on secondary marker species, and the results should be viewed with caution. Even biostratigraphically useful species that are present tend to be rare and sporadically distributed (e.g., *Eiffellithus windii, Umbria granulosa,* and *Rucinolithus wisei*). The last occurrence (LO) of *R. wisei* (Sample 198-1213B-14R-1, 12 cm) and presence of *E. windii* (Samples 198-1213B-14R-1, 58 cm, and 14R-1, 148 cm) indicate a Valanginian age (Subzone NK3A). The FO of *Tubodiscus* spp. (Sample 198-1213B-19R-1, 119 cm) and the occurrence of *U. granulosa* (Sample 198-1213B-21R-1, 150 cm) indicate a Berriasian age. The FO of *Assipetra infracretacea* (Sample 198-1213B-26R-1, 15 cm) is a lower Berriasian datum. The presence of *C. cuvillieri* and *Rotelapillus laffittei* in the lowermost nannofossil-bearing sample (Sample 198-1213B-27R-1, 38 cm) indicates a correlation with Subzone NJK–C, which ranges across the Jurassic/Cretaceous boundary.

Planktonic Foraminifers

Neogene

An apparently complete upper Pliocene to Pleistocene nannofossil ooze was recovered in Hole 1213A. Preservation of planktonic foraminifers is generally poor and characterized by selective dissolution and fragmentation. The assemblages in this interval (Zones N22 and N21) (Sections 198-1213A-1H-CC through 5H-CC) are dominated by dissolution-resistant taxa such as *Globorotalia inflata, G. tumida, Truncorotalia crassaformis, Sphaeroidinella dehiscens, Sphaeroidinellopsis seminulina,* and a few pulleniatinids.

No age determination is made for Sample 198-1213A-6R-CC, which contains rare Neogene (*Sphaeroidinellopsis subdehiscens* and *T. crassaformis*) and Albian–Cenomanian (*Hedbergella delrioensis, Globigerinelloides bentonensis,* and *Hedbergella planispira*) planktonic foraminifers, together with abundant radiolarians, fish teeth, and common crystals of phillipsite.

Cretaceous

Although no keeled species were observed in the small-sized assemblages, an early Santonian age is suggested for Samples 198-1213A-7R-1, 48–50 cm, 7R-1, 85–87 cm, and 198-1213A-7R-CC based on the presence of *Heterohelix planata, Heterohelix carinata,* and *Whiteinella baltica,* together with rare *Hedbergella holmdelensis, Archaeoglobigerina cretacea,* and few schackoinids.

Owing to the poor recovery of the underlying mid to Lower Cretaceous sequence, which consists of chert and porcellanite with interbedded rare chalk, planktonic foraminifers are generally rare and poorly preserved, whereas radiolarians are abundant in most of the studied samples.

Planktonic foraminifers were observed in only a few samples obtained by scraping the relatively soft chalk or limestone from the chert clasts. A few thin sections of the indurated lithologies were also analyzed for planktonic foraminifers. No age-diagnostic species were identified in Sample 198-1213A-8R-CC, which contains rare hedbergellids and schackoinids. Samples 198-1213A-9R-CC and 10H-CC yield a basal Cenomanian assemblage of poorly preserved planktonic foraminifers, including few *Hedbergella delrioensis, H. simplex, H. planispira, Costellagerina libyca, G. bentonensis,* and rare *Praeglobotruncana stephani* and *Rotalipora globotruncanoides,* which permits the identification of the *R. globotruncanoides* Zone (KS17).

The interval between Samples 198-1213A-12R-1, 15–18 cm, and 15R-1, 6–8 cm, contains rare to common planktonic foraminifers. The species identified are *Rotalipora appenninica, Planomalina buxtorfi, H. delrioensis, G. bentonensis, G. ultramicrus,* and a possible *P. stephani.* These taxa indicate the uppermost Albian *R. appenninica* Zone (KS16).

The presence of a single specimen of *Biticinella breggiensis* in Sample 198-1213B-2R-CC may indicate the middle–upper Albian *B. breggiensis* Zone (KS14), in disagreement with the nannofossil datums that indicate an older age (lower Albian) for the same sample.

Rare *Ticinella primula* together with few *H. delrioensis, Ticinella raynaudi, Biticinella praebreggiensis,* and *G. bentonensis* in Samples 198-1213A-21R-1, 148–150 cm, and 198-1213B-3R-CC suggest the *T. primula* Zone (KS13). A poorly preserved upper Aptian assemblage, including rare *Hedbergella trocoidea, Hedbergella maslakovae, "H. delrioensis,"* and possible *Hedbergella infracretacea,* was observed in Sample 198-1213B-6R-1, 83–84 cm. These taxa combined with the absence of *Ticinella bejaouaensis* and *Globigerinelloides algerianus* allow us to assign this section to the *Hedbergella trocoidea* Zone (KS9).

No planktonic foraminifers were observed in Cores 198-1213B-7H and 8H, the latter including the lower Aptian Selli equivalent horizon, whereas Sample 198-1213B-9R-1, 17–18 cm, contains a moderately well-preserved planktonic foraminiferal assemblage of Hauterivian age, including few *Hedbergella sigali, H. aptica, "H. delrioensis,"* and rare globigerinelloidids to indicate the *Hedbergella sigali–"Hedbergella delrioensis"* Zone.

Samples 198-1213B-16R-1, 13–14 cm, and 19R-1, 119–122 cm, contain few radiolarians, some of which are pyritized, together with glauconite, fish teeth, and fish bone. The former sample also contains inoceramid prisms. These features suggest low rates of sedimentation, possibly resulting from current winnowing and/or carbonate dissolution.

Benthic Foraminifers

Benthic foraminifers were examined in core catcher samples of Holes 1213A and 1213B. They are well preserved and few to common in abundance in the Neogene, but generally poorly preserved and trace to rare in abundance in the Cretaceous.

Neogene

In Samples 198-1213A-1R-CC through 4R-CC (Pleistocene–Pliocene), benthic assemblages are characterized by abundant uvigerinids (*Uvigerina hispida, Uvigerina hispidocostata,* and *U. senticosa*). The abundance of these taxa decreases in Sample 198-1213A-5R-CC, and they are replaced by *Anomalinoides globulosus, Cibicidoides wuellerstorfi, Cibicidoides mundulus, Oridorsalis tener, Pullenia bulloides, Pyrgo murrhina, Pyrgo lucernula,* and agglutinated species (*Eggerella bradyi, Karreriella bradyi, Haplophragmoides* spp., and *Martinottiella* sp.). These benthic assemblages are generally similar to those observed at other sites, except for the dominance of uvigerinids. The abundance of *Uvigerina senticosa* in Sample 198-1213A-3R-CC indicates deposition at abyssal depths (>2000 m) (Pflum and Frerichs, 1976).

Cretaceous

Sample 198-1213A-7R-CC (Santonian–Coniacian) contains common but poorly preserved benthic foraminifers with abundant *Aragonia ouezzanensis* and *Gaudryina pyramidata*. These taxa in addition to *Oridorsalis umbonatus,* one of the characteristic taxa in the Late Cretaceous, indicate deposition within lower bathyal to abyssal depths (1500–3500 m) according to Kaiho (1998, 1999).

In Sample 198-1213A-8R-CC, no benthic foraminifers are present. In Sample 198-1213A-9R-CC (upper Albian–lower Cenomanian), the very rare benthic foraminifers belong to trochospiral calcareous species (*Conorotalites aptiensis, Gyroidinoides infracretaceus, Hanzawaia compressa,* and *Protosangularia albiana*). In Sample 198-1213A-21R-1, 0–1 cm, and interval 198-1213B-2R-1, 4–6 cm, through 6R-1, 81–84 cm (Albian–lower Aptian), the benthic assemblages are dominated by abundant trochospiral taxa (*P. albiana, Protosangularia cenomaniana, Gyroidinoides globosus,* and *G. infracretaceus*), *Dentalina* spp., *Lenticulina* spp., and abundant agglutinated species (*Dorothia conula, Dorothia gradata, Gaudryina dividens, Remesella* sp., and *Tritaxia gaultina*). Nodosariids increase in abundance in Sample 198-1213B-6R-1, 81–84 cm. Abundant *Hanzawaia* sp., diverse nodosariids, and *Dorothia praehauteriviana* characterize Sample 198-1213B-9R-1, 9–12 cm. Sliter (1977) suggested that Albian benthic assemblages dominated by gavelinellids, gyroidinoidids, and agglutinated genera indicate deposition at middle to lower bathyal water depths (500–1500 m). According to Kaiho (1998, 1999), *P. albiana,* and *P. cenomaniana* indicate bathymetric ranges of ~1500–2500 and ~2000–3000 m, respectively. In addition, benthic assemblages in Samples 198-1213B-6R-1, 81–84 cm, and 9R-1, 9–12 cm, are similar to late Albian lower bathyal (1000–2000 m) assemblages of Holbourn et al. (2001), which include diverse nodosariids, rotaliids, and agglutinated taxa with calcareous cement.

In intervals 198-1213B-9R-1, 70–71 cm, to 19R-1, 119–122 cm, benthic assemblages are characterized by diverse nodosariids (*Astacolus* spp., *Dentalina* spp., *Frondicularia bettenstaedti, Lenticulina* spp., *Margin-*

ulinopsis spp., *Psilocitharella* spp., *Saracenaria triangularis,* and *Vaginulinopsis* spp.) and agglutinated taxa including *Marssonella praeoxycona* and *D. praehauteriviana.* According to Sliter (1980), assemblages characterized by nodosariids and larger agglutinated species indicate water depths of <500 m.

Samples 198-1213B-20R-1, 31–33 cm, to 25R-1, 29–49 cm, contain mainly nodosariids, *Dentalina* spp., and *Lenticulina* spp. These nodosariid-dominated assemblages are indicative of 100- to 1000-m depths, in agreement with the absence of larger symbiont-bearing foraminifers. The presence of fish debris, glauconite, and prisms of inoceramids in Samples 198-1213B-16R-1, 12–14 cm, 19R-1, 119–122 cm, and 21R-1, 148–150 cm, suggests that the depositional environment was under the influence of strong bottom currents (Sliter, 1977).

In summary, paleodepths of Site 1213 show a deepening trend during the Early Cretaceous. Undated shallow-water limestones (containing rudists and corals) dredged from the Southern High (Sager et al., 1999) suggest that this part of Shatsky Rise was near sea level early in its history (Late? Jurassic) before subsiding to middle or lower bathyal depths by Aptian–Albian time.

Radiolarians

The Lower Cretaceous sequence at Site 1213 is rich in radiolarians that can provide useful biostratigraphic information. Radiolarian preservation is typically moderate to poor. However, well-preserved specimens were recovered in samples from Cores 198-1213B-6R, 10R, and 12R. Radiolarian tests are replaced by calcite and a minor amount of pyrite throughout the lower part of the sequence. Rarely, radiolarian tests are filled with silica or calcite and the outer skeleton is dissolved. However, most samples contain specimens with visible diagnostic morphological features.

According to Baumgartner et al. (1995), 10 radiolarian Unitary Association Zones (UAZs) characterize the Lower Cretaceous and can be used for biostratigraphic correlation (see **"Biostratigraphy,"** p. 9, in the "Explanatory Notes" chapter). Zones UAZ13 to UAZ22, spanning the stratigraphic interval from lower Aptian to lowermost Berriasian, could be identified in Cores 198-1213B-12R through 27R. In addition, Cores 198-1213B-5R and 6R yield a younger assemblage, not formally zoned yet, of late early to late Aptian age. This radiolarian assemblage is informally called the "late early to late Aptian assemblage zone" (see **"Sedimentation and Accumulation Rates,"** p. 25).

The upper lower Aptian to upper Aptian assemblage zone (Samples 198-1213B-5R-1, 0–3 cm, and 6R-1, 81–84 cm) is characterized by *Archaeodictyomitra chalilovi, Anomalinoides simplex, Crucella* sp. EJ 1 sensu Erbacher (1994), *Eucyrtis micropora, Novixitus*(?) *daneliani, Thanarla conica,* and *T. elegantissima* sensu Sanfilippo and Riedel (see Baumgartner et al., 1995).

Zone UAZ22 (Sample 198-1213B-8R-1, 45–46 cm) is characterized by *Archaeodictyomitra excellens, Cryptamphorella clivosa, Dictyomitra pseudoscalaris* sensu Schaaf, *Godia lenticulata, Paronaella trifoliacea, Pseudodictyomitra lanceloti, Sethocapsa*(?) *orca, Sethocapsa simplex, Thanarla elegantissima,* and *T. pulchra* sensu Sanfilippo and Riedel (see Baumgartner et al., 1995), whereas the genus *Pantanellium* is not present. This assemblage suggests a late Barremian to early Aptian age and possibly is correlative with the upper OAE1a interval because the LO of *Pantanellium* is restricted to the lower part of the Selli level in the Tethys (Erbacher and Thurow, 1997).

Zone UAZ20 (Samples 198-1213B-10R-1, 21–22 cm, and 12R-1, 9–12 cm) is characterized by *Homoeoparonaella peteri, Pseudocrolanium fluegeli, Bernoullius*(?) *monoceros, Mirifusus dianae minor, S. simplex, S.*(?) *orca, A. chalilovi, T. elegantissima, T. pulchra,* and *Podobursa multispina.* This assemblage indicates an age of late Hauterivian to early Barremian. Sample 198-1213B-14R-1, 17–19 cm, is assigned to Zone UAZ17 and is of late Valanginian to early Hauterivian age based on the presence of *D. pseudoscalaris, Hemicryptocapsa capita, Obesacapsula cetia, Oesacapsula morroensis, T. pulchra,* and *Wrangellium puga.* Zones UAZ15 to UAZ17 could not be differentiated in Sample 198-1213B-15R-1, 15–16 cm. This sample contains *Angulobracchia*(?) *portamanni portamanni, Emiluvia chica decussata, P. squinaboli, S. trachyostraca,* and *S. vicetina,* which suggest an age of late Berriasian to early Hauterivian.

Upper Berriasian–lower Valanginian Zone UAZ15 is recognized in Samples 198-1213B-17R-1, 0–1 cm, 19R-1, 119–122 cm, 20R-1, 31–33 cm, and 22R-1, 58–60 cm, based on the presence of *Acanthocircus furiosus, H. feliformis, Jacus*(?) *italicus, O. bullata, P. squinaboli, S. trachyostraca, S. uterculus* sensu Foreman (see Baumgartner et al., 1995), *Syringocapsa agolarium,* and *Thanarla pulchra.*

Zones UAZ12 through UAZ14 (Samples 198-1213B-25R-1, 37–40 cm, and 27R-1, 21–22 cm) are characterized by *Acanthocircus*(?) *portamanni portamanni, Archaeodictyomitra apiarium, O. morroensis, P. squinaboli, Paevicingula sphaerica, Pseudodictyomitra carpatica, S. agolarium,* and *Wrangellium depressum.* Sample 198-1213B-25R-1, 37–40 cm, yields distinctive species, including *Mirifusus dianae dianae, Napora* sp. aff. *boneti,* and other *Mirifusus* spp. which characterize Upper Jurassic Zones UAZ10–UAZ12. However, the co-occurrence of *M. dianae dianae* (Zones UAZ7–UAZ12) and *W. depressum* (Zones UAZ13–UAZ18) suggests a late Tithonian age. Therefore, it is possible that the lowermost part of Hole 1213B is latest Jurassic in age; however, specimens of *M. dianae dianae* may also be reworked.

PALEOMAGNETISM

No paleomagnetic measurements were made from sediments or sedimentary rocks recovered from Holes 1213A and 1213B. Soft sediment cores from Hole 1213A were deemed to be too disturbed for reliable measurements. Cores from below the Tertiary–Cretaceous unconformity had low recovery and consisted of small pieces of chert with associated limestone and other types of sedimentary rock. These rock pieces are too small and lack the continuity in recovery to make pass-through measurements useful.

Igneous rocks from the six cores at the bottom of Hole 1213B were measured on the pass-through magnetometer because many of the core sections contained large pieces of contiguous basaltic rock. These cores were measured three to seven times, recording the natural remanent magnetization (NRM) and the magnetization at several different levels of alternating-field (AF) demagnetization. Typically, the AF steps used were 10, 20, 25, and 30 mT, although a few sections were taken as high as 35 mT. During analysis, measurements from zones with no oriented pieces, with small fragments, and near the ends of the larger fragments were excluded to remove inaccurate values resulting from the averaging of nearby pieces with different orientations.

NRM intensities for the igneous rocks fall within a narrow range close to ~1–10 A/m. After demagnetization to 30 mT, the intensities dropped to ~2.5×10^{-2} to 4×10^{-1} A/m. It was noted that magnetic inclinations changed between the 20, 25, and 30 mT demagnetization steps, implying that the characteristic remanent magnetization has not been completely isolated. Therefore, more detailed shore-based measurements will be necessary to obtain reliable magnetization directions. After demagnetization at peak fields of 30 mT, magnetic inclinations in Cores 198-1213B-28R to 32R are all positive (Fig. F26), implying normal polarity if magnetized north of the equator. The positive inclinations are all much steeper than expected for the near-equatorial position that Shatsky Rise is thought to have occupied during the Late Jurassic and Early Cretaceous (Larson et al., 1992; Sager et al., 1999). Most of the section averages for Cores 198-1213B-28R through 32R are between 50° and 70°. The cause of the steep inclinations is unclear. Measurements from Core 198-1213B-33R show negative inclinations (Fig. F26), indicating reversed polarity if the magnetization was acquired north of the equator. The inclination values are ~–30°, a value more in line with a low paleolatitude (~13°N). The apparent reversed polarity implies that this particular sill (Subunit IVC) was not emplaced during the Cretaceous Long Normal Superchron (i.e, Cretaceous Quiet Period; 83–121 Ma; see **“Paleomagnetism,”** p. 13, in the “Explanatory Notes” chapter for timescale), when many other similar sills were formed in the western Pacific (Schlanger and Moberly, 1986; Floyd et al., 1992).

SEDIMENTATION AND ACCUMULATION RATES

Unconformities and changes in sedimentation rate at Site 1213 are illustrated in a plot of calcareous microfossil datum ages (FOs and LOs) vs. depth (Fig. F27). These rates rely on major calcareous nannofossil and planktonic foraminiferal datums presented in Tables T5 and T6 (see **“Biostratigraphy,”** p. 18). The Pleistocene–basal Cretaceous or uppermost Jurassic section cored at Site 1213 is punctuated by at least two unconformities separating the lower Pliocene and lower Santonian and the lower Santonian and mid- to upper Cenomanian.

An expanded view of the Neogene (Fig. F28) shows that the mid- to lower Pliocene section accumulated at a rate of ~5.5 m/m.y., increasing to 14.6 m/m.y. in the upper Pliocene–Pleistocene. Dark-colored clay-rich sediments in Core 198-1213A-6R record condensed basal Pliocene (and upper Miocene?) sedimentation overlying the major upper Neogene/Upper Cretaceous unconformity (Figs. F28, F29).

Core 198-1213A-7R contains <1 m of lower Santonian chalk bounded by two major unconformities, with lower Pliocene (and upper Miocene?) above and mid- to upper Cenomanian below (Fig. F29). Core recovery was poor throughout the Cretaceous section, but all cores yielded datable calcareous nannofossil assemblages, which were supported by planktonic foraminifers and/or radiolarians (see **“Biostratigraphy,”** p. 18). The mid-Cenomanian–upper Albian sediments accumulated at an average rate of 21.2 m/m.y. The interval from near OAE1a in the lower Aptian through the middle Albian accumulated at a reduced rate of 4.7 m/m.y. The basal Aptian–upper Hauterivian is either missing at Site 1213 or is represented by an unrecovered condensed interval (sedimentation rates of ~1.1 m/m.y.). Sedimentation rate estimates for the lower Hauterivian–Berriasian interval range between 12.3 and 16.2

F26. Plot of magnetic inclination vs. depth for the igneous section, Hole 1213B, p. 72.

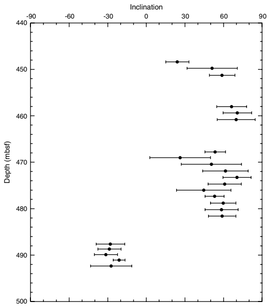

F27. Age-depth plot of calcareous nannofossil and planktonic foraminiferal datums, p. 73.

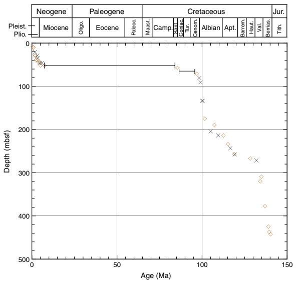

F28. Age-depth plot of Neogene calcareous nannofossil and planktonic foraminiferal datums, p. 74.

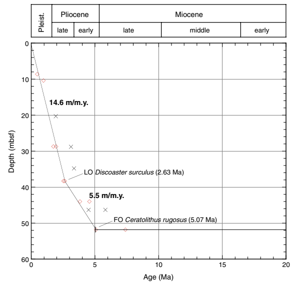

F29. Age-depth plot of Late Cretaceous–latest Jurassic calcareous nannofossil and planktonic foraminiferal datums, p. 75.

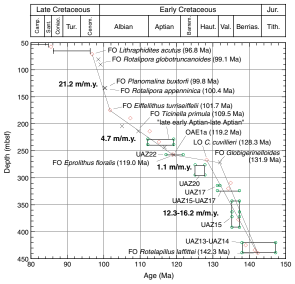

m/m.y. based on the combined evidence of calcareous nannofossils, radiolarians, and planktonic foraminifers (Fig. **F29**).

ORGANIC GEOCHEMISTRY

Volatile Hydrocarbons

Headspace gas analysis was conducted as part of the standard protocol required for shipboard safety and pollution prevention monitoring. A total of five cores from Hole 1213A were evaluated (Table **T9**). The concentrations of CH_4 were at background levels (range = 1.8–2.1 µL/L [ppmv]); no hydrocarbon gases higher than C_1 were detected.

T9. Headspace CH_4 concentrations, p. 100.

Carbonate and Organic Carbon

Carbonate determinations by coulometry were made for a total of 14 samples from Hole 1213A and 16 samples from Hole 1213B (Table **T10;** Fig. **F30**). Samples were selected to provide a measure of the carbonate content within different units.

T10. Carbonate content, p. 101.

The values for carbonate range from 11 to 80 wt% (Table **T10**) in Unit I, reflecting variations in the proportions of clay. The intervals with low values are condensed sections enriched in clay. Carbonate contents in the Cretaceous nannofossil chalks from Unit III range from 0.4 to 96 wt%. The lowest values correspond to lower Aptian organic-rich claystones deposited during OAE1a; variations derive from differences in clay and biogenic silica contents.

F30. Carbonate profile, p. 76.

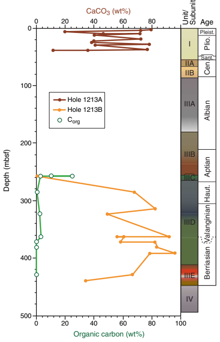

Elemental concentrations of C, H, N, and S were measured (Table **T11**) for nine samples from the lower Aptian to lower Valanginian (Subunits IIIC–IIIE) to assess the enrichment of organic matter within discrete intervals. In some samples, the darker horizons appear as stringers finely intercalated within carbonates; these prove to be lean in organic matter (0–0.4 wt%). The contents of organic carbon are highest in the lower Aptian samples. The two samples taken from the principal carbonaceous interval that correlates to OAE1a contain 25.2 and 10.2 wt% organic carbon. A third sample of clayey porcellanite interbedded with green claystone from lower in the section (Sample 198-1213B-8R-1, 96–97 cm) contains 2.9 wt% C_{org}. The organic carbon contents of C_{org}-rich intervals from the Valanginian were comparable (2.5 and 3.1 wt%). These horizons correspond to a minor peak in gamma ray logs (Fig. **F39**), whereas two more significant peaks are observed within the lower Aptian. The S contents of organic-rich layers range from 0.76 to 5.18 wt%; the highest value corresponds to the lower Valanginian horizon (Table **T11**). The C/N ratios of the organic-rich intervals range from 14.9 to 25.9 and are comparable to those reported for Site 1207, in part reflecting the different character of nitrogen cycling in these organic-rich intervals.

T11. CNSH analysis of samples from OAE1a, p. 102.

Rock-Eval Pyrolysis

The focus for Rock-Eval investigations are samples from C_{org}-rich intervals, including the early OAE1a. The aim is to assess the origins of their kerogens, their thermal maturity and enable comparisons with Aptian C_{org}-rich intervals recovered at other sites.

The hydrogen index (HI) and oxygen index (OI) values for two of the lower Aptian samples (198-1213B-8R-1, 47–48 cm, and 63–64 cm) (Table **T12**) are similar despite the significant difference in their organic carbon contents (Table **T11**). High HI and extremely low OI values confirm that they are composed of type I organic matter (Fig. **F31**) (Tissot et al., 1974) derived from algal and bacterial sources. They are also similar to the lower Aptian samples from Site 1207 and the more C_{org}-rich intervals from Site 463 (Fig. **F31**). By contrast, the higher OI for the lower Aptian sample at 198-1213B-8R-1, 96–97 cm, which was interbedded with green claystone, is closer to type II kerogen. The high OI values for both Valanginian samples (198-1213B-15R-1, 9–10 cm, and 19R-1, 112–113 cm, respectively) (Table **T12**) can be attributed to the ineffectiveness of the Rock-Eval to fully exclude contributions from carbonate that enhance the S_3 peak. This effect is well demonstrated by Sample 198-1213B-11R-1, 61–62 cm, which contained 65 wt% carbonate (Table **T10**). Consequently, the positions of these samples on the modified van Krevelen diagram are unrealistic. Unfortunately, the limited sample size precluded a second analysis after carbonate removal. The T_{max} values, notably the exceptionally low value of 404°C for Sample 198-1213B-8R-1, 63–64 cm, attest to the thermal immaturity of these samples.

T12. Organic carbon and Rock-Eval pyrolysis, p. 103.

F31. Oxygen and hydrogen indices, p. 77.

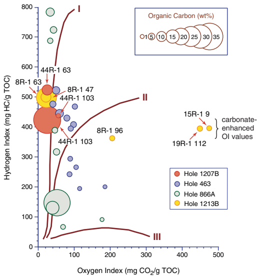

Assessment of Extractable Hydrocarbons and Ketones

Hydrocarbon compositions were examined in samples (~1–4 g) from the lower Aptian (Samples 198-1213B-8R-1, 47–48, 63–64, and 96–97 cm), Valanginian (Samples 198-1213B-15R-1, 9–10 cm, and 19R-1, 112–113 cm) containing elevated C_{org} contents (>2 wt%) (Table **T11**). The information obtained provides evidence of the biological sources and thermal maturity of the organic matter and of the likely depositional environment. The procedure followed the methodology described in **"Organic Geochemistry,"** p. 18, in the "Explanatory Notes" chapter. In addition, gas chromatography-mass spectrometry (GC-MS) was used to examine the composition of CH_2Cl_2 eluates from the silica separation step of the samples consisting primarily of ketones.

The color of the extracts reflected their organic carbon contents. In particular, the color of the most C_{org}-rich horizons (Sample 198-1213B-8R-1, 63–64 cm) was intense for such a small sample size. During sample preparation by chromatographic separation, a pronounced pink coloration was also evident in the polar (CH_2Cl_2) eluants of Samples 198-1213B-15R-1, 9–10 cm, and 19R-1, 112–113 cm, suggesting that they contain high concentrations of porphyrins. The same eluate for another sample (198-1213B-8R-1, 96–97 cm) produced an intense yellow coloration, which could be associated with carotenoids, but their presence could not be confirmed by GC-MS. Both hexane and CH_2Cl_2 eluants, primarily consisting of aliphatic hydrocarbons and ketones, respectively, were analyzed by GC-MS, and their components were identified from responses at specific target intervals in individual ion chromatograms and from their mass spectra. All of the hydrocarbons are well documented as components of mid-Cretaceous black shales elsewhere (e.g., Barnes et al., 1979; Brassell, 1984; Rullkötter et al., 1984, 1987; Farrimond et al., 1986b, 1990; Simoneit, 1986). There are fewer published identifications of ketones in sedimentary rocks of this age (Comet et al., 1981; Farrimond et al., 1986a). Consideration of the principal characteristics of the samples (Table **T13**) and their relative abundances of biomarker components (Table **T14**) enables assessment and interpretation of aspects of the depositional environment of OAE1a and comparison with other intervals enriched in organic matter.

T13. Biomarkers and compound ratios, p. 104.

T14. Biomarker carbon number ranges and relative abundances, p. 105.

Source of Organic Matter and Depositional Paleoenvironment

The extractable hydrocarbons are dominated by biomarkers of algal and bacterial origin, including short-chain *n*-alkanes and suites of polycyclic steroid and hopanoid hydrocarbons (Figs. F32, F33; Tables T15, T16). In the lower Aptian samples, the abundance of *n*-C_{17}, complemented by occurrences of methylhopanes, provides evidence for contributions from cyanobacteria. The steroids and hopanoids are derived from eukaryotic algae and bacteria, respectively (see Table T15, p. 131, in the "Site 1207" chapter), although the absence of 4-methyl steroidal hydrocarbons suggests that dinoflagellates (Brassell and Eglinton, 1983; Robinson et al., 1984; Summons et al., 1987) were sparse among the plankton community. The occurrence of alkenones in Sample 198-1213B-8R-1, 63–64 cm, further extends the temporal record of these markers for haptophyte algae (Farrimond et al., 1986a; Marlowe et al., 1990; Brassell, 1993). Their abundance, in concert with that of other functionalized lipids, strongly suggests that alkatrienones are unlikely to have been lost as a result of diagenetic alteration (cf. Farrimond et al., 1986a; Prahl et al., 1989; Hoefs et al., 1998). Thus, the absence of alkatrienones may reflect sea-surface temperatures that are elevated (i.e., >28°C) above the range where the composition of alkenones responds to temperature variations (Brassell et al., 1986; Prahl et al., 1988; Müller et al., 1998). Alternatively, this interval may precede the advent of temperature regulation of alkenone production and potentially the evolution of alkatrienone biosynthesis (S.C. Brassell, unpubl. data). The presence of sterol ethers in Sample 198-1213B-19R-1, 112 cm, is unprecedented in the Cretaceous (cf. Boon and de Leeuw, 1979; Brassell et al., 1980), although the origin of these components remains enigmatic (Brassell and Eglinton, 1986).

The only indication of allochthonous materials is the trace amounts of C_{25+} *n*-alkanes with pronounced odd/even preference that likely reflect input of vascular plant waxes borne by eolian dust (Simoneit, 1978; Zafiriou et al., 1985; Gagosian and Peltzer, 1986; Gagosian et al., 1987). The prevalence and character of bacterial components in the lower Aptian samples is again (cf. "Organic Geochemistry," p. 27, in the "Site 1207" chapter) consistent with the existence of a microbial mat, perhaps akin to those of the sulfur-oxidizing bacteria *Thioploca* in benthic settings (Williams and Reimers, 1983; McCaffrey et al., 1989; Ferdelman et al., 1997). The pristane/phytane ratios are less than unity (Table T13), which is typical of sediments associated with oxygen-depleted systems (Didyk et al., 1978). In contrast, the occurrence of suites of steroidal ketones (Fig. F33; Table T13) provides circumstantial evidence for oxidation of precursor lipids (Simoneit, 1973) or food web processes within the water column. However, they can also be biosynthetic products (Gagosian et al., 1982; Brassell and Eglinton, 1983; Robinson et al., 1984; Brassell et al., 1987) and, consequently, cannot provide conclusive, independent evidence of oxygenation levels in the water column or underlying sediments. Certainly, the high total organic carbon (TOC) content and high HI of lower Aptian sedimentary rocks at Site 1213 suggest anoxic bottom-water conditions, but the lack of fine lamination and presence of burrows indicate at least periodic oxygenation at the sediment/water interface (see "Lithostratigraphy," p. 8).

F32. GC-MS traces of aliphatic hydrocarbons, p. 78.

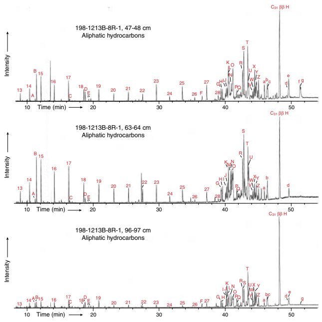

F33. GC-MS traces of ketone fractions, p. 80.

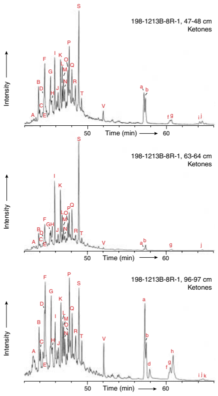

T15. Identities of hydrocarbon components, p. 106.

T16. Identities of ketone components, p. 107.

The catalog of biomarkers identified in the samples derive entirely from bacterial and/or algal sources (Table T14), consistent with the results from Rock-Eval pyrolysis.

Depositional Scenarios for OAE1a

The biomarker results from Site 1213 yield important information on the depositional conditions during early Aptian OAE1a. All of the C_{org}-rich intervals contain an abundance of steroidal ketones and suites of steroidal and hopanoid aliphatic hydrocarbons, which suggests a degree of uniformity in the contributions of organic matter, despite differences in organic carbon content. The steroids, in particular, reflect inputs from eukaryotes and are predominantly derived from planktonic algae, modified by water column predation. Steroidal ketones are abundant in the upwelling systems off Peru and Southwest Africa (Gagosian and Smith, 1979; Gagosian et al., 1983; Smith et al., 1983). There are also individual distinctive features, specifically the occurrence of alkenones and sterol ethers in Samples 198-1213B-8R-1, 96–97 cm, and 15R-1, 9–10 cm, respectively. Two specific features, however, distinguish the lower Aptian samples at Site 1213 and Site 1207 from the other organic-rich horizons, namely the presence of suites of methylhopanoids and extended hopanoids and the relative abundance of phytane and phytenyl lipids (phytenes at Site 1213 and phytenyl thiophenes at Site 1207). These characteristics can be attributed to contributions of organic matter from cyanobacteria and from methylotrophic and methanogenic bacteria. They imply the presence of specific bacterial communities associated with OAE1a, which in turn may reflect dysoxic conditions. However, the overall uniformity in the distributions of the dominant biomarkers, namely steroidal ketones, suggests that the populations of oceanic phytoplankton were stable over the time span represented by the samples. Yet, the higher prominence of Δ4-sterones relative to 5α(H)-stanones in Samples 198-1213B-8R-1, 47–48 cm, and 63–64 cm (Table T13), potentially reflect enhanced anaerobic sterol degradation observed in microbial mats (Edmunds et al., 1980).

The extraordinary sequestration of organic matter (>25 wt%) reflects a perturbation of the ocean-climate system that radically changed the processes controlling biogeochemical cycling. The potential roles of increased productivity and enhanced preservation in contributing to the survival of elevated amounts of organic matter are not easily distinguished. Yet, the majority of indicators for plankton productivity suggest only minor temporal variations in their populations, whereas the occurrence of components derived from bacteria suggests a change in the processing of organic matter at higher trophic levels. This evidence is most consistent with the concept that exceptional preservation of organic matter derived from algal and bacterial sources was aided by anoxic conditions.

INORGANIC GEOCHEMISTRY

Interstitial Water Chemistry

Five interstitial water samples were collected from a thin drape of Neogene sediments (0–66.1 mbsf) that unconformably overlies an Upper to Lower Cretaceous sequence. Details of analytical methods can be found in **"Inorganic Geochemistry,"** p. 21, in the "Explanatory Notes" chapter. Filtered (0.45 µm) samples were analyzed for pH, salinity, chlorinity, alkalinity, sulfate (SO_4^{2-}), phosphate (HPO_4^{2-}), ammonium (NH_4^+), silica ($Si(OH)_4$), boron (H_3BO_3), iron (Fe^{2+}), manganese (Mn^{2+}), and major cations (Na^+, K^+, Mg^{2+}, Ca^{2+}, Li^+, Sr^{2+}, and Ba^{2+}). A compilation of data is provided in Table **T17.**

Rotary coring at Site 1213 caused significant disturbance of Cores 198-1213A-1R to 7R, making it difficult to recognize primary sedimentary structures and textures (see **"Lithostratigraphy,"** p. 8). The drilling disturbance appears to have also affected the samples obtained for interstitial water analyses, most of which have seawater-like chemistries but elevated Fe^{2+} and Mn^{2+} concentrations (Table **T17**). As such, the geochemical results suggest that samples consist of varying mixtures of pore water and drilling water (i.e., surface seawater) and do not provide a reliable reflection of sediment geochemistry and diagenetic processes at Site 1213.

PHYSICAL PROPERTIES

Physical properties at Site 1213 were measured on both whole-round sections and discrete samples from split-core sections. Because of poor core recovery at Site 1213, only a limited number of cores were measured on the multisensor track (MST). The MST records of magnetic susceptibility, gamma ray attenuation (GRA) bulk density and natural gamma radiation thus have poor stratigraphic coverage. Discrete measurements of compressional *P*-wave velocity were made at a routine frequency of at least one measurement per split-core section in Holes 1213A and 1213B. No index properties measurements were made at Site 1213.

MST Measurements

Whole-round core sections from Holes 1213A and 1213B were routinely measured on the MST for magnetic susceptibility and GRA bulk density at 3-cm intervals in Cores 198-1213A-1R to 7R and 198-1213B-8R to 10R and 27R (Figs. **F34; F35**). In Cores 198-1213B-28R to 33R, magnetic susceptibility and GRA bulk density were measured at 5-cm intervals. Natural gamma radiation was measured at 5-cm intervals (with a count time of 10 s) in Cores 198-1213B-8R through 10R and 27R through 33R (Fig. **F36**). All collected MST data are archived in the ODP Janus database.

Hole 1213A magnetic susceptibility values appear to display no discernible downhole trend, although relatively higher values are recorded at ~9 and ~51 mbsf, and these intervals may correlate with ash layers (Fig. **F34**). The magnitude of Hole 1213A magnetic susceptibility data are comparable with values measured in the Pleistocene–Pliocene interval at other Leg 198 sites (see **"Physical Properties,"** p. 37, in the "Site 1207" chapter; **"Physical Properties,"** p. 28, in the "Site 1208" chapter; **"Physical Properties,"** p. 29, in the "Site 1209" chapter; **"Physical Properties,"** p. 26, in the "Site 1210" chapter; **"Physical Properties,"** p. 25, in the "Site 1211" chapter; and **"Physical Properties,"** p. 23, in the "Site 1212" chapter). In cores from Hole 1213B, magnetic susceptibility values are close to background in the lower Aptian–Hauterivian (~257 to ~276 mbsf) (Fig. **F34**) but are slightly higher in the basal Berri-

T17. Data collected at Site 1213, p. 108.

F34. Whole-core MST magnetic susceptibility, p. 82.

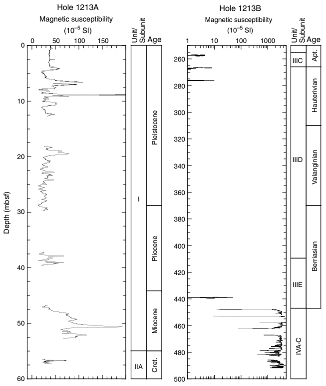

F35. Whole-core MST GRA bulk density, p. 83.

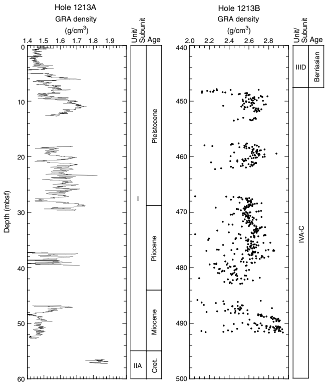

F36. MST natural gamma radiation, p. 84.

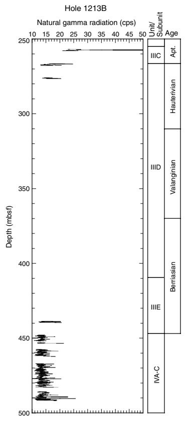

asian (~439 mbsf). Below ~447 mbsf in Hole 1213B, the diabase has magnetic susceptibility values in excess of 2000 × 10^{-5} SI.

GRA bulk density data show a slight downhole increase between the seafloor and ~11 mbsf (Fig. **F35**). Between ~11 and ~15 mbsf, GRA bulk density values decrease, and then from ~18 to 27 mbsf GRA bulk density values increase slightly. GRA bulk density values appear to decrease between ~37 and ~52 mbsf. A stepped downhole increase in GRA bulk density occurs across the boundary between lithologic Units I and II at 54.6 mbsf, which represents an unconformity between the Santonian and the lower Pliocene (see **"Biostratigraphy,"** p. 18). GRA bulk density was not measured between ~57 and ~447 mbsf, due to the poor recovery of sediments. Between ~447 and ~494 mbsf, at least three units of diabase were recovered, and within these igneous rocks (Subunits IVA–IVC) a slight downhole increase in GRA bulk density values is evident. A number of low values in the GRA bulk density data obtained for the ~447 to ~494 mbsf interval may be due to cracks, veins, and/or poor contact between the liner and the diabase.

Natural gamma radiation was measured in the Hole 1213B Lower Cretaceous sediments and diabase only (Fig. **F36**). At ~254 mbsf, high natural gamma radiation values are recorded that correspond with a lower Aptian black shale (see **"Lithostratigraphy,"** p. 8) that contains a high amount of organic carbon (see **"Organic Geochemistry,"** p. 26). Other Lower Cretaceous cores that were measured for natural gamma radiation (Cores 198-1213B-9R, 10R, and 27R) have fairly constant values and show no obvious downhole trend. Natural gamma radiation values in the diabase (lithologic Subunits IVA–IVC) (see **"Lithostratigraphy,"** p. 8) are fairly constant downhole, but absolute values are slightly lower than those in the Lower Cretaceous sediments.

P-Wave Velocity

Discrete measurements of compressional *P*-wave velocity were made on Site 1213 split-core sections using the modified Hamilton Frame (PWS3) velocimeter. These data are listed in Table **T18** and illustrated in Figure **F37.** Data were collected at a routine sampling frequency of one measurement per section. A variety of lithologies were cored at Site 1213, each of which have distinct *P*-wave velocities (Table **T19**). Within the recovered sediments, there is a general downhole increase in *P*-wave velocity between 0 and ~60 mbsf, and this is most likely related to progressive sediment compaction and dewatering with increasing burial depth. An increase in *P*-wave velocity occurs at ~57 mbsf, within the uppermost part of Cretaceous Subunit IIA. Between ~240 and ~440 mbsf, a general downhole increase in the *P*-wave velocities of chalk and limestone sediments relates to increased lithification with greater burial depth. Downhole trends in the *P*-wave data obtained for chert, porcellanite, radiolarite, and diabase lithologies are not evident at Site 1213 (Fig. **F37**).

T18. Discrete measurements of *P*-wave velocity, p. 109.

F37. Discrete *P*-wave velocities, p. 85.

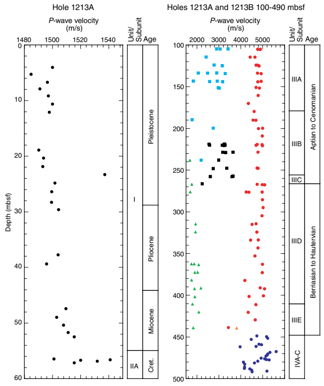

Summary

Physical properties data from Site 1213 primarily reflect the compositional variability between the different sediments and igneous rocks recovered. Data from the recovered sediments are diagnostic both of the depth of burial (i.e., degree of lithification) and also the amount of silicification. The high degree of variability of *P*-wave velocities below 100

T19. Minimum, maximum, and average *P*-wave velocities, p. 110.

mbsf, which is related to lithology, has significant implications for seismic interpretations of Site 1213 and related stratigraphic sections.

DOWNHOLE MEASUREMENTS

Operations

Downhole measurements in Hole 1213B were made after the completion of RCB coring to a total depth of 494.9 mbsf. Prior to logging, a wiper trip was made with the drill string, and the hole was flushed of debris and filled with sepiolite mud. During the wiper trip, the BHA reentered the igneous rocks in the lower 45 m of the hole only with some difficulty. The triple-combo tool string (porosity, density, resistivity, and natural gamma radiation) (see **"Wireline Logging,"** p. 27, in "Downhole Measurements," Fig. F8, p. 53, and Table T7, p. 62, all in the "Explanatory Notes" chapter) was successfully lowered to 431 mbsf, 64 m short of the total hole depth. During the uplog, between 312 and 324 mbsf, the hole apparently narrowed to <5 in wide; this obstruction had not been noted on the downward passage of the tool. High cable tension was encountered at 188 mbsf, and the logging run had to be stopped at this point, where it was also discovered that the caliper arm on the density tool would not close. After ~20 min of working the tool, it came free and was brought into the pipe and up to the ship. The most likely explanation for the difficulties in logging the hole is that pieces of chert fell out of the borehole wall and down the hole. There was no time for further logging runs because an approaching storm forced us to leave the site.

In the 240-m-long logged interval, the tools provided continuous, high-quality log data. The borehole diameter ranged from 11 in at the base of the hole to a maximum of 17 in at 305 mbsf. The hole contained ledges that formed at the hard chert layers, with the relatively soft ooze or chalk in between preferentially washed away. The wireline depth to seafloor was not determined.

Logging Units

Hole 1213B was divided into six units on the basis of the logs (Figs. F38, F39).

Logging Unit 1: Top of Logs (188 mbsf) to 238 mbsf

Unit 1 is characterized by high resistivity values, generally high densities, and a generally narrow hole diameter, all implying quite well lithified sediment.

Logging Unit 2: 238–251 mbsf

Unit 2 is characterized by low resistivity values compared to the units above and below. The hole is wider in this unit, implying that it is more easily washed away and less lithified.

Logging Unit 3: 251–268 mbsf

This unit has high resistivities and high gamma radiation values, including a double peak in uranium at 257.5 and 259.5 mbsf (Fig. F39). Potassium is also high in this interval, indicating that it is more clay

F38. Geophysical logs and equivalent core physical properties measurements, Hole 1213B, p. 86.

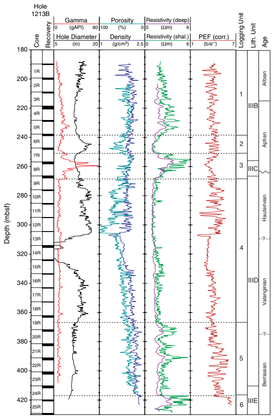

F39. Geochemical logs, Hole 1213B, p. 87.

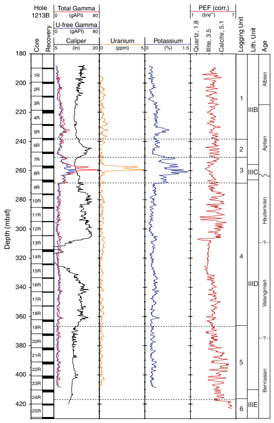

rich than the other units. Units 1, 2, and 3 at this site bear similarity to Units 4, 5, and 6 at Site 1207 (Fig. **F40**).

F40. Gamma radiation and resistivity logs, Aptian sediments, Holes 1213B and 1207B, p. 88.

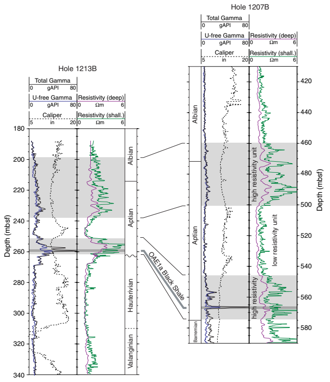

Logging Unit 4: 268–367 mbsf

This unit is characterized by generally low resistivities and low gamma radiation values.

Logging Unit 5: 367–417 mbsf

This unit is characterized by generally high resistivities, high densities, and low gamma radiation values.

Logging Unit 6: 417 mbsf to the Base of Logs (428 mbsf)

Unit 6 is characterized by higher resistivity values than the unit above, and uniformly high densities. It is probably a limestone.

Black Shales

The lower Aptian black shales recovered in Core 198-1213B-8R are represented in the logs by two large peaks in gamma radiation at 257.5 and 259.5 mbsf (Fig. **F41**). Uranium is the main contributor to the gamma radiation peaks; uranium peaks are often associated with black shales because the uranium is adsorbed by organic matter in the shale. Only the lower of the two uranium peaks is accompanied by low density values. Using the same equations presented in **"Black Shales,"** p. 42, in "Downhole Measurements" in the "Site 1207" chapter, the low density indicates that the peak has an organic matter content of ~9 wt%. This value falls within the range for TOC determined from core analysis (see **"Carbonate and Organic Carbon,"** p. 26, in "Organic Geochemistry"). The shale is ~0.9 m thick, according to the uranium, porosity, and density logs.

F41. Detail of gamma radiation, density, and porosity logs around OAE1a black shale interval, p. 89.

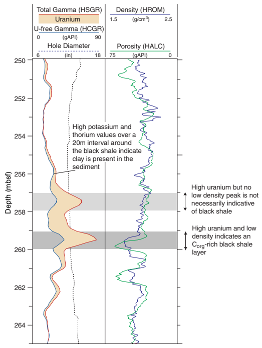

The interval in which the shales occur is relatively rich in potassium, which is in clay minerals like illite. If the potassium content is 1 wt% and all the potassium is in illite, the matrix would be ~20 wt% illite. The other major clay minerals have lower potassium contents. As at Site 1207, the black shale occurs within a high-resistivity unit (Fig. **F40**). The higher resistivity is probably caused by increased cementation of the chalk, or perhaps by increased concentration of chert layers, in this interval.

As in Hole 1207B, there are no other gamma radiation peaks of the same magnitude in the Cretaceous section at Hole 1213B. There are some minor peaks, such as the potassium peak at 361 mbsf, which may be related to the lower Valanginian shale found in Core 198-1213-19R. The shale recovered in Core 198-1213B-15R is not represented in the logs. However, the general conclusion is that, of the Cretaceous OAEs observed elsewhere, only OAE1a is significantly represented at Shatsky Rise.

REFERENCES

Arthur, M.A., and Dean, W.E., 1986. Cretaceous paleoceanography. *In* Tucholke, B.E., and Vogt, P.R. (Eds.), *Decade of North American Geology, Western North Atlantic Basin Synthesis Volume.* Geol. Soc. Am., 617–630.

Barnes, P.J., Brassell, S.C., Comet, P., Eglinton, G., McEvoy, J., Maxwell, J.R., Wardroper, A.M.K., and Volkman, J.K., 1979. Preliminary lipid analysis of core sections 18, 24, and 30 from Hole 402A. *In* Montadert, L., Roberts, D.G., et al., *Init. Repts. DSDP,* 48: Washington (U.S. Govt. Printing Office), 965–976.

Baumgartner, P.O., Bartolini, A., Carter, E.S., Conti, M., Cortese, G., Danelian, T., De Wever, P., Dumitrica, P., Dumitrica-Jud, R., Gorican, S., Guex, J., Hull, D.M., Kito, N., Marcucci, M., Matsuoka, A., Murchey, B., O'Dogherty, L., Savary, J., Vishnevskaya, V., Widz, D., and Yao, A., 1995. Middle Jurassic to Early Cretaceous radiolarian biochronology of Tethys based on unitary associations. *In* Baumgartner, P.O., O'Dogherty, L., Gorican, S., Urquhart, E., Pillevuit, A., and De Wever, P. (Eds.), *Middle Jurassic to Lower Cretaceous Radiolaria of Tethys: Occurrences, Systematics, Biochronology.* Mem. Geol. (Lausanne), 23:1013–1048.

Boon, J.J., and de Leeuw, J.W., 1979. The analysis of wax esters, very long mid-chain ketones and sterol ethers isolated from Walvis Bay diatomaceous ooze. *Mar. Chem.,* 7:117–132.

Bown, P.R., Rutledge, D.C., Crux, J.A., and Gallagher, L.T., 1998. *In* Bown, P.R. (Ed.), *Calcareous Nannofossil Biostratigraphy:* London (Chapman and Hall), 86–131.

Bralower, T.J., Arthur, M.A., Leckie, R.M., Sliter, W.V., Allard, D.J., and Schlanger, S.O., 1994. Timing and paleoceanography of oceanic dysoxia/anoxia in the late Barremian to early Aptian. *Palaios,* 9:335–369.

Bralower, T.J., CoBabe, E., Clement, B., Sliter, W.V., Osburne, C., and Longoria, J., 1999. The record of global change in mid-Cretaceous (Barremian–Albian) sections from the Sierra Madre, northeastern Mexico. *In* Huber, B.T., Bralower, T.J., and Leckie, R.M. (Eds.), *J. Foraminiferal Res.,* 29:418–437.

Bralower, T.J., Monechi, S., and Thierstein, H.R., 1989. Calcareous nannofossil zonation of the Jurassic-Cretaceous boundary interval and correlation with the geomagnetic polarity timescale. *Mar. Micropaleontol.,* 14:153–235.

Brassell, S.C., 1984. Aliphatic hydrocarbons of a Cretaceous black shale and its adjacent green claystone from the southern Angola Basin. Deep Sea Drilling Project, Leg 75. *In* Hay, W.W., Sibuet, J.C., et al., *Init. Repts. DSDP,* 75 (Pt. 2): Washington (U.S. Govt. Printing Office), 1019–1030.

————, 1993. Applications of biomarkers for delineating marine paleoclimatic fluctuations during the Pleistocene. *In* Engel, M.H., and Macko, S.A. (Eds.), *Organic Geochemistry: Principles and Applications:* New York (Plenum), 699–738.

Brassell, S.C., Comet, P.A., Eglinton, G., Isaacson, P.J., McEvoy, J., Maxwell, J.R., Thomson, I.D., Tibbetts, P.J., and Volkman, J.K., 1980. The origin and fate of lipids in the Japan Trench. *In* Douglas, A.G., and Maxwell, J.R. (Eds.), *Advances in Organic Geochemistry 1979:* Oxford (Pergamon Press), 375–392.

Brassell, S.C., and Eglinton, G., 1983. Steroids and triterpenoids in deep-sea sediments as environmental and diagenetic indicators. *In* Bjorøy, M., et al. (Eds.), *Advances in Organic Geochemistry 1981:* Chichester (Wiley), 684–697.

Brassell, S.C., and Eglinton, G., 1986. Molecular geochemical indicators in sediments. *In* Sohn, M. (Ed.), *Organic Marine Geochemistry,* Washington, *Amer. Chem. Soc. Symp. Ser.,* 305:10–32.

Brassell, S.C., Eglinton, G., and Howell, V.J., 1987. Palaeoenvironmental assessment for marine organic-rich sediments using molecular organic geochemistry. *In* Brooks, J., and Fleet, A.J. (Eds.), *Marine Petroleum Source Rocks.* Spec. Publ.—Geol. Soc. London, 26:79–98.

Brassell, S.C., Eglinton, G., Marlowe, I.T., Pflaumann, U., and Sarnthein, M., 1986. Molecular stratigraphy: a new tool for climatic assessment. *Nature,* 320:129–133.

Brassell, S.C., Eglinton, G., and Maxwell, J.R., 1983. The geochemistry of terpenoids and steroids. *Biochem. Soc. Trans.,* 11:575–586.

Brassell, S.C., Eglinton, G., Maxwell, J.R., and Philp, R.P., 1978. Natural background of alkanes in the aquatic environment. *In* Hutzinger, O., van Lelyveld, L.H., and Zoeteman, B.C.J. (Eds.), *Aquatic Pollutants: Transformation and Biological Effects:* Oxford (Pergamon Press), 69–86.

Brassell, S.C., McEvoy, J., Hoffmann, C.F., Lamb, N.A., Peakman, T.M., and Maxwell, J.R., 1984. Isomerization, rearrangement and aromatisation of steroids in distinguishing early stages of diagenesis. *In* Schenck, P.A., de Leeuw, J.W., and Lijmbach, G.W.M. (Eds.), *Advances in Organic Geochemistry 1983:* Oxford (Pergamon Press), 6:11–23.

Brassell, S.C., Wardroper, A.M.K., Thomson, I.D., Maxwell, J.R., and Eglinton, G., 1981. Specific acyclic isoprenoids as biological markers of methanogenic bacteria in marine sediments. *Nature,* 290:693–696.

Bréhéret, J.G., 1988. Episodes de sédimentation riches en matière organique dans les marnes bleues d'âge Aptien et Albien de la partie pélagique du bassin vocontien. *Bull. Geol. Soc. Fr.,* 8:349–356.

Busson, G., and Noël, D., 1991. Les Nannoconides, indicateurs environnementaux des oceans et mers epicontinentales du Jurassique terminal et du Cretace inferieur. *Oceanol. Acta,* 14:333–356.

Comet, P.A., McEvoy, J., Brassell, S.C., Eglinton, G., Maxwell, J.R., and Thomson, I.D., 1981. Lipids of an upper Albian limestone, Deep Sea Drilling Project Site 465, Section 465A-38-3. *In* Thiede, J., Vallier, T.L., et al., *Init. Repts. DSDP,* 62: Washington (U.S. Govt. Printing Office), 923–937.

Cox, A., and Gordon, R.G., 1984. Paleolatitudes determined from paleomagnetic data from vertical cores. *Rev. Geophys. Space Phys.,* 22:47–72.

Dachs, J., Bayona, J.M., Fowler, S.W., Miquel, J.C., and Albaiges, J., 1998. Evidence for cyanobacterial inputs and heterotrophic alteration of lipids in sinking particles in the Alboran Sea (SW Mediterranean). *Mar. Chem.,* 60:189–201.

Dastillung, M., Albrecht, P., and Ourisson, G., 1980. Aliphatic and polycyclic ketones in sediments. C_{27}–C_{35} ketones and aldehydes of the hopane series. *J. Chem. Res.,* (M)2325–2352; (S)166–167.

Didyk, B.M., Simoneit, B.R.T., Brassell, S.C., and Eglinton, G., 1978. Organic geochemical indicators of palaeoenvironmental conditions of sedimentation. *Nature,* 272:216–222.

Edmunds, K.L.H., Brassell, S.C., and Eglinton, G., 1980. The short-term diagenetic fate of 5α-cholestan-3β-ol: in situ radiolabelled incubations in algal mats. *In* Douglas, A.G., and Maxwell, J.R. (Eds.), *Advances in Organic Geochemistry 1979:* Oxford (Pergamon Press), 427–434.

Eglinton, G., and Hamilton, R.J., 1963. The distribution of alkanes. *In* Swain, T. (Ed.), *Chemical Plant Taxonomy:* London (Academic Press), 187–208.

Erba, E., 1994. Nannofossils and superplumes: the early Aptian "nannoconids crisis." *Paleoceanography,* 9:483–501.

Erba, E., Channell, J.E.T., Claps, M., Jones, C., Larson, R., Opdyke, B., Premoli Silva, I., Riva, A., Salvini, G., and Torricelli, S., 1999. Integrated stratigraphy of the Cismon APTICORE (southern Alps, Italy): a "reference section" for the Barremian–Aptian interval at low latitudes. *J. Foraminiferal Res.,* 29:371–391.

Erbacher, J., 1994. Entwicklung und Paläoozeanographie mittelkretazischer Radiolarien der westlichen Tethys (Italien) und des Nordatlantiks. *Tubing. Mikropalaontol. Mitteil.,* 12:1–120.

Erbacher, J., and Thurow, J., 1997. Influence of oceanic anoxic events on the evolution of mid-Cretaceous radiolaria in the North Atlantic and western Tethys. *Mar. Micropaleontol.,* 30:139–158.

Farrimond, P., Eglinton, G., and Brassell, S.C., 1986a. Alkenones in Cretaceous black shales, Blake-Bahama Basin, western North Atlantic. *In* Leythaeuser, D., and Rullkötter, J. (Eds.), *Advances in Organic Geochemistry, 1985*. Org. Geochem., 10:897–903.

————, 1986b. Geolipids of black shales and claystones in Cretaceous and Jurassic sediment sequences from the North American Basin. *In* Summerhayes, C.P., and Shackleton, N.J. (Eds.), *North Atlantic Palaeoceanography.* Spec. Publ.—Geol. Soc. London, 21:347–360.

Farrimond, P., Eglinton, G., Brassell, S.C., and Jenkyns, H.C., 1990. The Cenomanian/Turonian anoxic event in Europe: an organic geochemical study. *Mar. Pet. Geol.,* 7:75–89.

Ferdelman, T.G., Lee, C., Pantoja, S., Harder, J., Bebout, B.M., and Fossing, H., 1997. Sulfate reduction and methanogenesis in a *Thioploca*-dominated sediment off the coast of Chile. *Geochim. Cosmochim. Acta,* 61:3065–3079.

Fischer, A.G., Heezen, B.C., et al., 1971. *Init. Repts. DSDP,* 6: Washington (U.S. Govt. Printing Office).

Floyd, P.A., Winchester, J.A., and Castillo, P.R. 1992. Geochemistry and petrography of Cretaceous sills and lava flows, Sites 800 and 802. *In* Larson, R.L., Lancelot, Y., et al., *Proc. ODP, Sci. Results,* 129: College Station, TX (Ocean Drilling Program), 345–359.

Gagosian, R.B., and Peltzer, E.T., 1986. The importance of atmospheric input of terrestrial organic material to deep sea sediments. *In* Leythaeuser, D., and Rullkötter, J. (Eds.), *Advances in Organic Geochemistry 1985:* Oxford (Pergamon Press) *Org. Geochem.,* 10:897–903.

Gagosian, R.B., Peltzer, E.T., and Merrill, J.T., 1987. Long-range transport of terrestrially derived lipids in aerosols from the south Pacific. *Nature,* 325:800–803.

Gagosian, R.B., and Smith, S.O., 1979. Steroid ketones in surface sediments from the south-west African Shelf. *Nature,* 277:287–289.

Gagosian, R.B., Smith, S.O., and Nigrelli, G.E., 1982. Vertical transport of steroid alcohols and ketones measured in a sediment trap experiment in the equatorial Atlantic Ocean. *Geochim. Cosmochim. Acta,* 46:1163–1172.

Gagosian, R.B., Volkman, J.K., and Nigrelli, G.E., 1983. The use of sediment traps to determine sterol sources in coastal sediments off Peru. *In* Bjoroy, M. (Ed.), *Advances in Organic Geochemistry, 1981:* Chichester (Wiley), 369–379.

Gelpi, E., Schneider, H., Mann, J., and Oró, J., 1970. Hydrocarbons of geochemical significance in microscopic algae. *Phytochemistry,* 9:603–612.

Goossens, H., de Leeuw, J.W., Schenk, P.A., and Brassell, S.C., 1984. Tocopherols as likely precursors of pristane in ancient sediment and crude oils. *Nature,* 312:440–442.

Greiner, A.Ch., Spyckerelle, C., and Albrecht, P., 1976. Aromatic hydrocarbons from geological sources: I. New naturally occurring phenanthrene and chrysene derivatives. *Tetrahedron,* 32:257–260.

Greiner, A.Ch., Spyckerelle, C., Albrecht, P., and Ourisson, G., 1977. Aromatic hydrocarbons from geological sources: V. Mono and diaromatic hopane derivatives. *J. Chem. Res.,* (M):3829–3871; (S):334–335.

Han, J., McCarthy, E.D., Calvin, M., and Benn, M.H., 1968. Hydrocarbon constituents of the blue-green algae *Nostoc muscorum, Anacystis nidulans, Phormidium luridum* and *Chlorogloea fritischii. J. Chem. Soc. C,* 2785–2791.

Hoefs, M.J.L., Versteegh, G.J.M., Rijpstra, I.C., de Leeuw, J.W., and Sinninghe Damsté, J.S., 1998. Postdepositional oxic degradation of alkenones: implications for the measurement of paleo sea surface temperatures. *Paleoceanography,* 13:42–49.

Holbourn, A., Kuhnt, W., and Soeding, E., 2001. Atlantic paleobathymetry, paleoproductivity and paleocirculation in the late Albian: the benthic foraminiferal record. *Palaeogeogr., Palaeoclimatol., Palaeoecol.,* 170:171–196.

Howard, D.L., Simoneit, B.R.T., and Chapman, D.J., 1984. Triterpenoids from lipids of *Rhodomicrobium vannielli. Arch. Microbiol.,* 137:200–204.

Hussler, G., and Albrecht, P., 1983. C_{27}–C_{29} monoaromatic anthrasteroid hydrocarbons in Cretaceous black shales. *Nature,* 304:262–263.

Hussler, G., Chappe, B., Wehrung, P., and Albrecht, P., 1981. C_{27}–C_{29} ring A monoaromatic steroids in Cretaceous black shales. *Nature,* 294:556–558.

Kaiho, K., 1998. Phylogeny of deep-sea calcareous trochospiral benthic foraminifera: evolution and diversification. *Micropaleontology,* 44:291–311.

————, 1999. Evolution in the test size of deep-sea benthic foraminifera during the past 120 million years. *Mar. Micropaleontol.,* 37:53–65.

Köster, J., Volkman, J.K., Rullkötter, J., Scolz-Böttcher, B.M., Reithmeir, J., and Fisher, U., 1999. Mono-, di- and trimethyl-branched alkanes in cultures of the filamentous cyanobacterium *Calothrix scopulorum. Org. Geochem.,* 30:1367–1379.

Jenkyns, H.C., 1995. Carbon-isotope stratigraphy and paleoceanographic significance of the Lower Cretaceous shallow-water carbonates of Resolution Guyot, Mid-Pacific Mountains. *In* Winterer, E.L., Sager, W.W., Firth, J.V., and Sinton, J.M. (Eds.), *Proc. ODP, Sci. Results,* 143: College Station, TX (Ocean Drilling Program), 99–104.

Larson, R.L., Steiner, M.B., Erba, E., and Lancelot, Y., 1992. Paleolatitudes and tectonic reconstructions of the oldest portion of the Pacific plate: a comparative study. *In* Larson, R.L., Lancelot, Y., et al., *Proc. ODP, Sci. Results,* 129: College Station, TX (Ocean Drilling Program), 615–631.

Lini, A., Weissert, H., and Erba, E., 1992. The Valanginian carbon isotope event: a first episode of greenhouse climate conditions during the Cretaceous. *Terra Nova,* 4:374–384.

Mackenzie, A.S., Brassell, S.C., Eglinton, G., and Maxwell, J.R., 1982. Chemical fossils: the geological fate of steroids. *Science,* 217:491–504.

Marlowe, I.T., Brassell, S.C., Eglinton, G., and Green, J.C., 1990. Long-chain alkenones and alkyl alkenoates and the fossil coccolith record of marine sediments. *Chem. Geol.,* 88:349–375.

McCaffrey, M.A., Farrington, J.W., and Repeta, D.J., 1989. Geochemical implications of the lipid composition of *Thioploca* spp. from the Peru upwelling region, 15°S. *Org. Geochem.,* 14:61–68.

Menegatti, A.P., Weissert, H., Brown, R.S., Tyson, R.V., Farrimond, P., Strasser, A., and Caron, M., 1998. High resolution $\delta^{13}C$ stratigraphy through the early Aptian “Livello Selli” of the Alpine Tethys. *Paleoceanography,* 13:530–545.

Müller, P.J., Kirst, G., Ruhland, G., von Storch, I., and Rosell-Melé, A., 1998. Calibration of the alkenone paleotemperature index ($U^{k}_{37}{'}$) based on core-tops from the eastern South Atlantic and the global ocean (60°N–60°S). *Geochim. Cosmochim. Acta,* 62:1757–1772.

Nakanishi, M., Tamaki, K., and Kobayashi, K., 1989. Mesozoic magnetic anomaly lineations and seafloor spreading history of the northwestern Pacific. *J. Geophys. Res.,* 94:15437–15462.

Ourisson, G., Albrecht, P., and Rohmer, M., 1979. The hopanoids: paleochemistry and biochemistry of a group of natural products. *Pure Appl. Chem.,* 51:709–729.

Ourisson, G., Rohmer, M., and Poralla, K., 1987. Microbial lipids betrayed by their fossils. *Microbiol. Sci.,* 4:52–57.

Peakman, T.M., and Maxwell, J.R., 1988. Early diagenetic pathways of steroid alkenes. *Org. Geochem.,* 13:583–592.

Pflum, C.E., and Frerichs, W.E., 1976. *Gulf of Mexico Deep-water Foraminifers.* Spec. Publ.—Cushman Found. Foraminiferal Res., 14.

Prahl, F.G., de Lange, G.J., Lyle, M., and Sparrow, M.A., 1989. Post-depositional stability of long-chain alkenones under contrasting redox conditions. *Nature,* 341:434–437.

Prahl, F.G., Muehlhausen, L.A., and Zahnle, D.L., 1988. Further evaluation of long-chain alkenones as indicators of paleoceanographic conditions. *Geochim. Cosmochim. Acta,* 52:2303–2310.

Premoli Silva, I., Erba, E., Salvini, G., Locatelli, C., and Verga, D., 1999. Biotic changes in Cretaceous oceanic anoxic events of the Tethys. *J. Foraminiferal Res.,* 29:352–370.

Robinson, N., Eglinton, G., Brassell, S.C., and Cranwell, P.A., 1984. Dinoflagellate origin for sedimentary 4α-methylsteroids and 5α(H)-stanols. *Nature,* 308:439–441.

Rohmer, M., Bisseret, P., and Neunlist, S., 1992. The hopanoids, prokaryotic triterpenoids and precursors of ubiquitous molecular fossils. *In* Moldowan, J.M., Albrecht, P., and Philp, R.P., *Biological Markers in Sediments and Petroleum:* Englewood Cliffs, NJ (Prentice Hall), 1–17.

Rohmer, M., Bouvier-Nave, P., and Ourisson, G., 1984. Distribution of hopanoid triterpenes in prokaryotes. *J. Gen. Microbiol.,* 130:1137–1150.

Roth, P.H., 1973. Calcareous nannofossils—Leg 17, Deep Sea Drilling Project. *In* Winterer, E.L., Ewing, J.I., et al., *Init. Repts. DSDP,* 17: Washington (U.S. Govt. Printing Office), 695–795.

Roth, P.H., and Bowdler, J., 1981. Middle Cretaceous calcareous nannoplankton biogeography and oceanography of the Atlantic Ocean. *In* Warme, J.E., Douglas, R.G., and Winterer, E.L. (Eds.), *The Deep Sea Drilling Project: A Decade of Progress.* Spec. Publ.—Soc. Econ. Paleontol. Mineral., 32:517–546.

Roth, P.H., and Krumbach, K.R., 1986. Middle Cretaceous calcareous nannofossil biogeography and preservation in the Atlantic and Indian Oceans: implications for paleoceanography. *Mar. Micropaleontol.,* 10:235–266.

Rullkötter, J., Mukhopadhyay, P.K., and Welte, D.H., 1984. Geochemistry and petrography of organic matter in sediments from Hole 530A, Angola Basin, and Hole 532, Walvis Ridge, Deep Sea Drilling Project. *In* Hay, W.W., Sibuet, J.-C., et al., *Init. Repts. DSDP,* 75 (Pt. 2), Washington (U.S. Govt. Printing Office), 1069–1087.

————, 1987. Geochemistry and petrography of organic matter from Deep Sea Drilling Project Site 603, lower continental rise off Cape Hatteras. *In* van Hinte, J.E., Wise, S.W., Jr., et al., *Init. Repts. DSDP,* 93 (Pt. 2): Washington (U.S. Govt. Printing Office), 1163–1176.

Rullkötter, J., and Welte, D.H., 1983. Maturation of organic matter in areas of high heat flow: a study of sediments from DSDP Leg 63, offshore California, and Leg 64, Gulf of California. *In* Bjoroey, M., Albrecht, C., Cornford, C., de Groot, K., Eglinton, G., Galimov, E., Leythaeuser, D., Pelet, R., Rullkötter, J., and Speers, G. (Eds.), *Advances in Organic Geochemistry 1981:* Chichester (Wiley), 438–448.

Sager, W.W., Kim, J., Klaus, A., Nakanishi, M., and Khankishieva, L.M., 1999. Bathymetry of Shatsky Rise, northwest Pacific Ocean: implications for ocean plateau development at a triple junction. *J. Geophys. Res.,* 104:7557–7576.

Schaaf, A., 1981. Late Early Cretaceous radiolarians from Deep Sea Drilling Project Leg 62. *In* Thiede, J., Vallier, T.L., et al., *Init. Repts. DSDP,* 62: Washington (U.S. Govt. Printing Office), 419–470.

Schlanger, S.O., and Moberly, R., 1986. Sedimentary and volcanic history: East Mariana Basin and Nauru Basin. *In* Moberly, R., Schlanger, S.O., et al., *Init. Repts. DSDP,* 89: Washington (U.S. Govt. Printing Office), 653–678.

Sheia, J., Brassell, S.C., and Ward, D.M., 1990. Mid-chain branched mono- and dimethyl alkanes in hot spring cyanobacterial mats: a direct biogenic source for branched alkanes in ancient sediments? *Org. Geochem.,* 15:223–231.

Simoneit, B.R., 1973. Identification of isoprenoidal ketones in Deep Sea Drilling Project core samples and their geochemical significance. *In* Burns, R.E., Andrews, J.E., et al., (Eds.) *Init. Repts. DSDP,* 21: Washington (U.S. Govt. Printing Office), 909–923.

Simoneit, B.R.T., 1978. The organic chemistry of marine sediments. *In* Riley, J.P., and Chester, R. (Eds.), *Chemical Oceanography* (2nd ed.) (Vol. 7): New York (Academic Press), 233–311.

————, 1986. Biomarker geochemistry of black shales from Cretaceous oceans—an overview. *Mar. Geol.,* 70:9–41.

Sliter, W.V., 1977. Cretaceous benthic foraminifers from the western South Atlantic Leg 39, Deep Sea Drilling Project. *In* Supko, P.R., Perch-Nielsen, K., et al., *Init. Repts. DSDP,* 39: Washington (U.S. Govt. Printing Office), 1657–687.

————, 1980. Mesozoic foraminifers and deep-sea benthic environments from Deep Sea Drilling Project Sites 415 and 416, eastern North Atlantic. *In* Lancelot, Y., Winterer, E.L., et al., *Init. Repts. DSDP,* 50: Washington (U.S. Govt. Printing Office), 353–427.

————, 1989. Aptian anoxia in the Pacific Basin. *Geology,* 17:909–912.

————, 1992. Cretaceous planktonic foraminiferal biostratigraphy and paleoceanographic events in the Pacific Ocean with emphasis on indurated sediment. *In* Ishizaki, K., and Saito, T. (Eds.), *Centenary of Japanese Micropaleontology:* Tokyo (Terra Sci.), 281–299.

Sliter, W.V., and Brown, G.R., 1993. Shatsky Rise: seismic stratigraphy and sedimentary record of Pacific paleoceanography since the Early Cretaceous. *In* Natland, J.H., Storms, M.A., et al., *Proc. ODP, Sci. Results,* 132: College Station, TX, (Ocean Drilling Program), 3–13.

Smith, D.J., Eglinton, G., and Morris, R.J., 1983. Aspects of steroid geochemistry of a interfacial sediment from the Peruvian upwelling. *Oceanol. Acta,* 6:211–219.

Summons, R.E., and Jahnke, J.L., 1990. Identification of the methylhopanes in sediments and petroleums. *Geochim. Cosmochim. Acta,* 54:247–251.

Summons, R.E., Volkman, J.K., and Boreham, C.J., 1987. Dinosterane and other steroidal hydrocarbons of dinoflagellate origin in sediments and petroleum. *Geochim. Cosmochim. Acta,* 51:3075–3082.

Thierstein, H.R., 1979. Paleoceanographic implications of organic carbon and carbonate distribution in Mesozoic deep sea sediments. *In* Talwani, M., Hay, W.W., and Ryan, W.B.F. (Eds.), *Deep Drilling Results in the Atlantic Ocean.* Maurice Ewing Ser., Am. Geophys. Union, 3:249–274.

Tissot, B., Durand, B., Espitalié, J., and Combaz, A., 1974. Influence of the nature and diagenesis of organic matter in the formation of petroleum. *AAPG Bull.,* 58:499–506.

van Morkhoven, F.P.C.M., Berggren, W.A., and Edwards, A.S., 1986. Cenozoic cosmopolitan deep-water benthic foraminifera. *Bull. Cent. Rech. Explor.—Prod. Elf-Aquitaine,* 11.

Volkman, J.K., and Maxwell, J.R., 1986. Acyclic isoprenoids as biological markers. *In* Johns, R.B. (Ed.), *Biological Markers in the Sedimentary Record:* New York (Elsevier), 1–42.

Weissert, H., and Lini, A., 1991. Ice age interludes during the time of Cretaceous greenhouse climate? *In* Müller, D.W., McKenzie, J.A., and Weissert, H. (Eds.), *Controversies in Modern Geology: Evolution of Geological Theories in Sedimentology, Earth History and Tectonics:* New York (Academic Press), 173–191.

Williams, L.A., and Reimers, C., 1983. Role of bacterial mats in oxygen-deficient marine basins and coastal upwelling regimes; preliminary report. *Geology,* 11:267–269.

Woodruff, F., 1985. Changes in Miocene deep-sea benthic foraminiferal distribution in the Pacific Ocean: relationship to paleoceanography. *In* Kennett, J.P. (Ed.), *The Miocene Ocean: Paleoceanography and Biogeography.* Mem.—Geol. Soc. Am., 163:131–175.

Zafiriou, O.C., Gagosian, R.B., Peltzer, E.T., Alford, J.B., and Loder, T., 1985. Air-to-sea fluxes of lipids at Enewetak Atoll. *J. Geophys. Res.,* 90:2409–2433.

Figure F1. Interpretation of seismic reflection profile across Site 1213 based on coring results. Mustard = Pliocene to Holocene, medium green = Albian through Aptian, dark green = Neocomian, brown = igneous sill unit (Unit IV) and basement. Lithologic units, subunits, and depths (in meters below seafloor [mbsf]) are indicated.

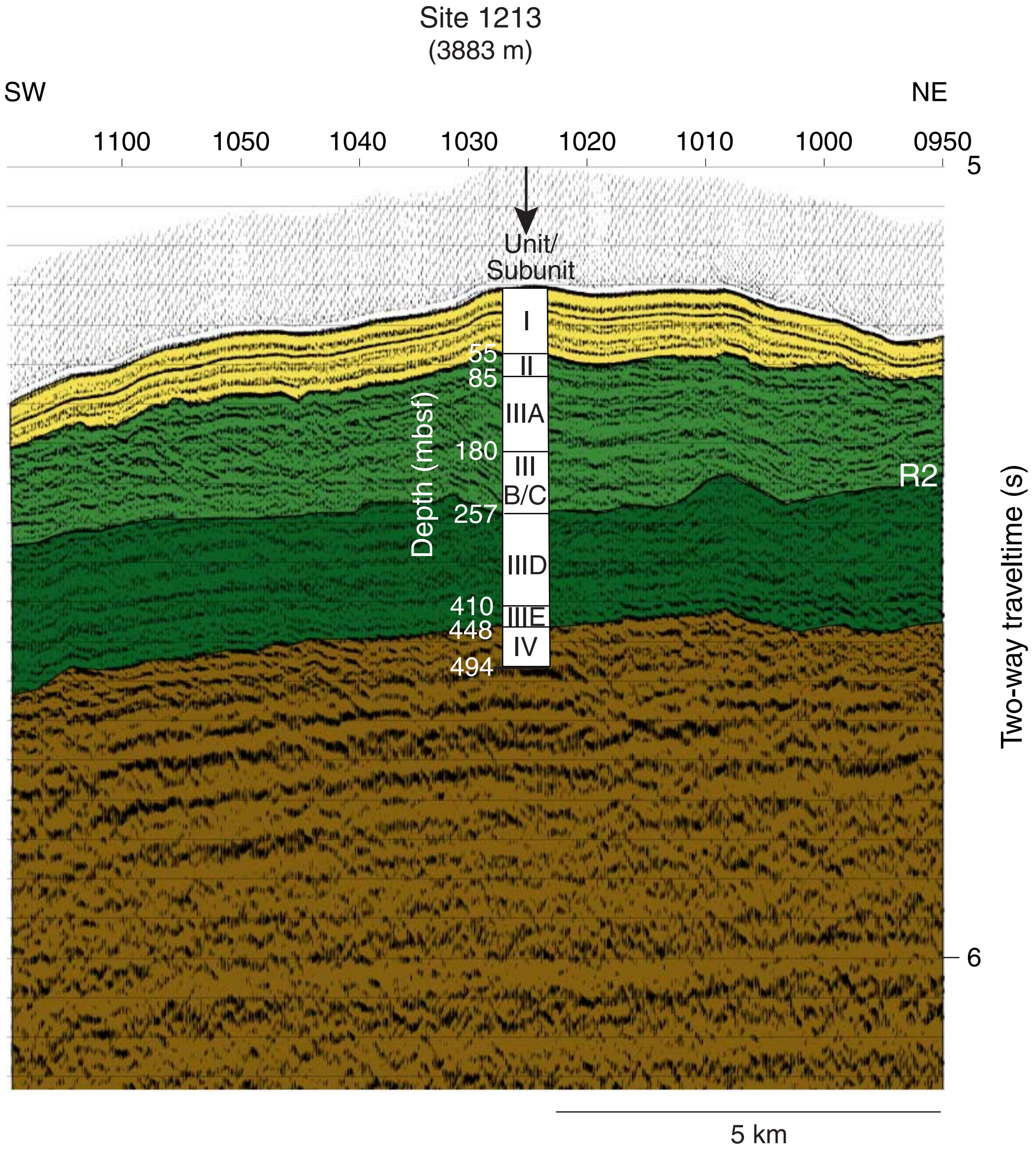

Figure F2. Core recovery, lithology, lithologic units, age with corresponding biostratigraphic zonations, color reflectance (at 550 nm), and percent carbonate for Site 1213. Foram. zn. = foraminiferal zone, nanno. zn. = nannofossil zone.

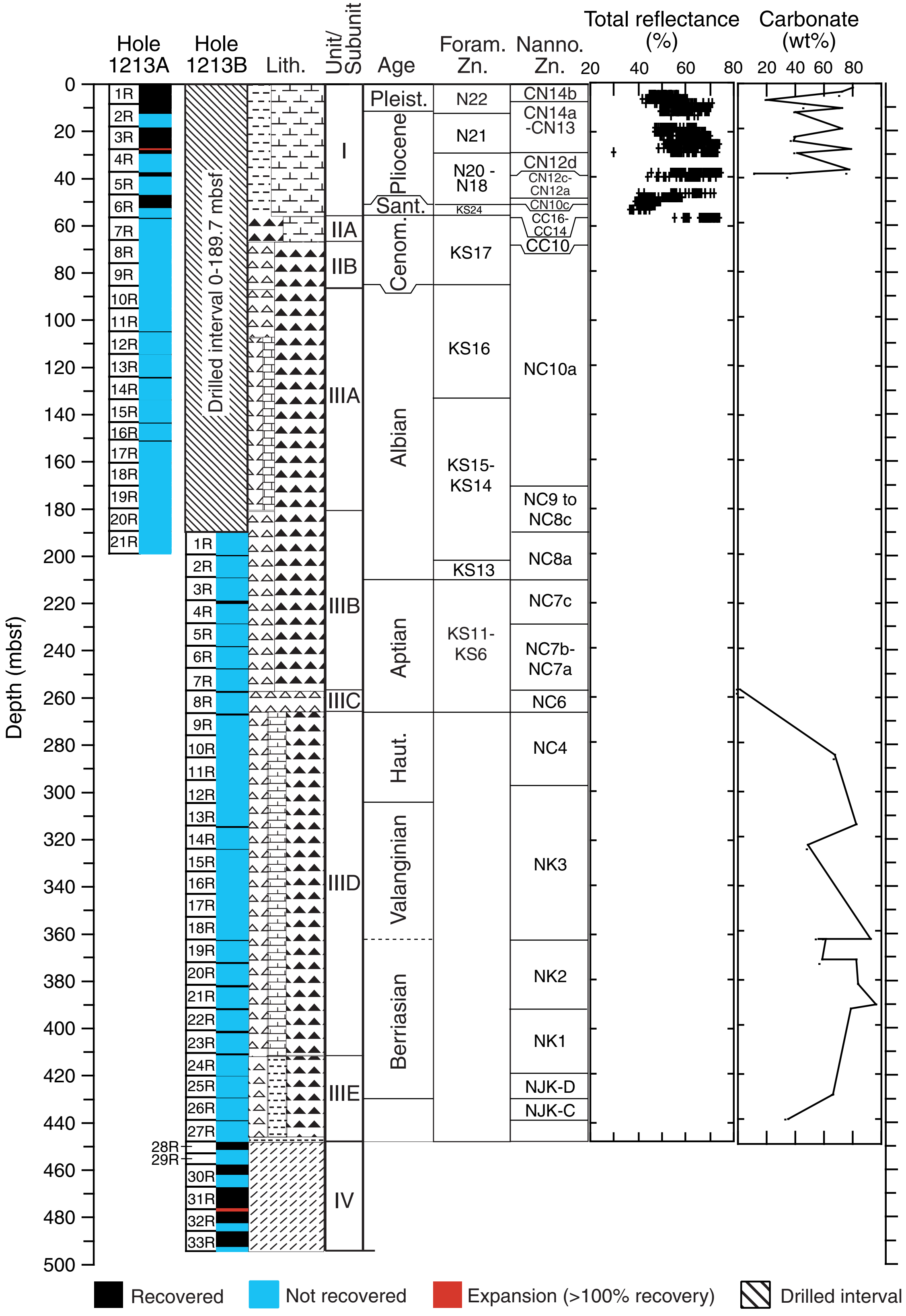

Figure F3. Composite digital photograph with total color reflectance (left panel) and bulk density (right panel) for Core 198-1213A-6R and Section 7R-1. The plot shows a sharp rise in total reflectance and bulk density at the boundary between the lower Pliocene and the Santonian at the Unit I/II contact.

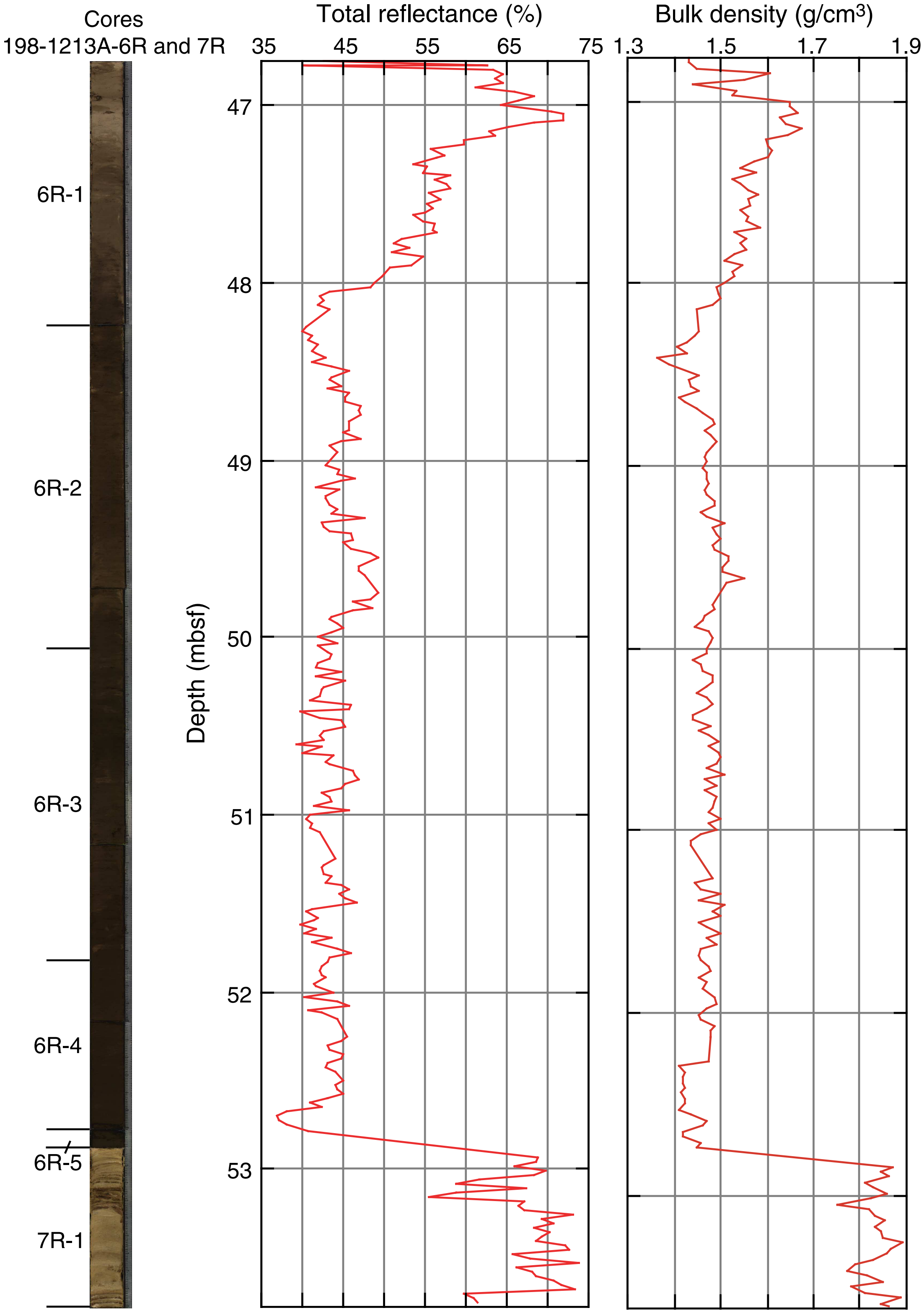

Figure F4. Digital photograph of Section 198-1213B-8R-1 showing the early Aptian OAE1a equivalent and associated sediment. Carbonate and C_{org} values are shown for selected samples.

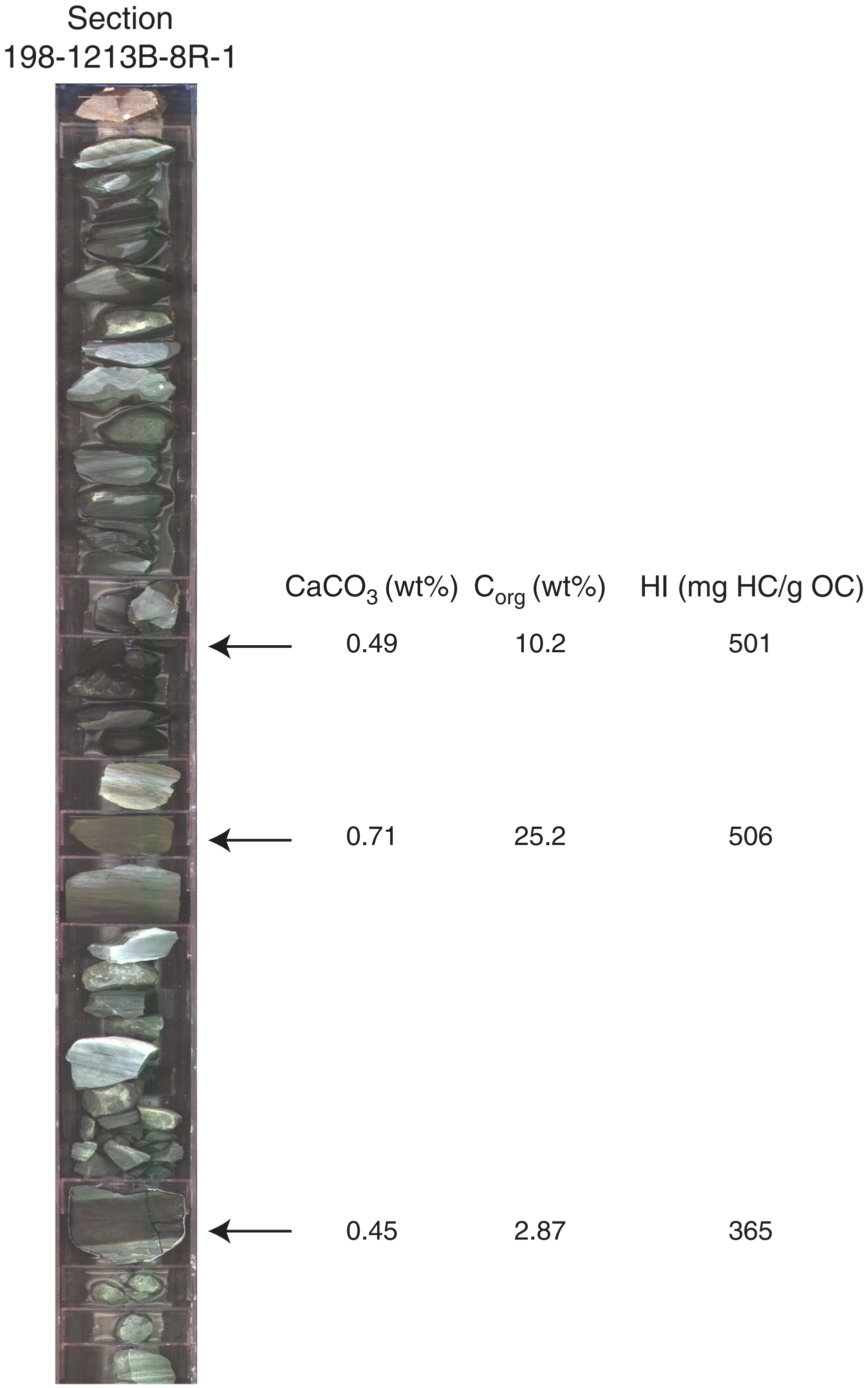

Figure F5. Close-up photograph showing pieces of early Aptian relatively C_{org}-rich radiolarian claystone of Subunit IIIC (interval 198-1213B-8R-1, 55–70 cm). The piece at 61–63 cm has 25.2 wt% C_{org}.

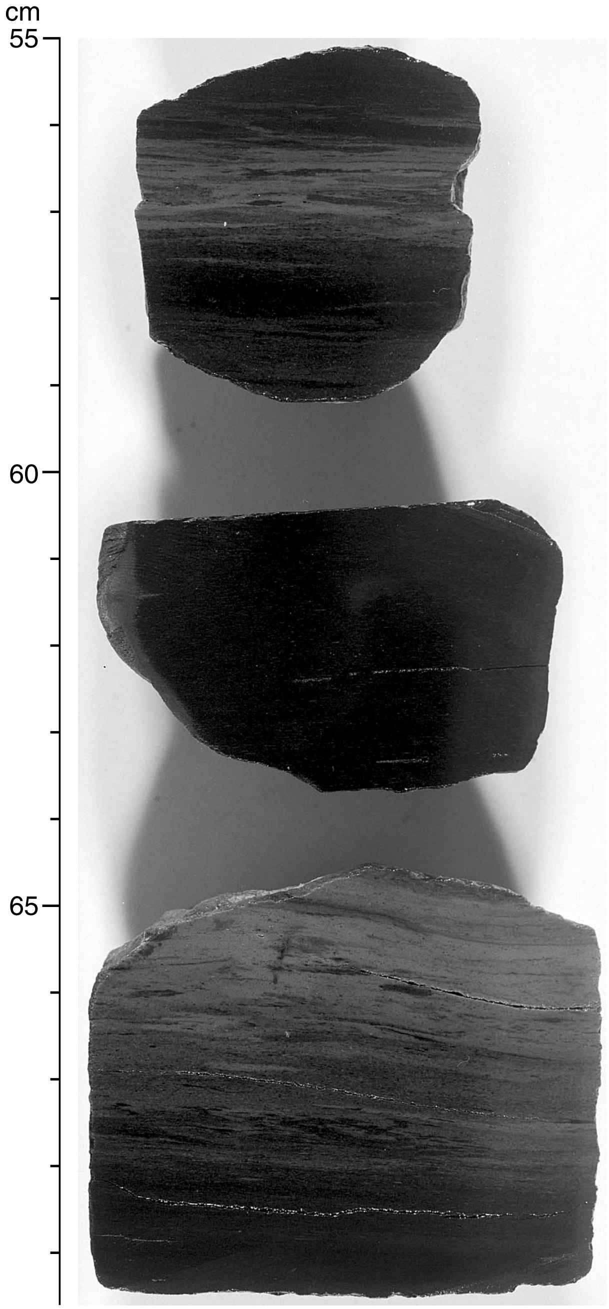

Figure F6. Close-up photograph showing a homogeneous, black radiolarian claystone of early Aptian age with sharp upper and lower contacts with dark greenish gray bioturbated radiolarian claystone (interval 198-1213B-8R-1, 92–99.5 cm). This black interval within Subunit IIIC contains 2.87 wt% C_{org}.

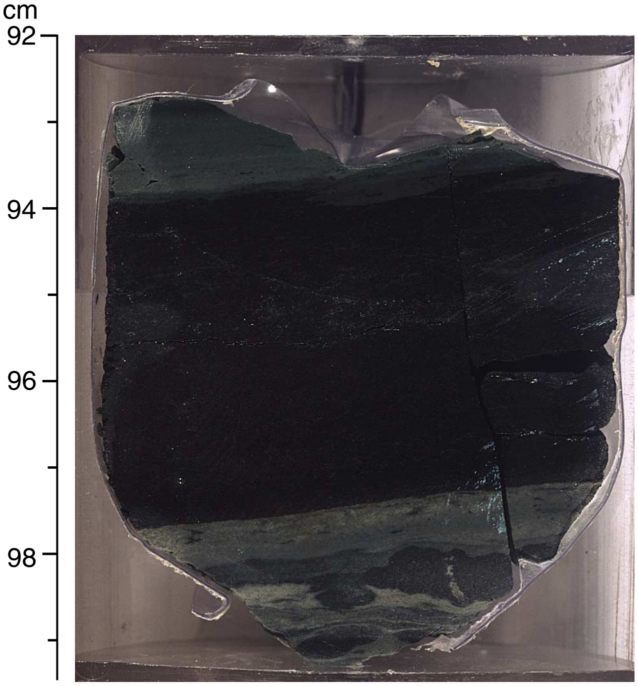

Figure F7. Close-up photograph showing bioturbated Berriasian chalk-nannofossil claystone cycle in Subunit IIID (interval 198-1213B-23R-1, 8–40 cm).

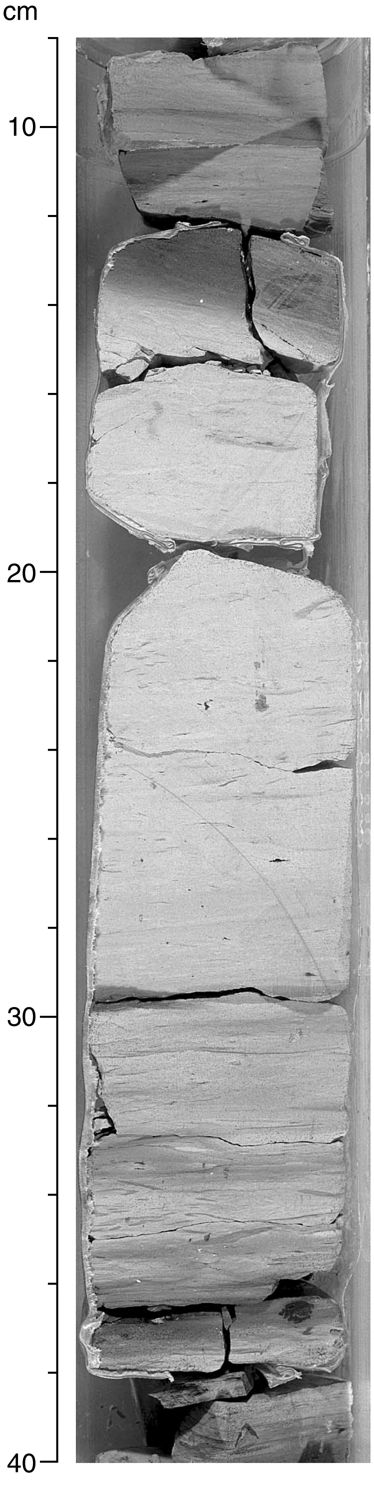

Figure F8. Close-up photograph illustrating the highly bioturbated fabric of Berriasian radiolarian chalks and clayey chalks of Subunit IIID (interval 198-1213B-22R-1, 62–79 cm). A horizontal composite burrow occurs at ~66 cm.

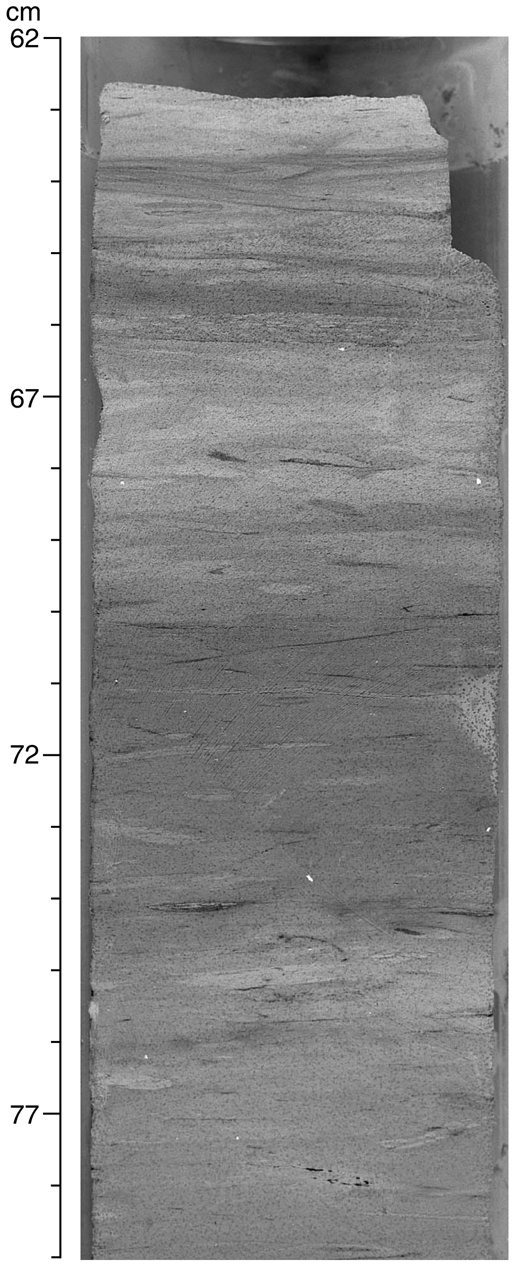

Figure F9. Close-up photograph of Sample 198-1213B-20R-1, 18–32 cm, showing soft-sediment deformation, probably a small slump, in clayey chalks of Subunit IIID.

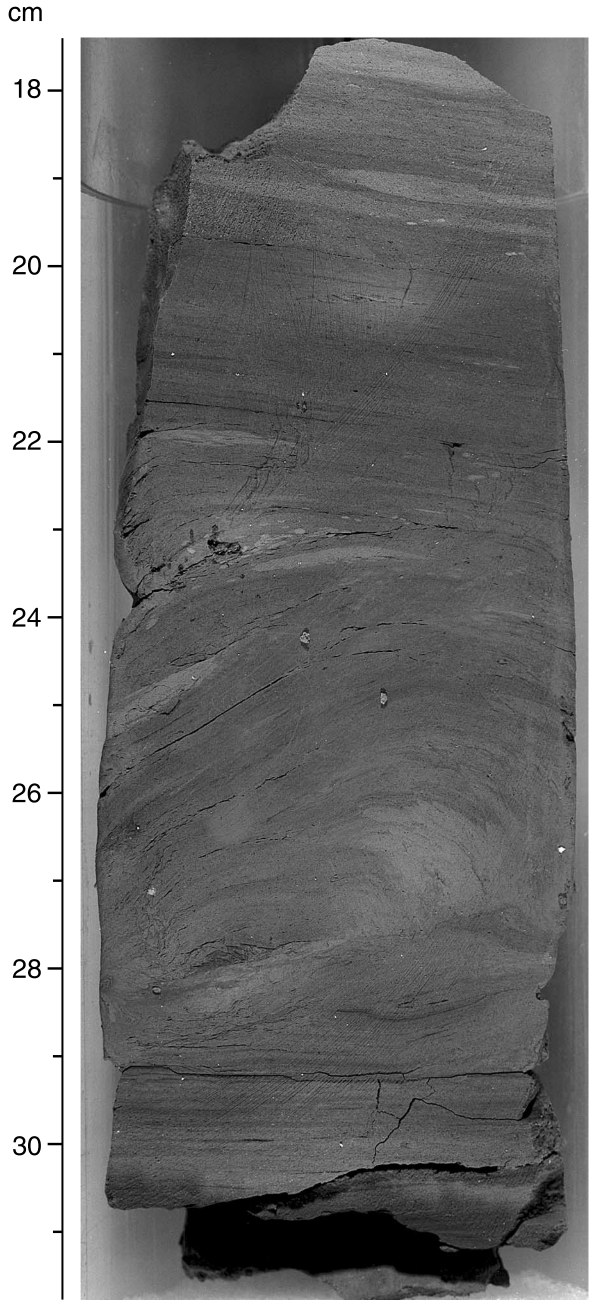

Figure F10. X-ray diffractogram for Sample 198-1213B-27R-1, 74–76 cm, a hydrothermal alteration breccia showing quartz and goethite to be the main mineral phases present.

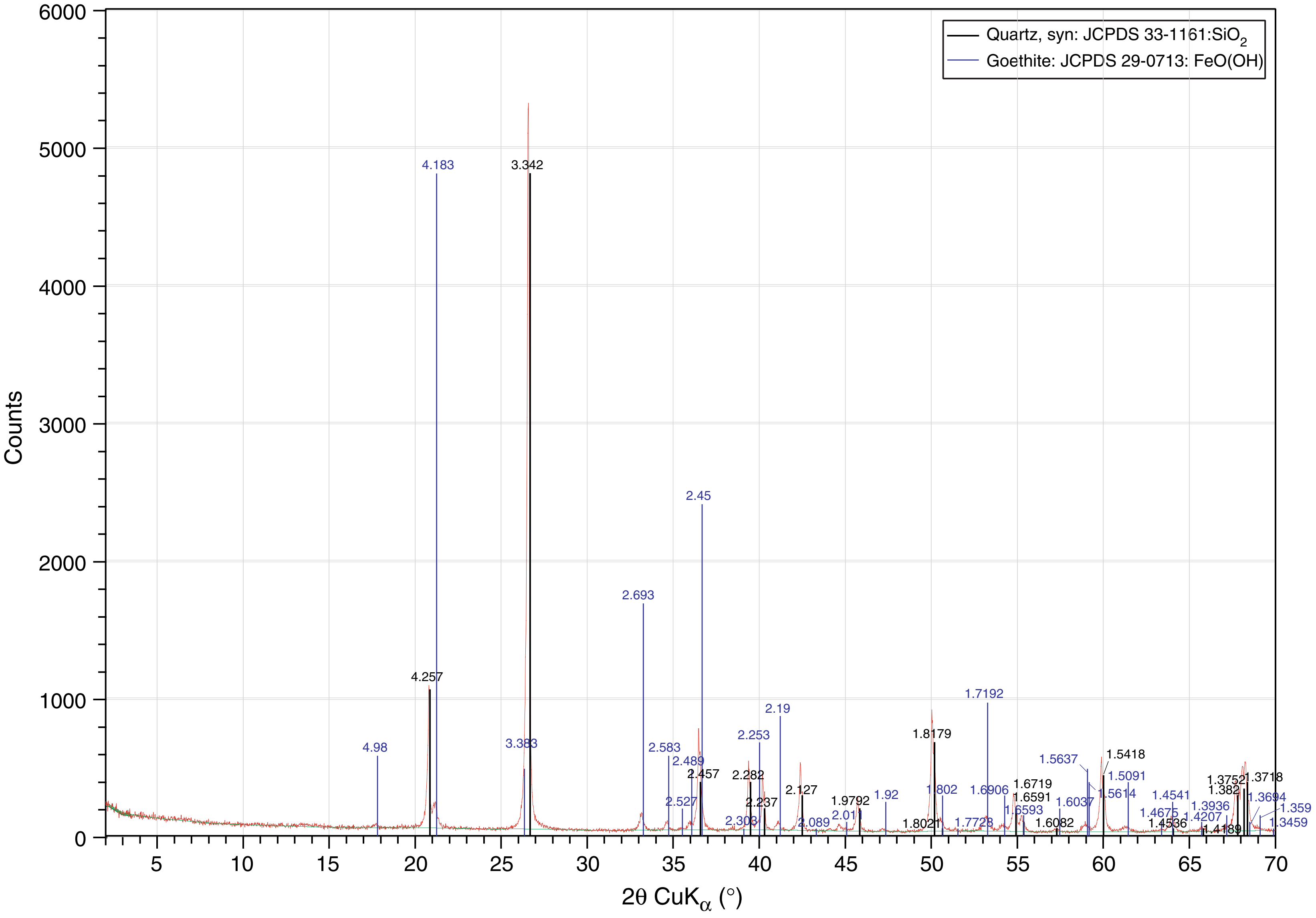

Figure F11. Photomicrographs of Sample 198-1213B-27R-1, 74–76 cm, showing possible microbial structures enclosed in quartz crystal cement within the breccia pictured in Figure F10, p. 49. The upper view is in plane-polarized light, and the lower view is with nicols crossed.

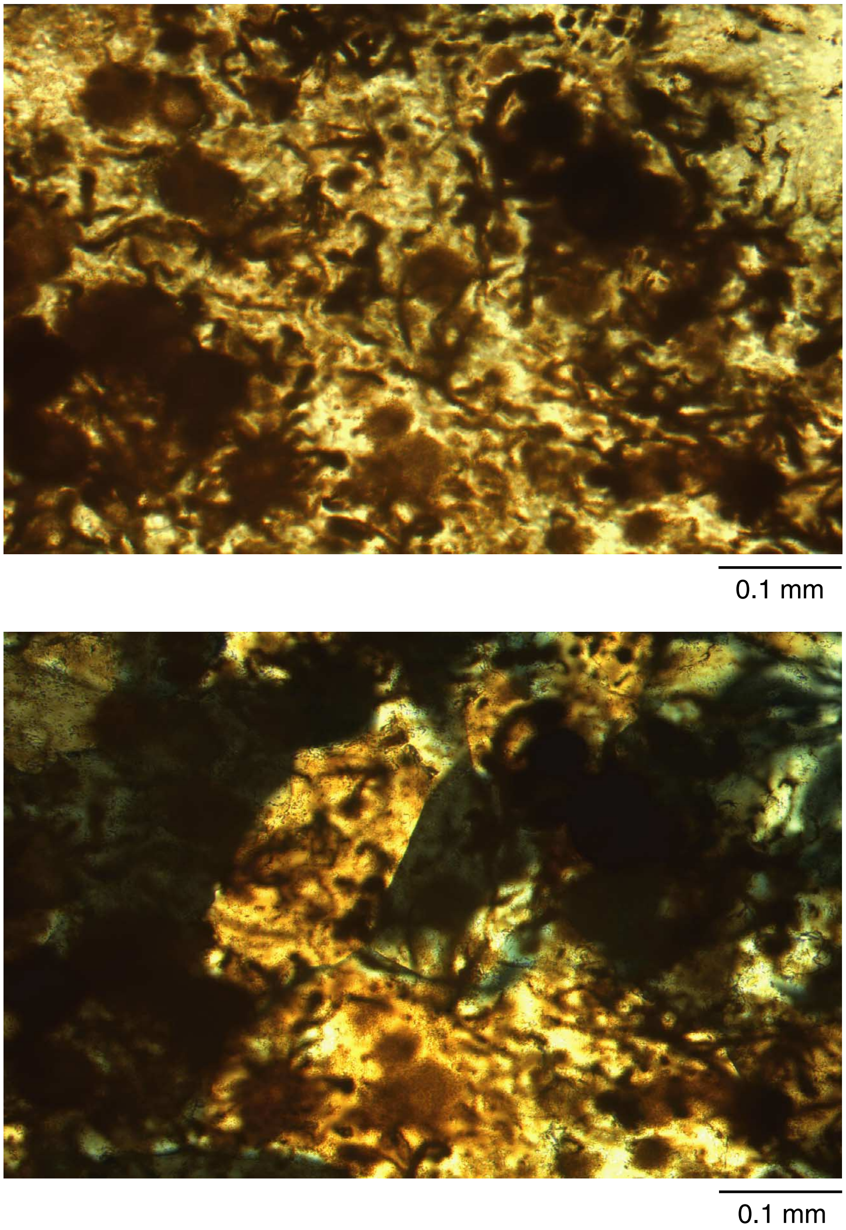

Figure F12. Composite digital photographs of Cores 198-1213B-28R through 33R showing diabase units and numbered core pieces. Note that the Subunit IVA, IVB, and IVC boundaries and possible chilled zones are identified. (Continued on next seven pages.)

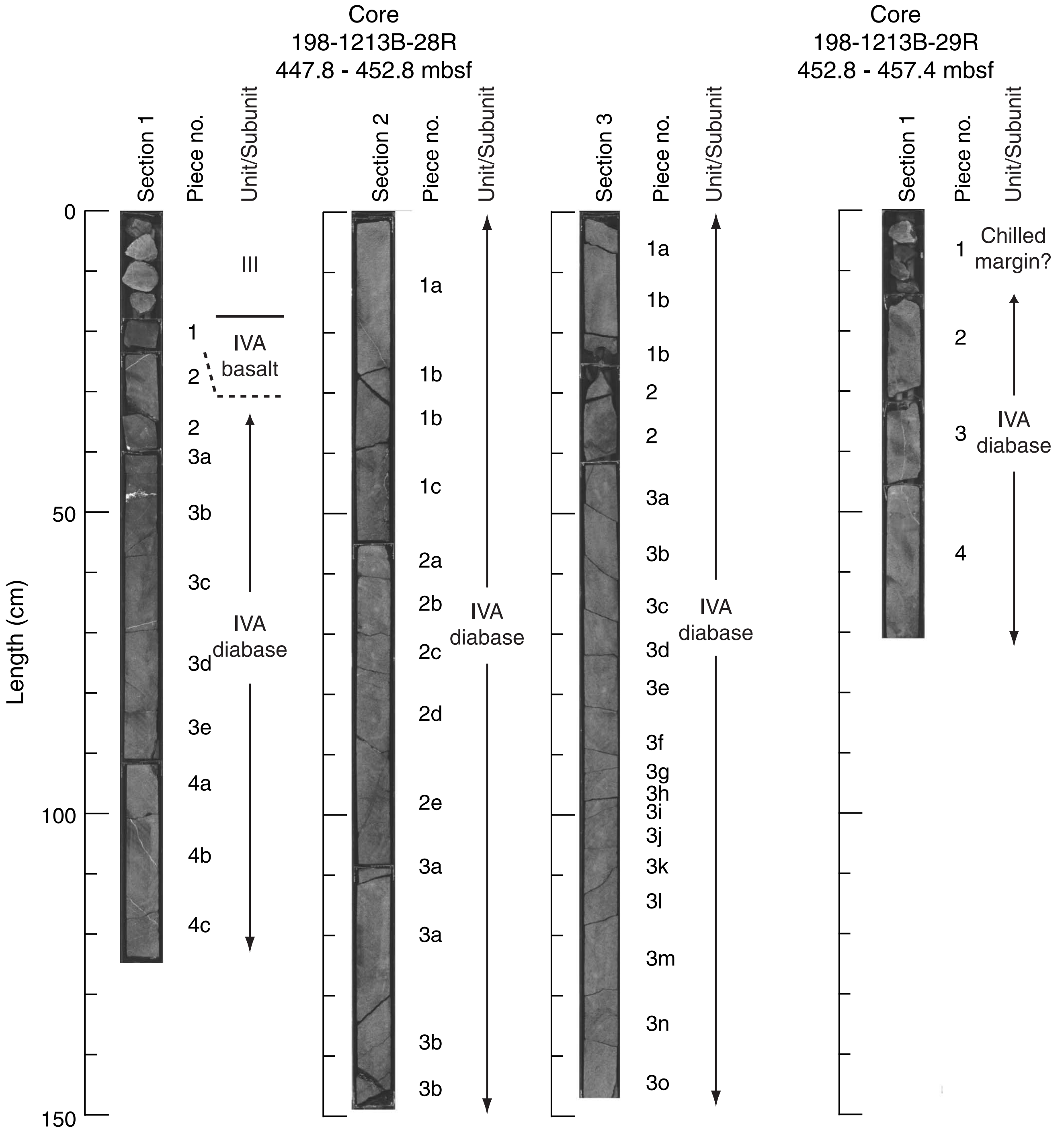

Figure F12 (continued).

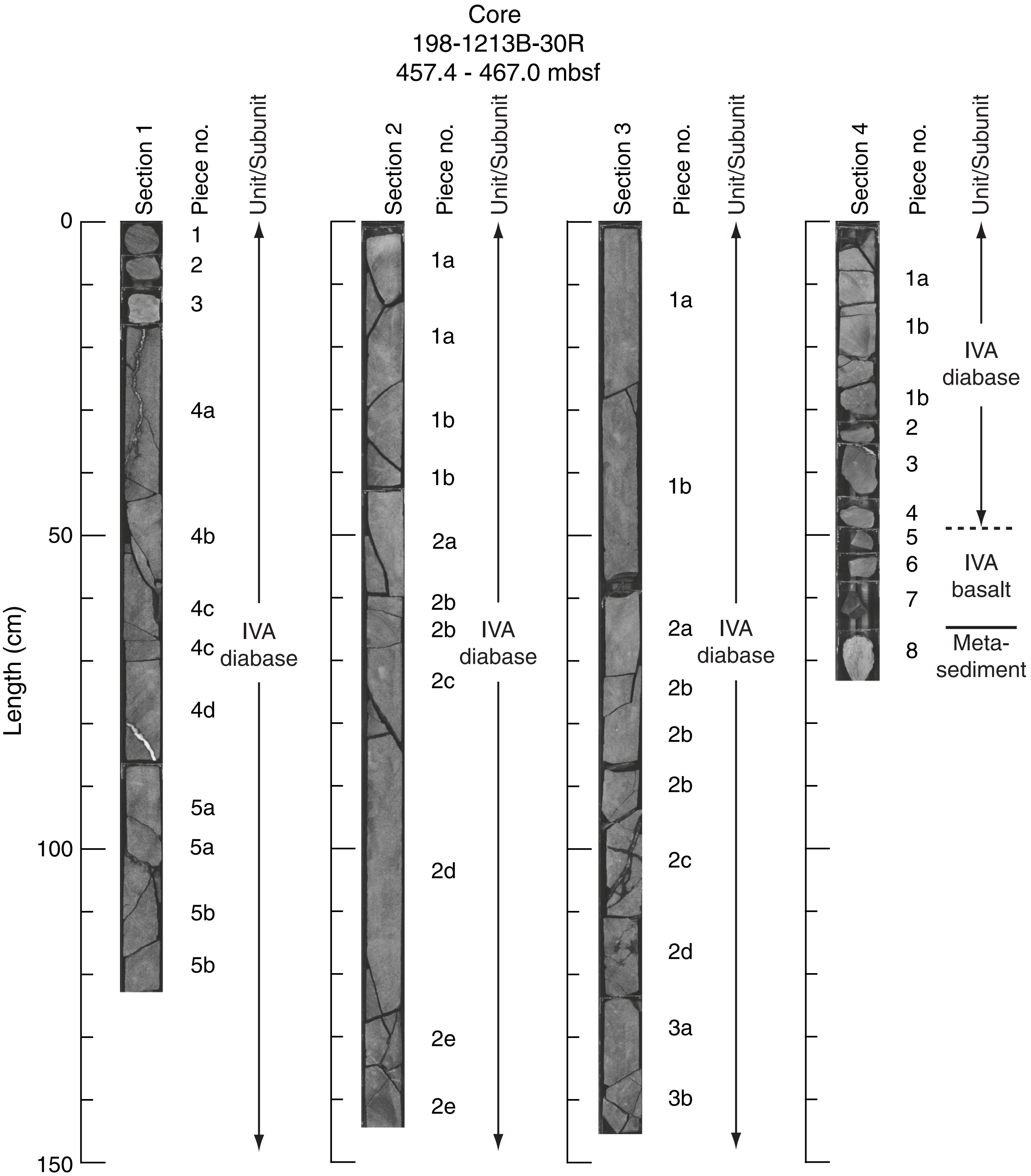

Figure F12 (continued).

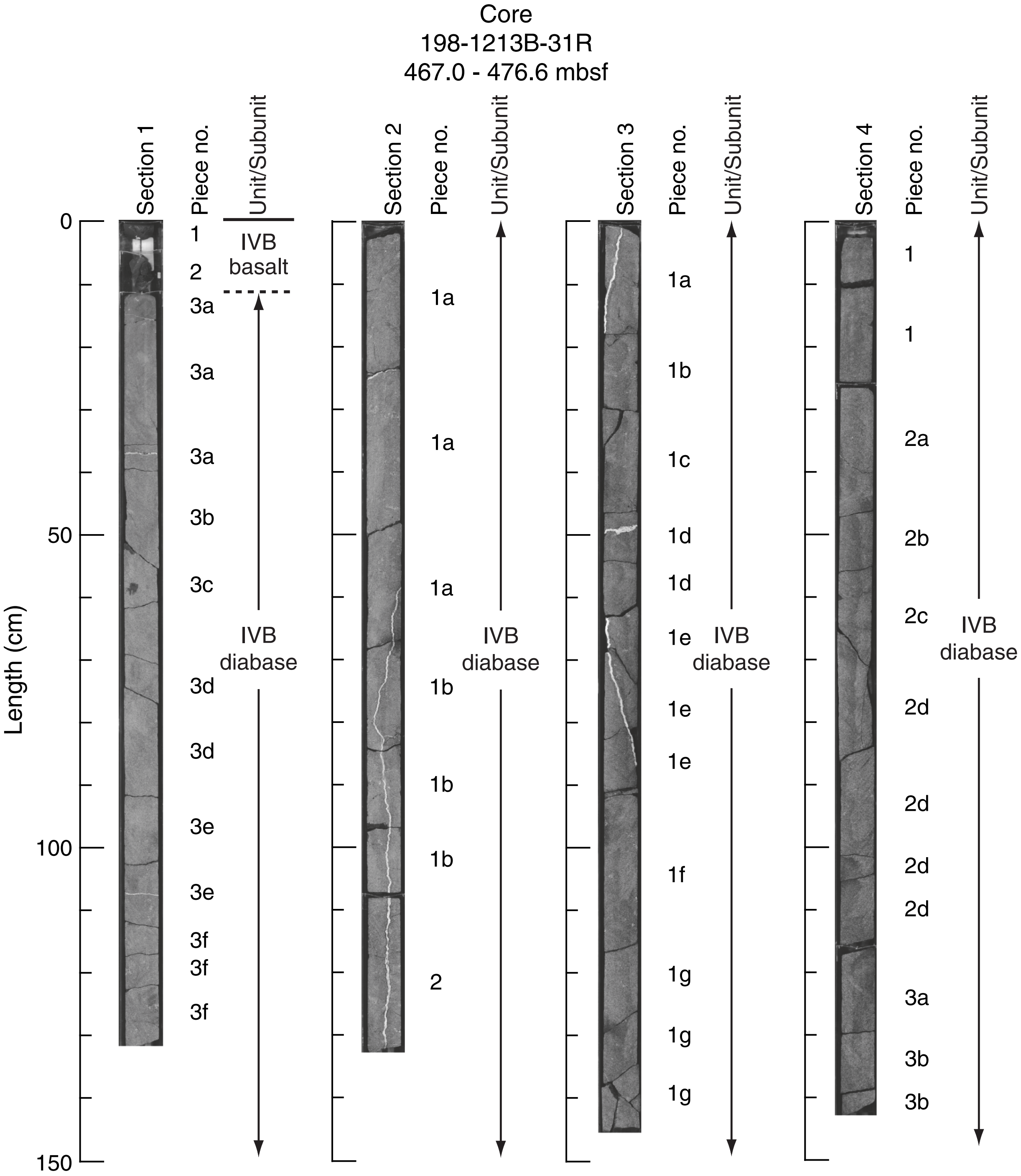

Figure F12 (continued).

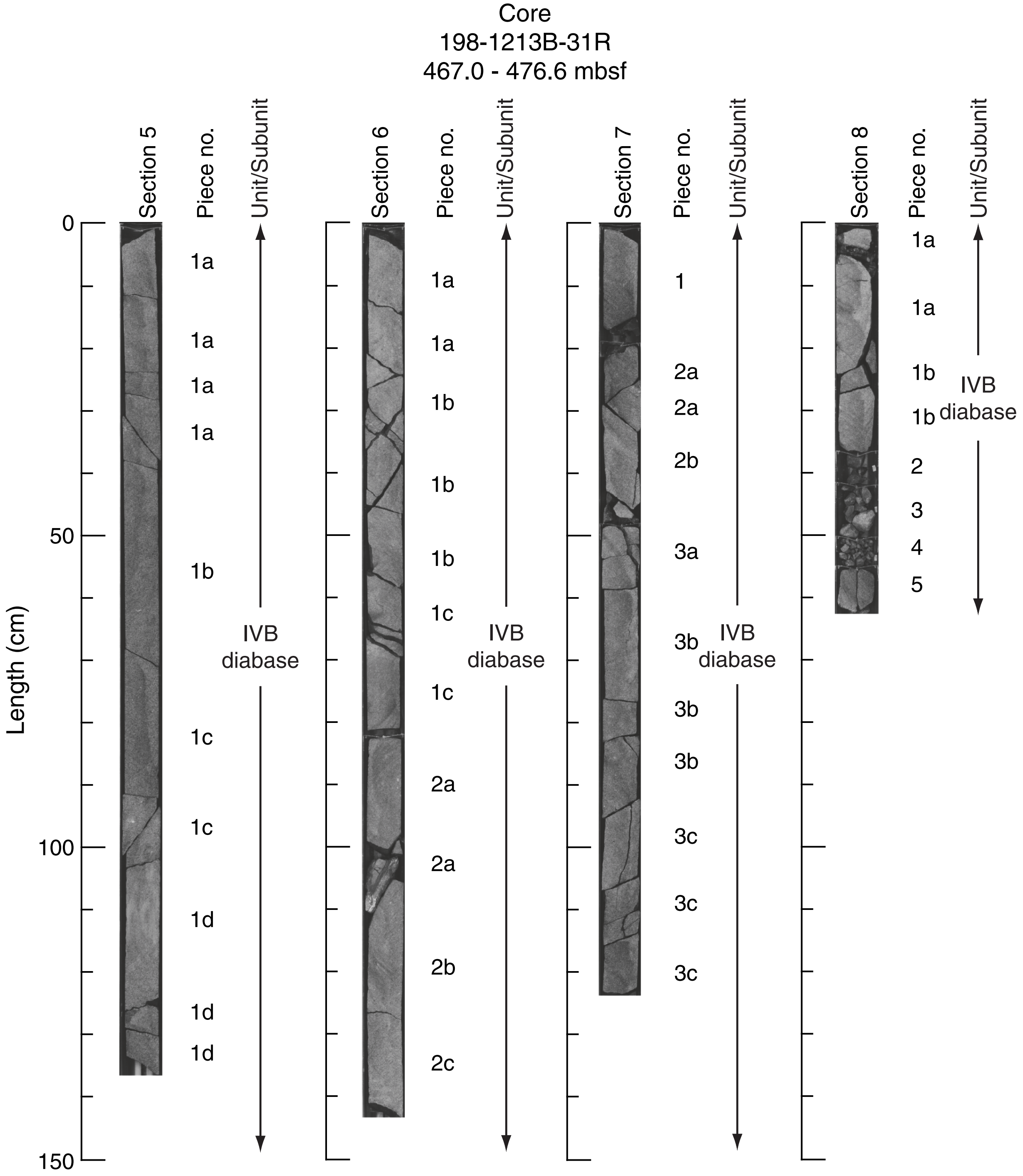

Figure F12 (continued).

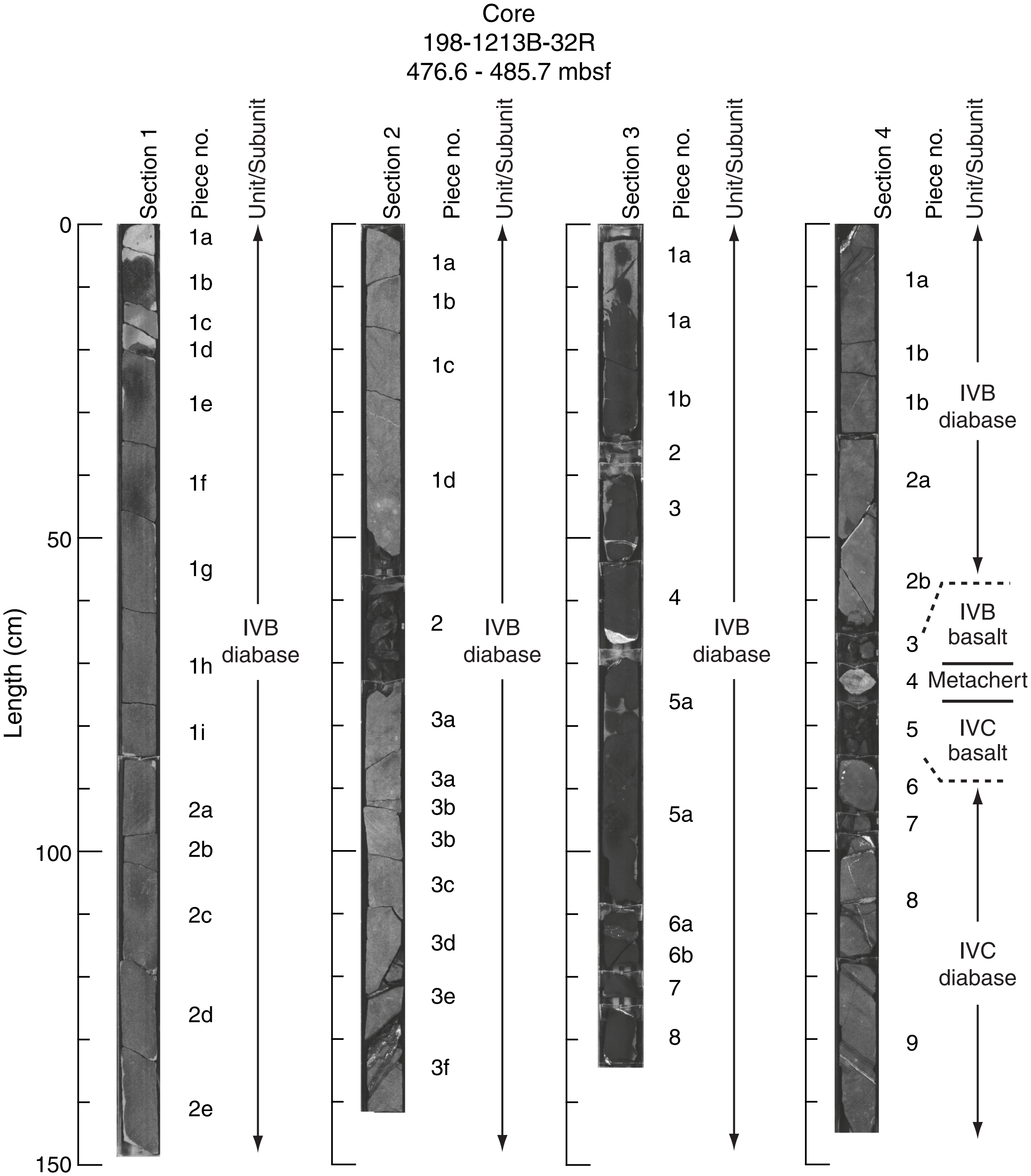

Figure F12 (continued).

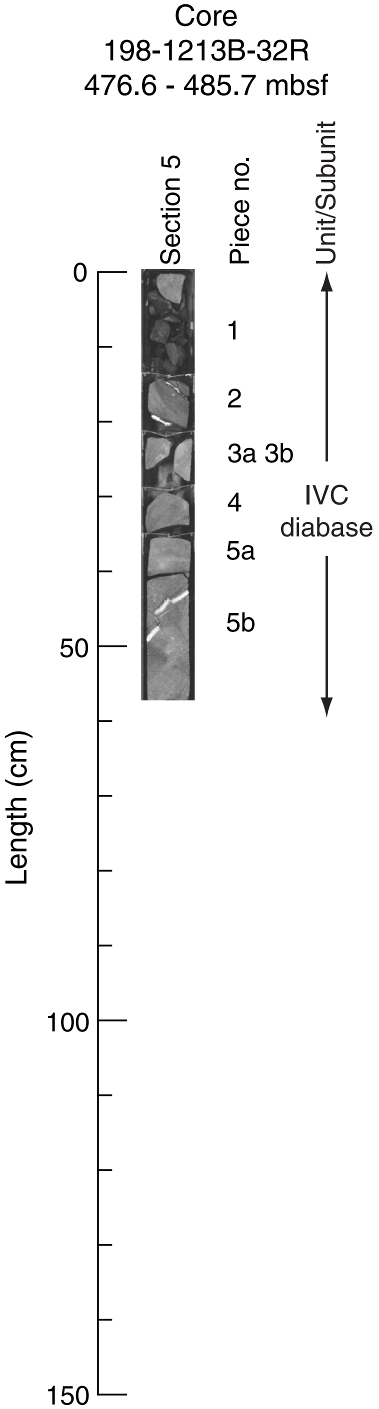

Figure F12 (continued).

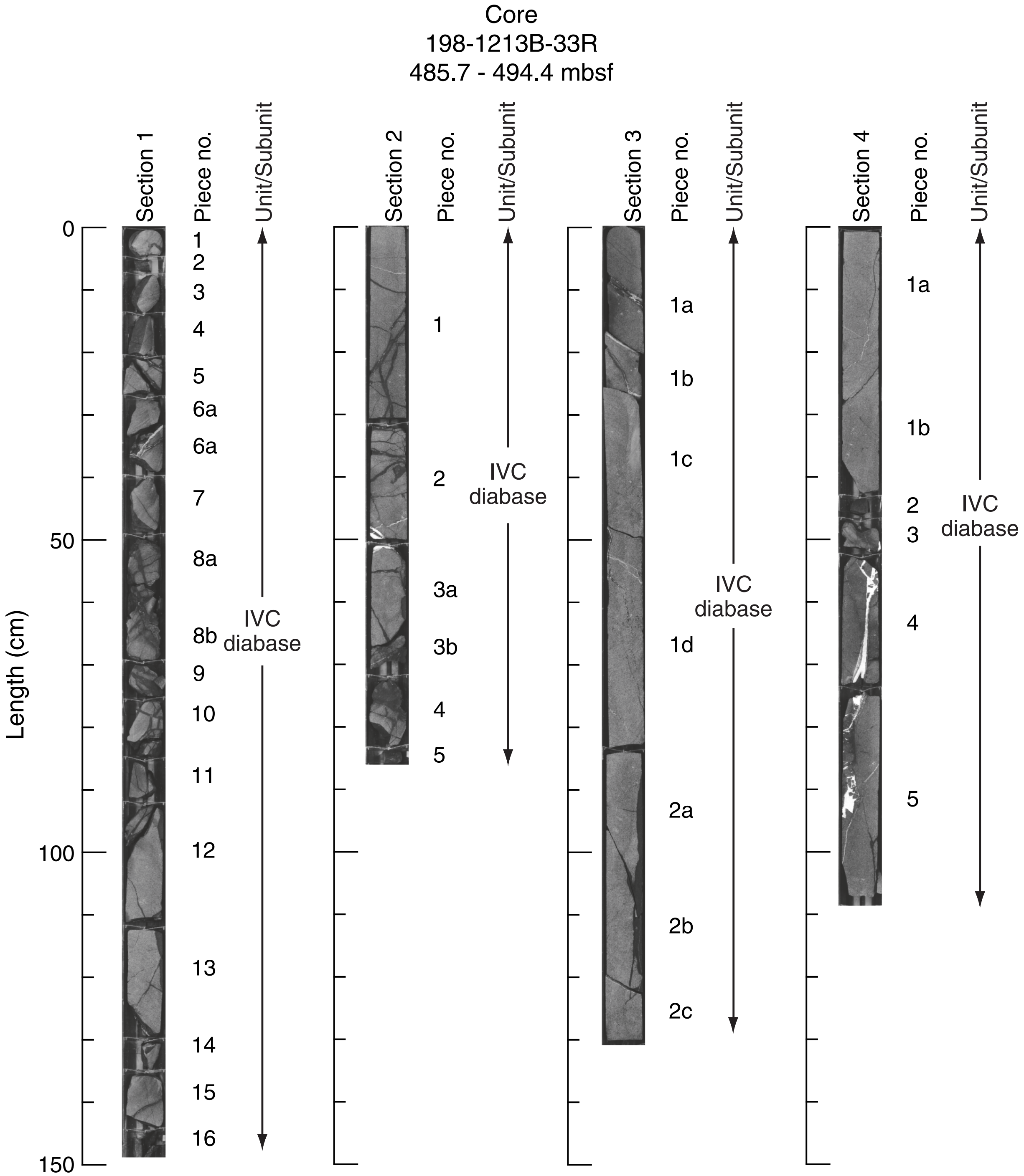

Figure F12 (continued).

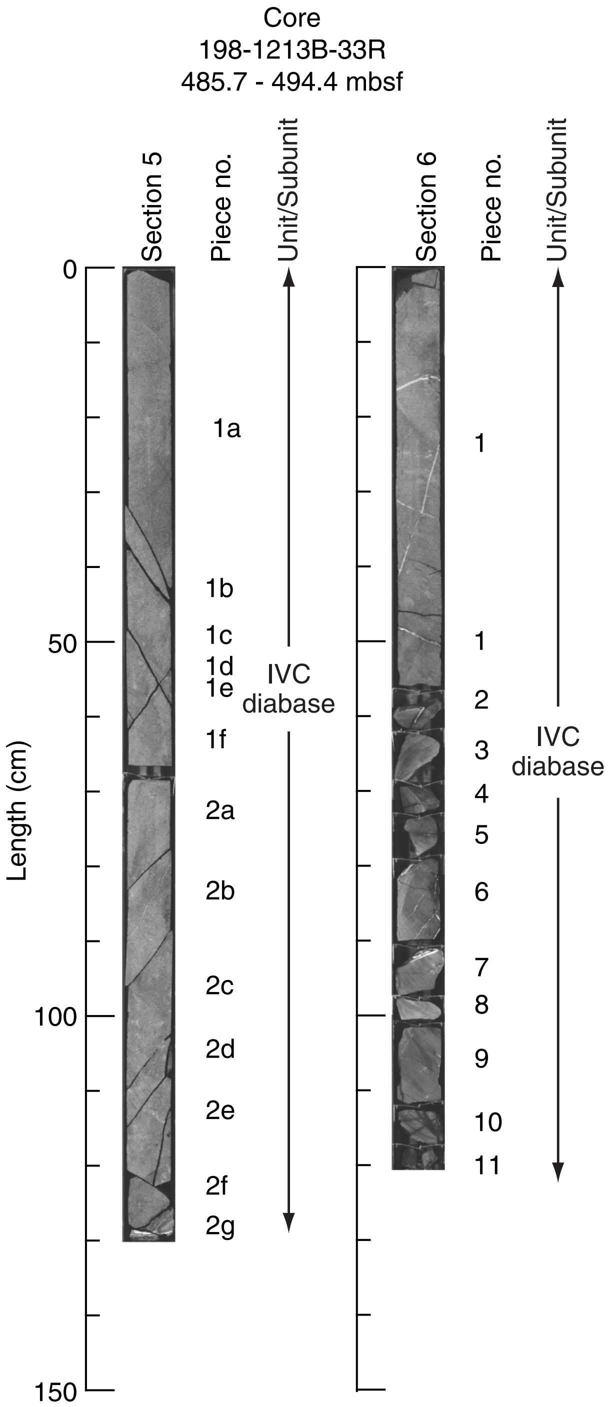

Figure F13. Close-up photograph illustrating a chilled margin (glassy basalt at 17.5–23.5 cm) above diabase and overlain by "baked" chert at 9–18 cm (interval 198-1213B-28R-1, 10–30 cm). Although the relative stratigraphy appears to be intact, contacts were destroyed during drilling.

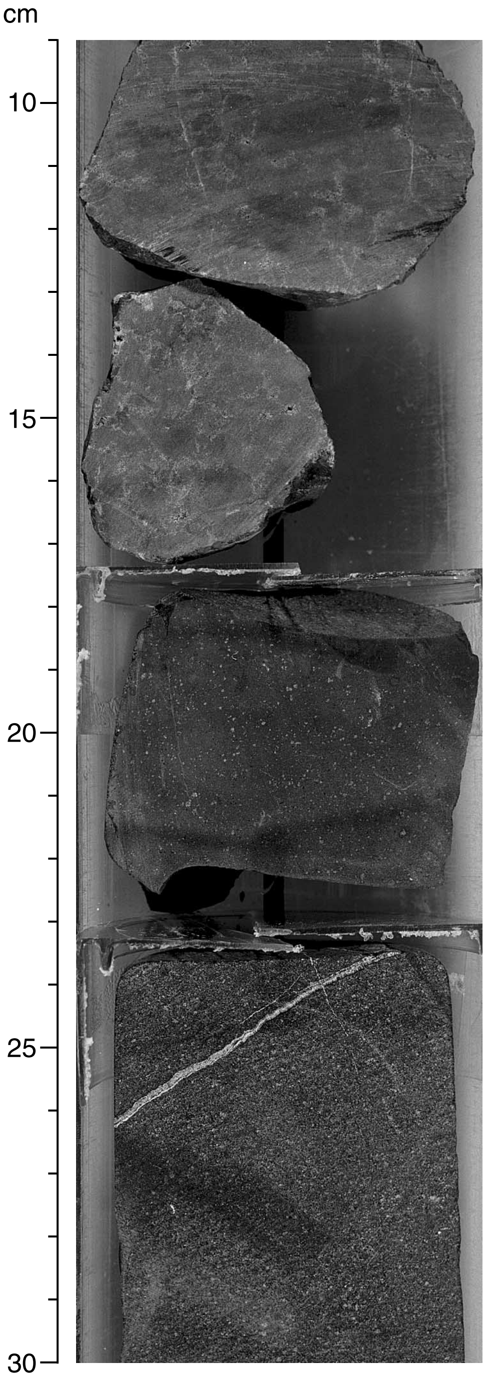

Figure F14. Close-up photograph showing basalt at 60.5–74.5 cm recovered near metamorphosed sedimentary rock with burrow structures at 66–74.5 cm (interval 198-1213B-30R-4, 60–74.5 cm). This interval is interpreted as the fragmentary record of a contact between a sill (chilled margin) and country rock (contact-metamorphosed sediments) between two overlying and underlying intervals (Subunits IVA and IVB) of diabase (not shown here).

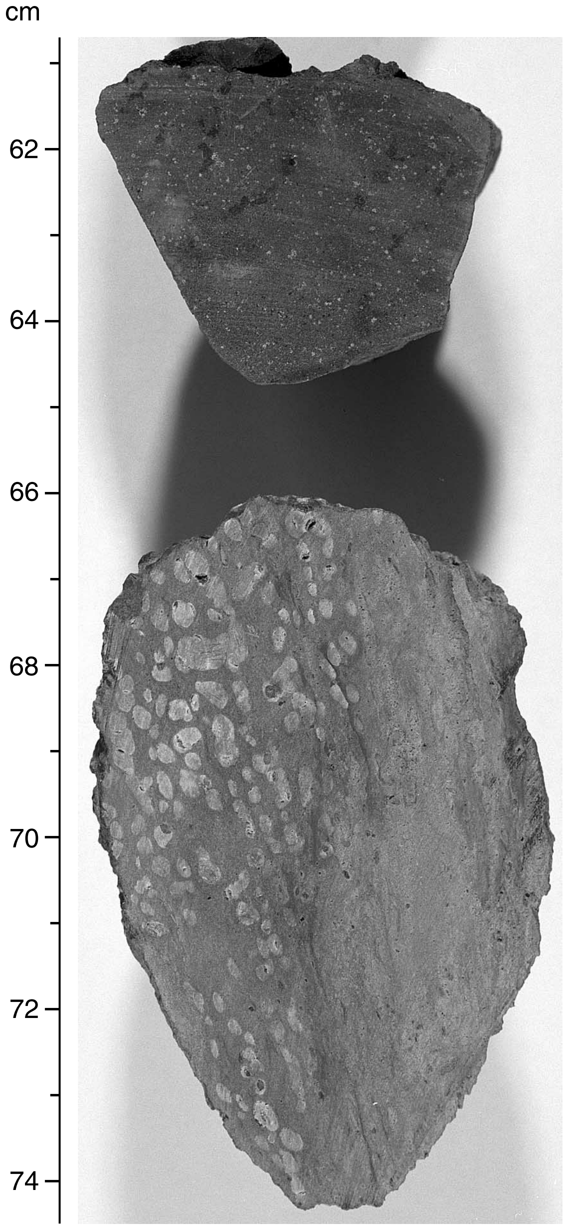

Figure F15. Close-up photograph of symmetrical basalt contact zones at 63–70 and 76–94 cm around a fragment of metachert at 71–75 cm (interval 198-1213B-32R-4, 56–99 cm). The upper gradation between basalt at 63–65 cm and diabase at 55– 63 cm is preserved in the uppermost piece. Elsewhere the basalt is fragmented (65–70 and 76–85 cm). Carbonate and clay-filled amygdules are present at 87–88 cm and glomerporphyritic clusters are present at 56, 59, 86, and 89 cm.

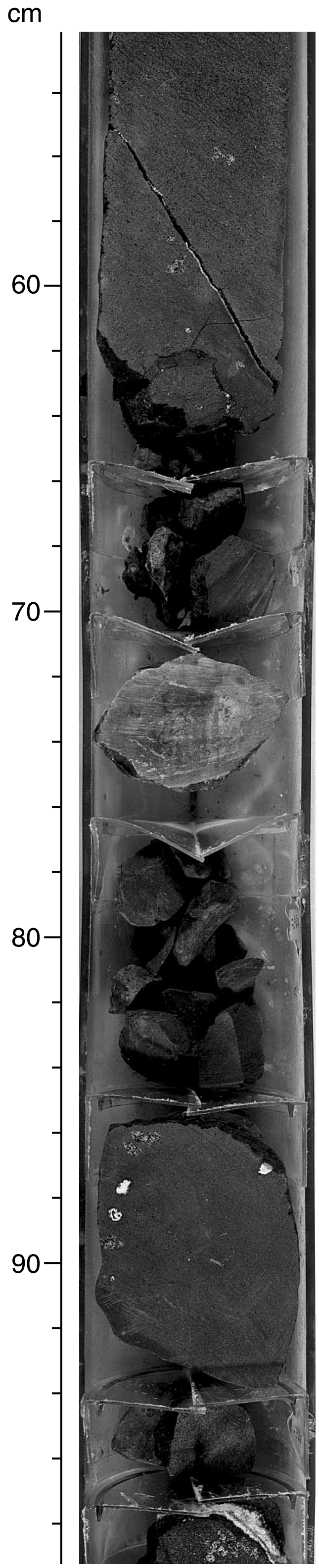

Figure F16. Photomicrographs of basalt exhibiting a sparsely phyric texture (Sample 198-1213B-31R-1, 7–10 cm). Phenocrysts of plagioclase and pyroxene are in a devitrified groundmass with radiating clusters of microlites. Hollow-appearing plagioclase microlites in the center of the view are likely a product of partial alteration or resorption. The upper view is in plane-polarized light, and the lower view is with nicols crossed.

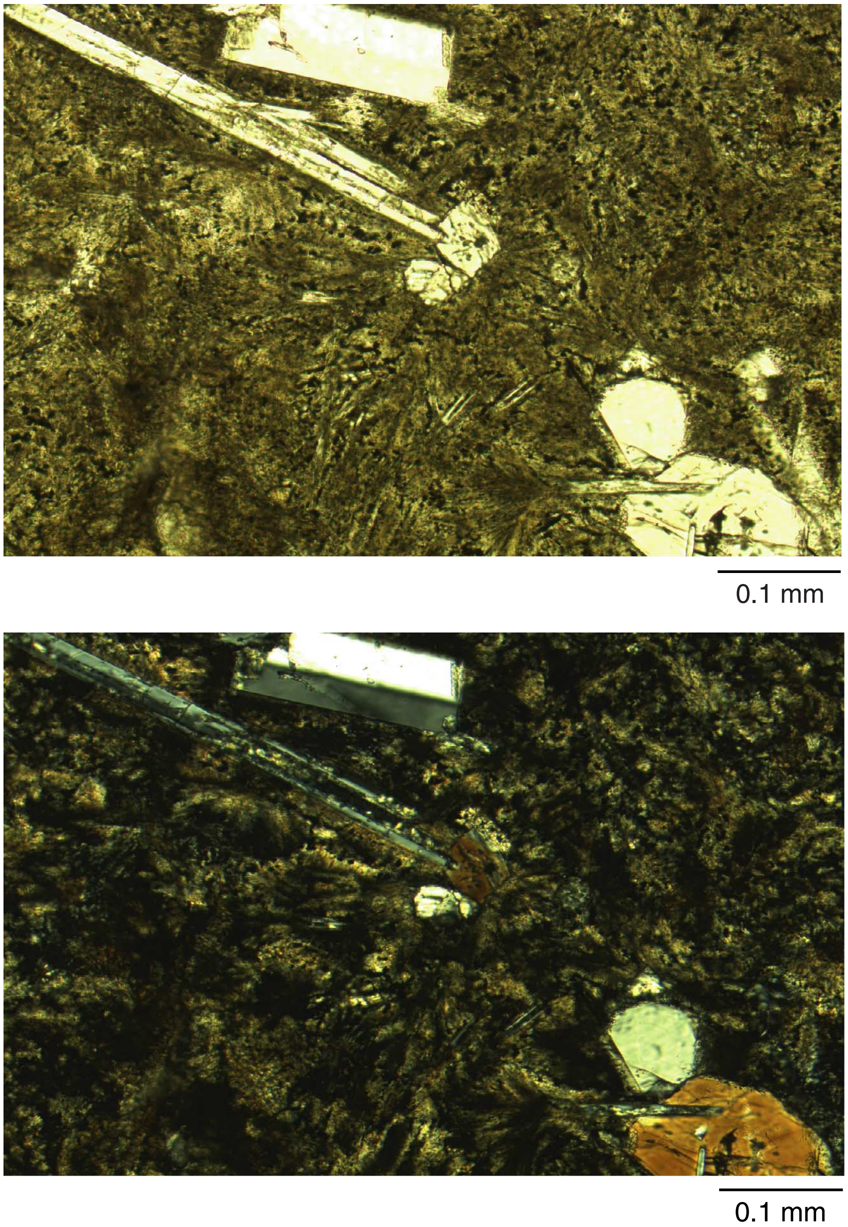

Figure F17. Photomicrographs of diabase showing intersertal to subophitic texture, with light plagioclase, clinopyroxene, and olivine crystals and (dark altered) glassy groundmass (Sample 198-1213B-28R-3, 143–145 cm). The upper view is in plane-polarized light, and the lower view is with nicols crossed.

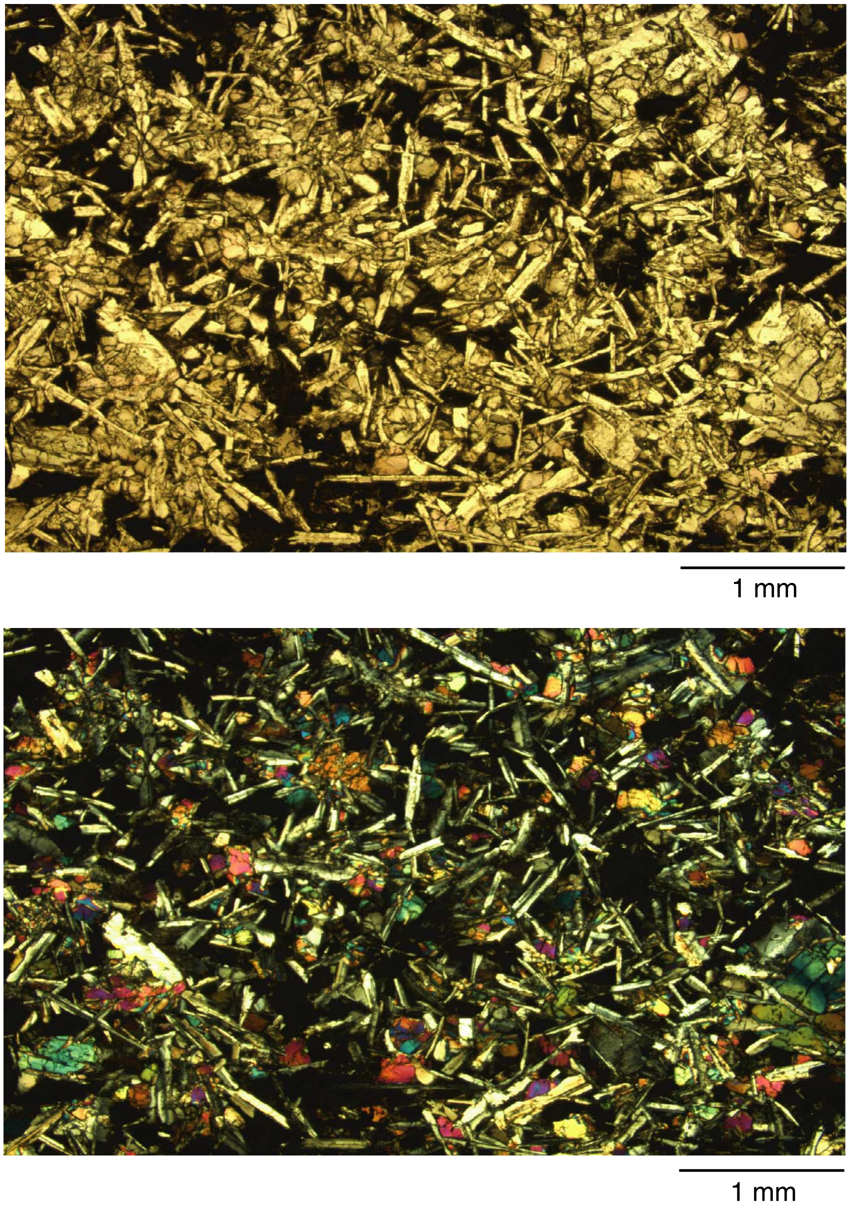

Figure F18. Photomicrographs of diabase showing subophytic texture with light plagioclase crystals encased in larger crystals of clinopyroxene and olivine (Sample 198-1213B-31R-3, 73–75 cm). Darker areas include opaque minerals and minor (altered) glassy groundmass. The upper view is in plane-polarized light, and the lower view is with nicols crossed.

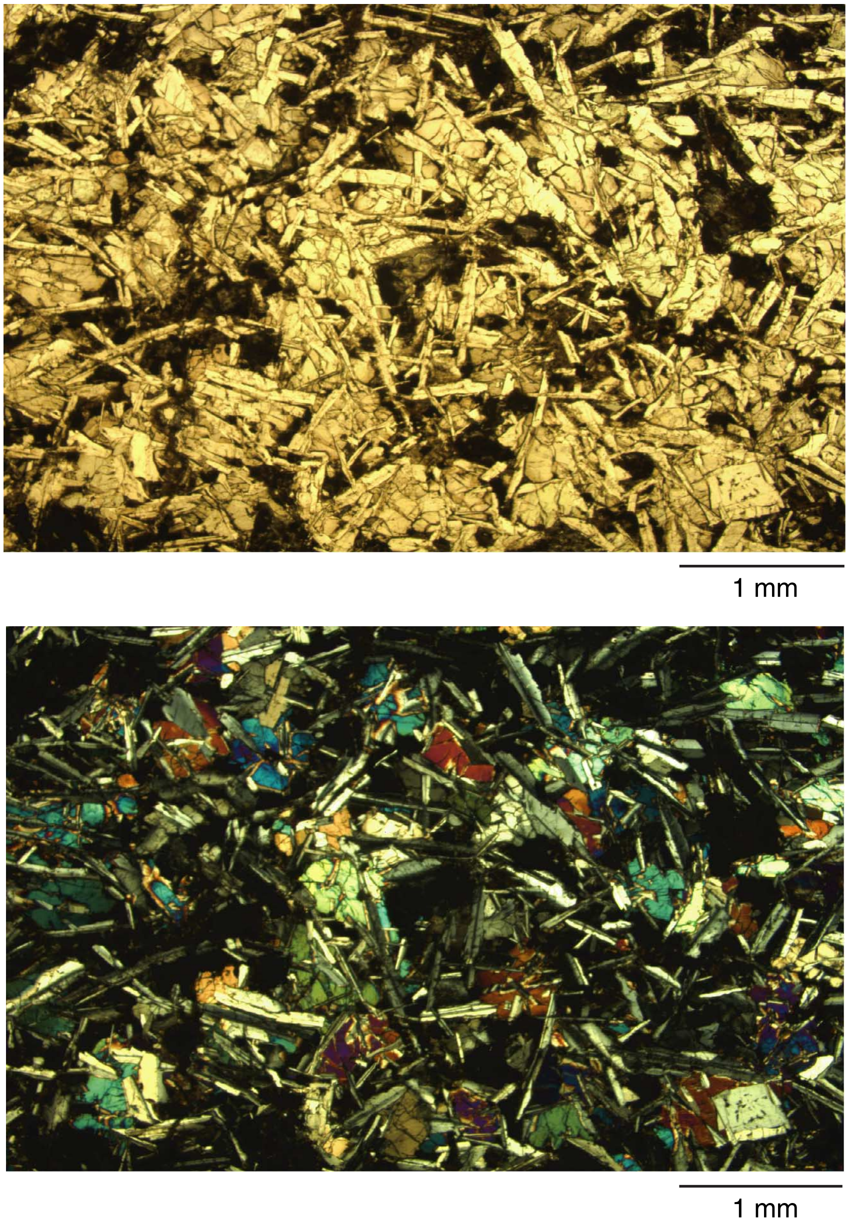

Figure F19. Photomicrographs showing striped areas thought to be pyroxene (olivine?) crystals replaced by clay minerals (Sample 198-1213B-32R-3, 72–75 cm). The "stripes" are likely shrinkage cracks produced when smectite alteration minerals were heated during thin section production. The cracks may mimic cleavage in the replaced mineral, which would favor a pyroxene precursor. Note that the crystals of opaque minerals exhibit skeletal textures. The upper view is in plane-polarized light, and the lower view is with nicols crossed.

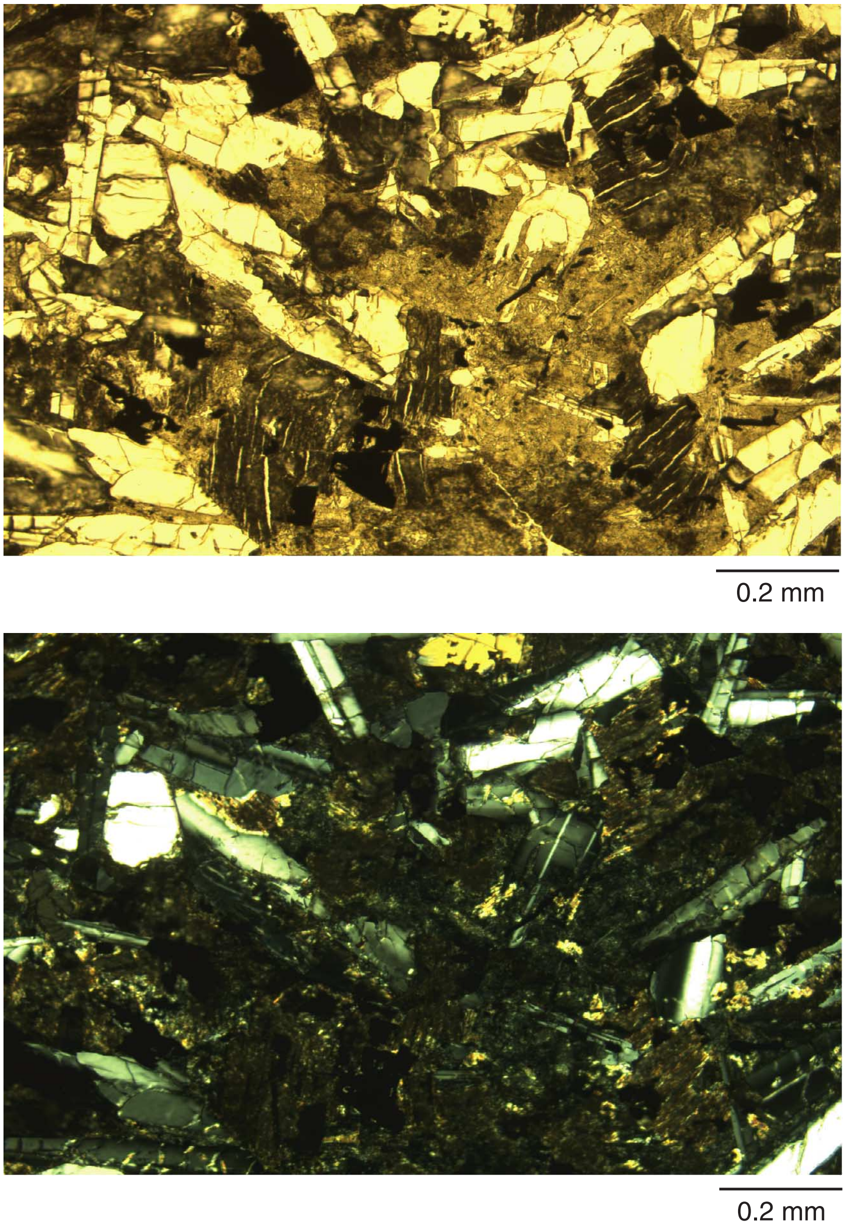

Figure F20. Photomicrographs of large glomeroporphyritic cluster of plagioclase crystals (on left) within diabase exhibiting subophytic texture (on right) (Sample 198-1213B-31R-3, 73–75 cm). The upper view is in plane-polarized light, and the lower view is with nicols crossed.

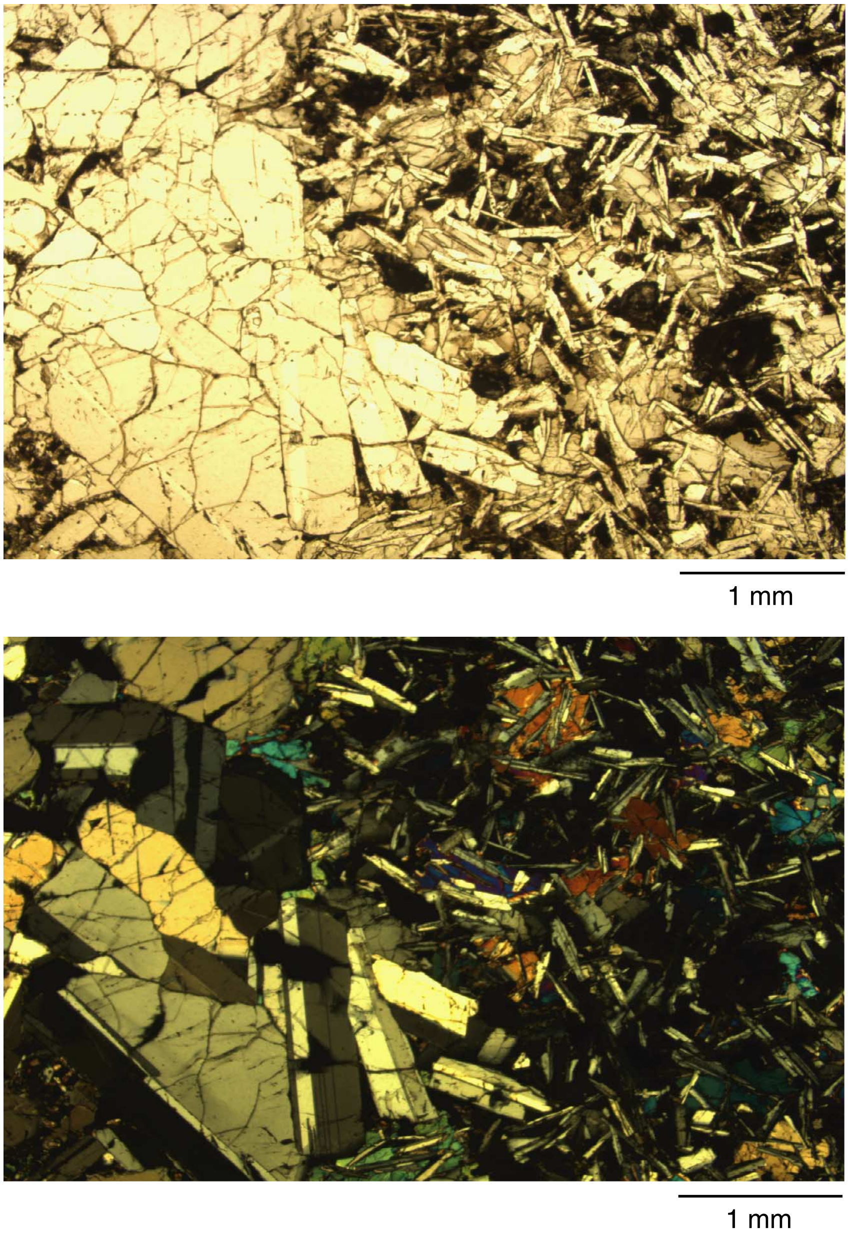

Figure F21. Close-up photograph of showing diabase cut by a zoned calcite- (white) and smectite- (dark) filled vein at 43–50 cm, which in turn is offset by several thin veins filled by mostly clay minerals and lesser calcite (interval 198-1213B-32R-5, 41–53 cm).

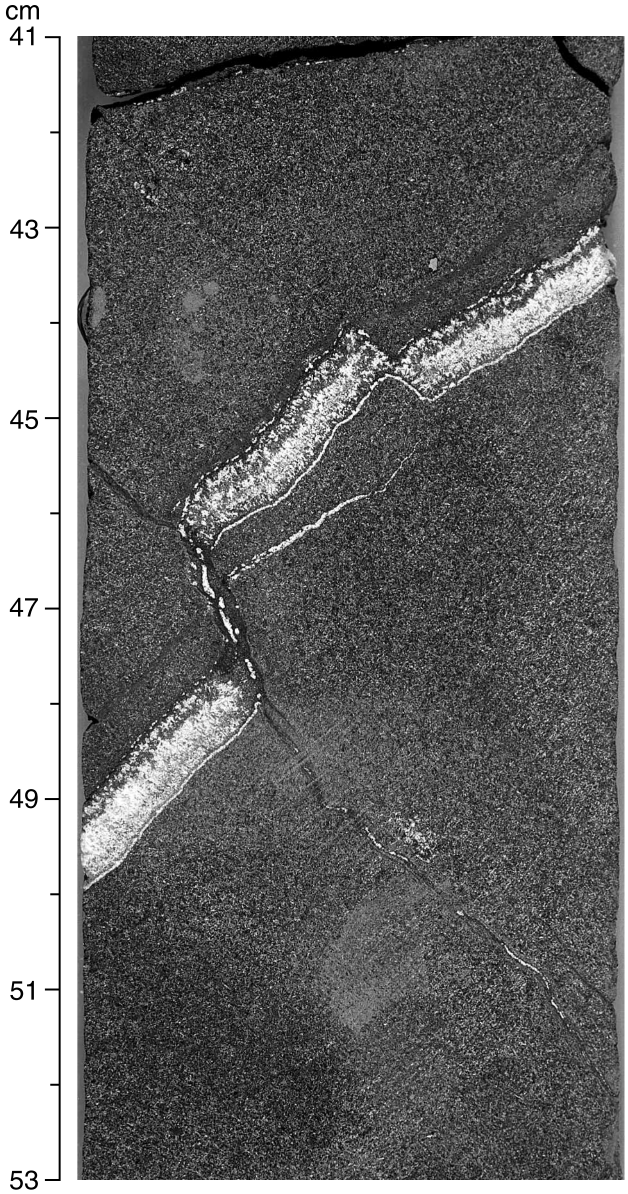

Figure F22. Photomicrographs of complex veins showing an early phase of botryoidal to bladed carbonate followed by a second phase of fibrous radiating fans of carbonate (Sample 198-1213B-31R-3, 73–75 cm). The vein fills much of the field of view. Out of the field of view, the second phase is associated with minor quartz. Darker (more isotropic) areas on either side of the carbonate cement are clay-rich alteration zones. On the right, the alteration zone is crossed by later fractures filled by carbonate. Unaltered host rock can be seen on the extreme left. The upper view is in plane-polarized light, and the lower view is with nicols crossed.

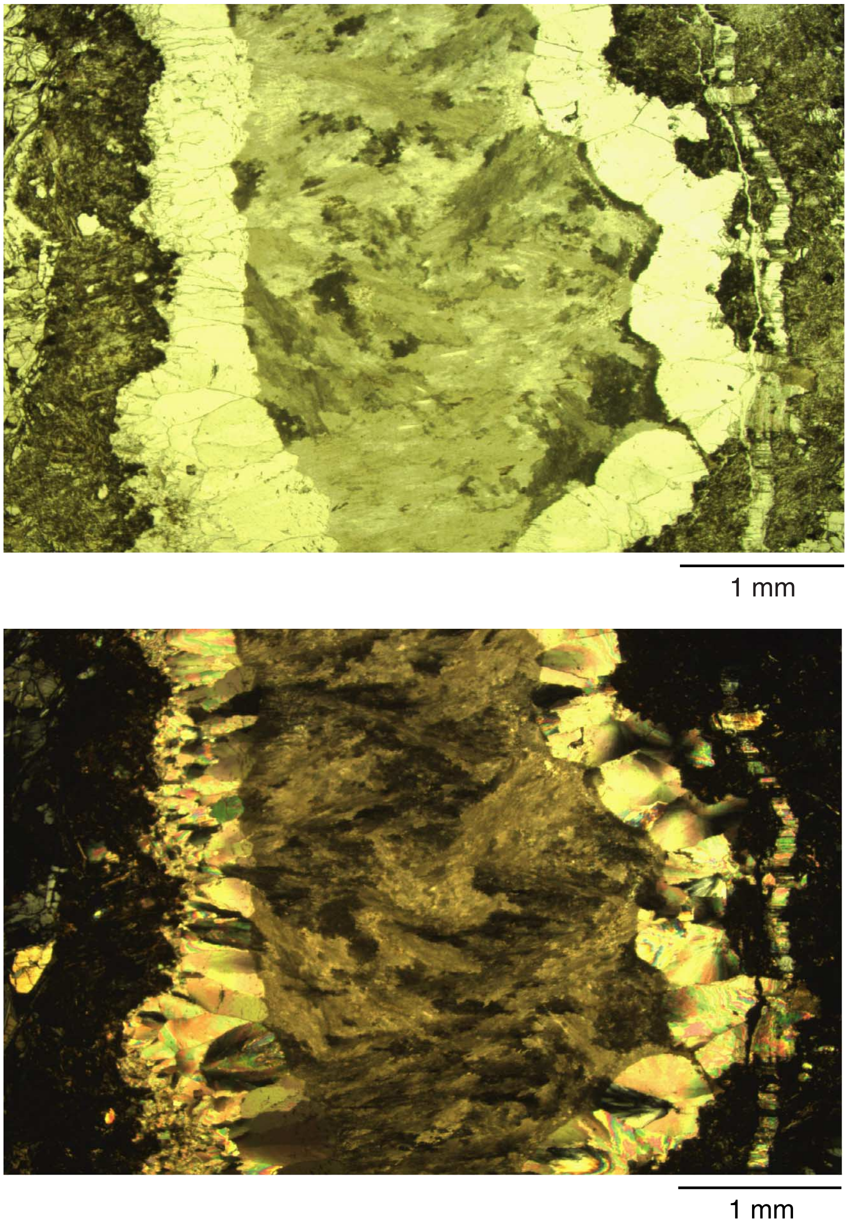

Figure F23. Photomicrographs showing radiating fibrous crystals (metamorphic minerals?) encased in microcrystalline quartz within a former burrow structure in metachert (Sample 198-1213B-32R-4, 71–74 cm). The upper view is in plane-polarized light, and the lower view is with nicols crossed.

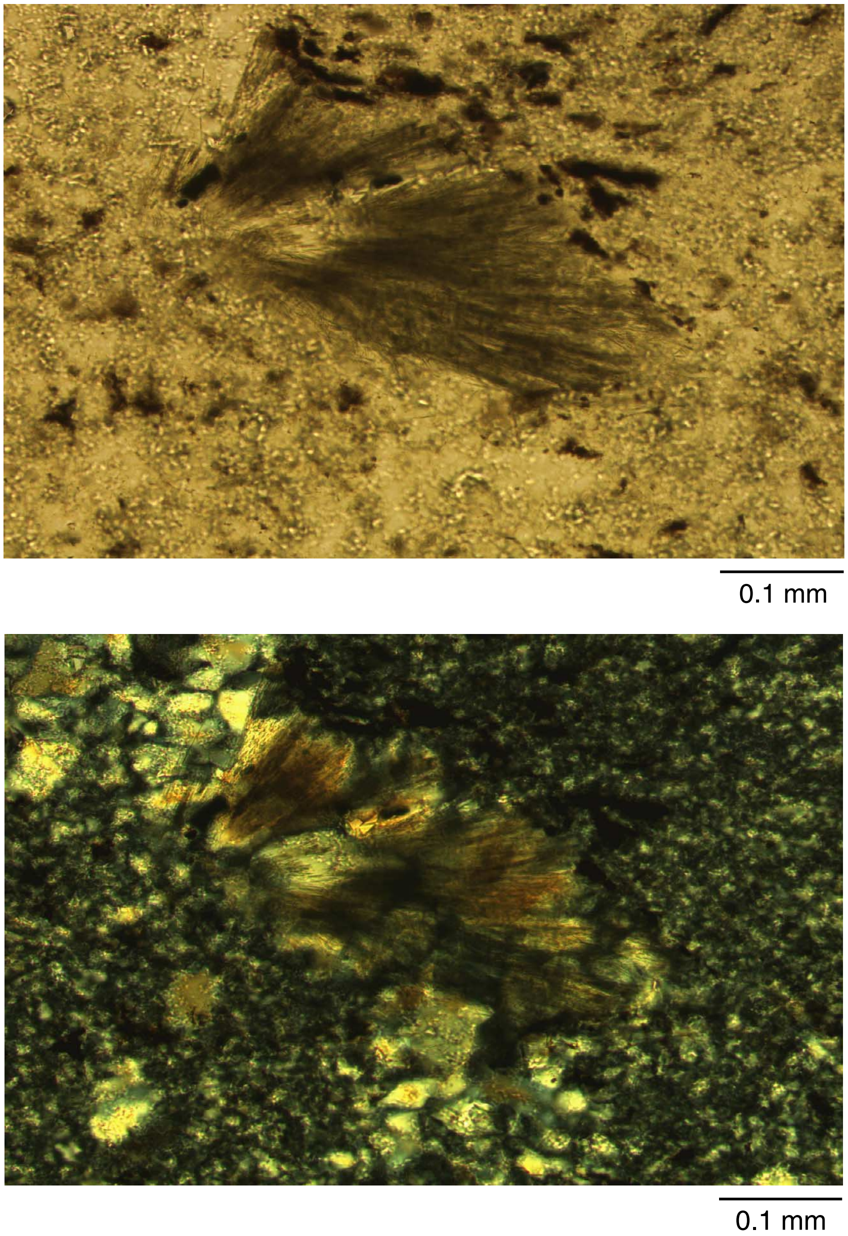

Figure F24. Photomicrographs showing a large plagioclase phenocryst with complex zonation (Sample 198-1213B-33R-6, 106–108 cm). One zone is preferentially altered to green clay minerals, along with minerals in surrounding groundmass. The upper view is in plane-polarized light, and the lower view is with nicols crossed.

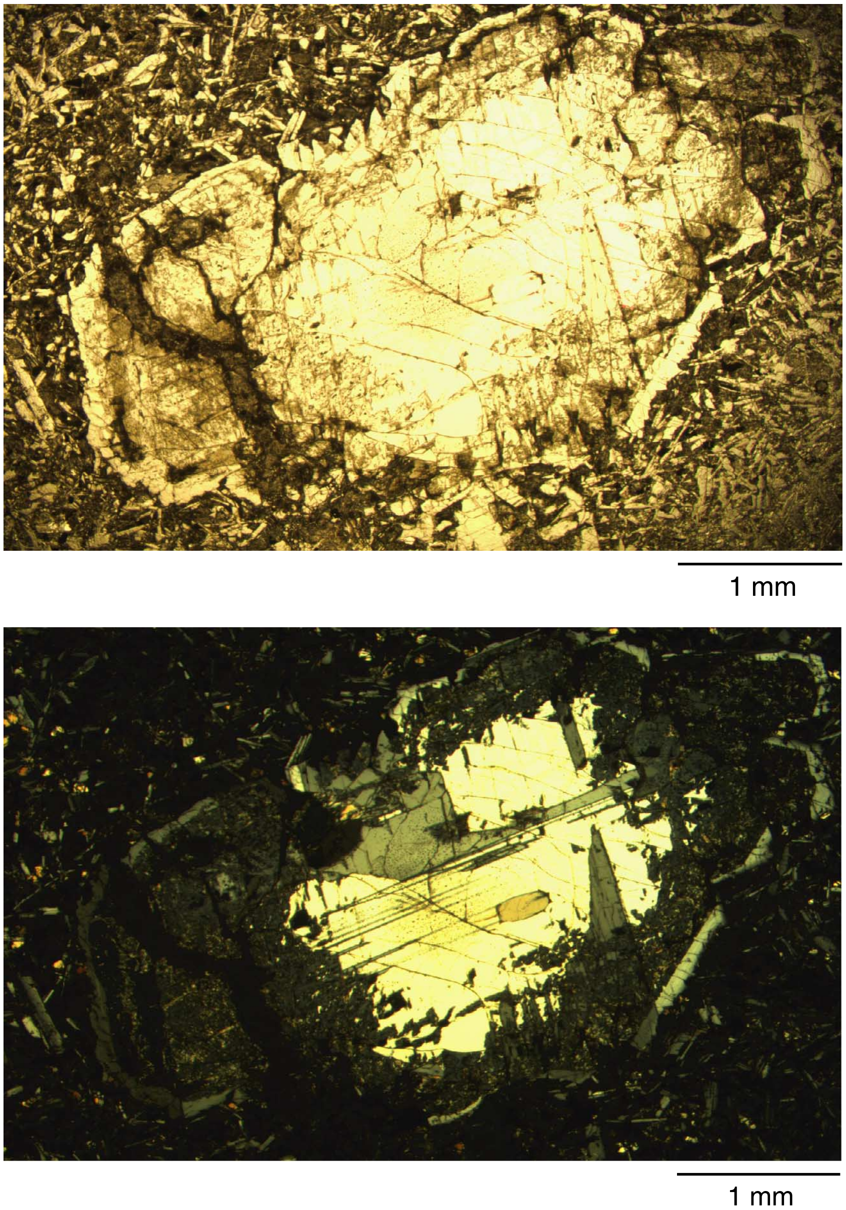

Figure F25. Estimated paleodepth of Site 1213. Squares show estimated paleowater depths based on benthic foraminiferal assemblages from selected core catcher samples. The curve is based on the backtracked data (Pacific Ocean) of DSDP and ODP samples (Kaiho, 1999). The present-day depth of Site 1213 is 3883 m.

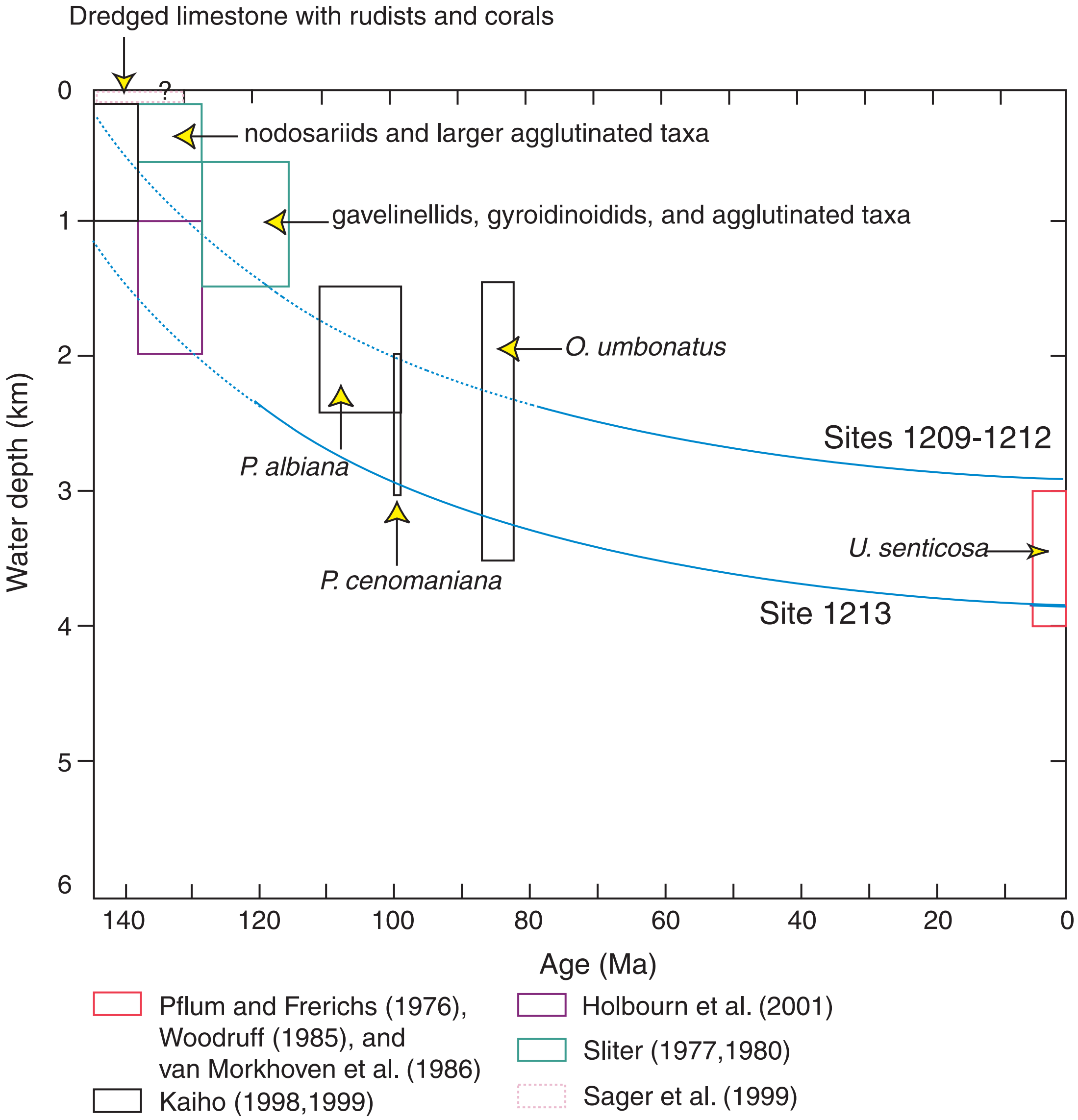

Figure F26. Plot of magnetic inclination vs. depth for the igneous section of Hole 1213B. Measurements shown are averages from core sections where long contiguous pieces were recovered. Mean inclinations have been corrected for bias caused by averaging inclination-only data using the method of Cox and Gordon (1984). Error bars show one standard deviation.

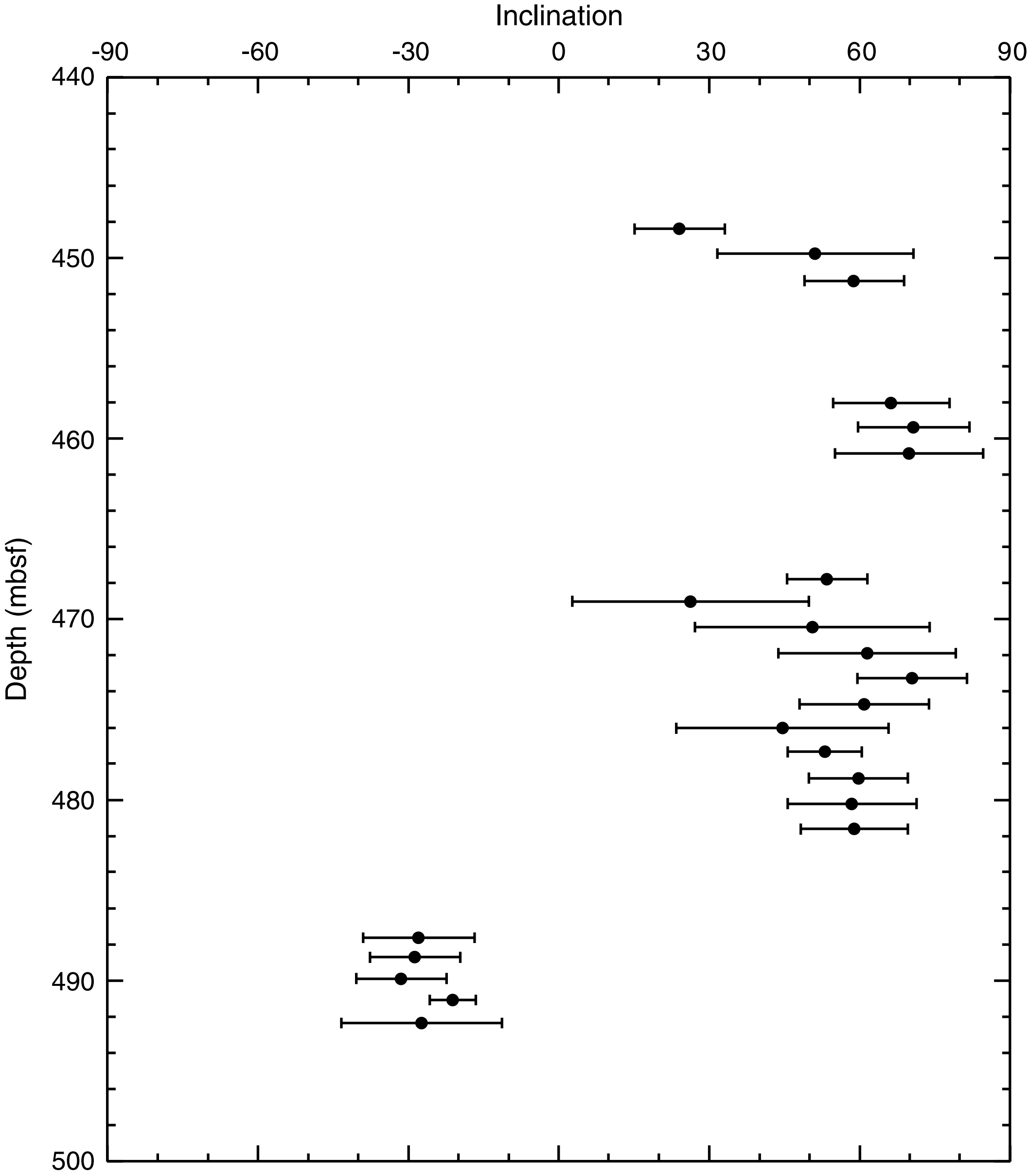

Figure F27. Age-depth plot of calcareous nannofossil (diamonds) and planktonic foraminiferal (crosses) datums at Site 1213. Horizontal lines represent unconformities in the section. Datum ages and depths are presented in Tables T5, p. 96, and T6, p. 97 (see "Biostratigraphy," p. 18).

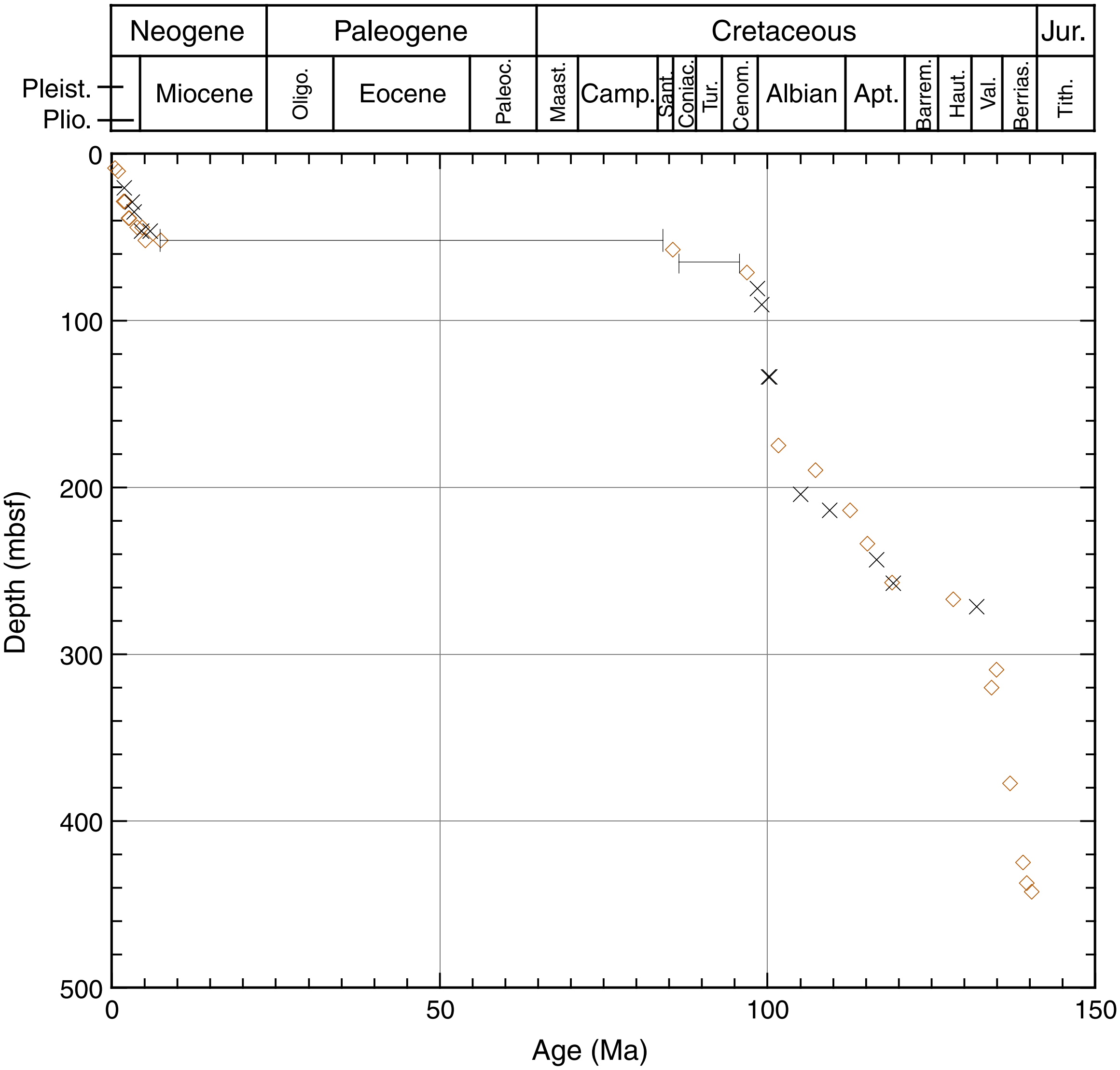

Figure F28. Age-depth plot of Neogene calcareous nannofossil (diamonds) and planktonic foraminiferal (crosses) datums at Site 1213. Horizontal lines represent unconformities in the section. Datum ages and depths are presented in Tables T5, p. 96, and T6, p. 97. FO = first occurrence, LO = last occurrence.

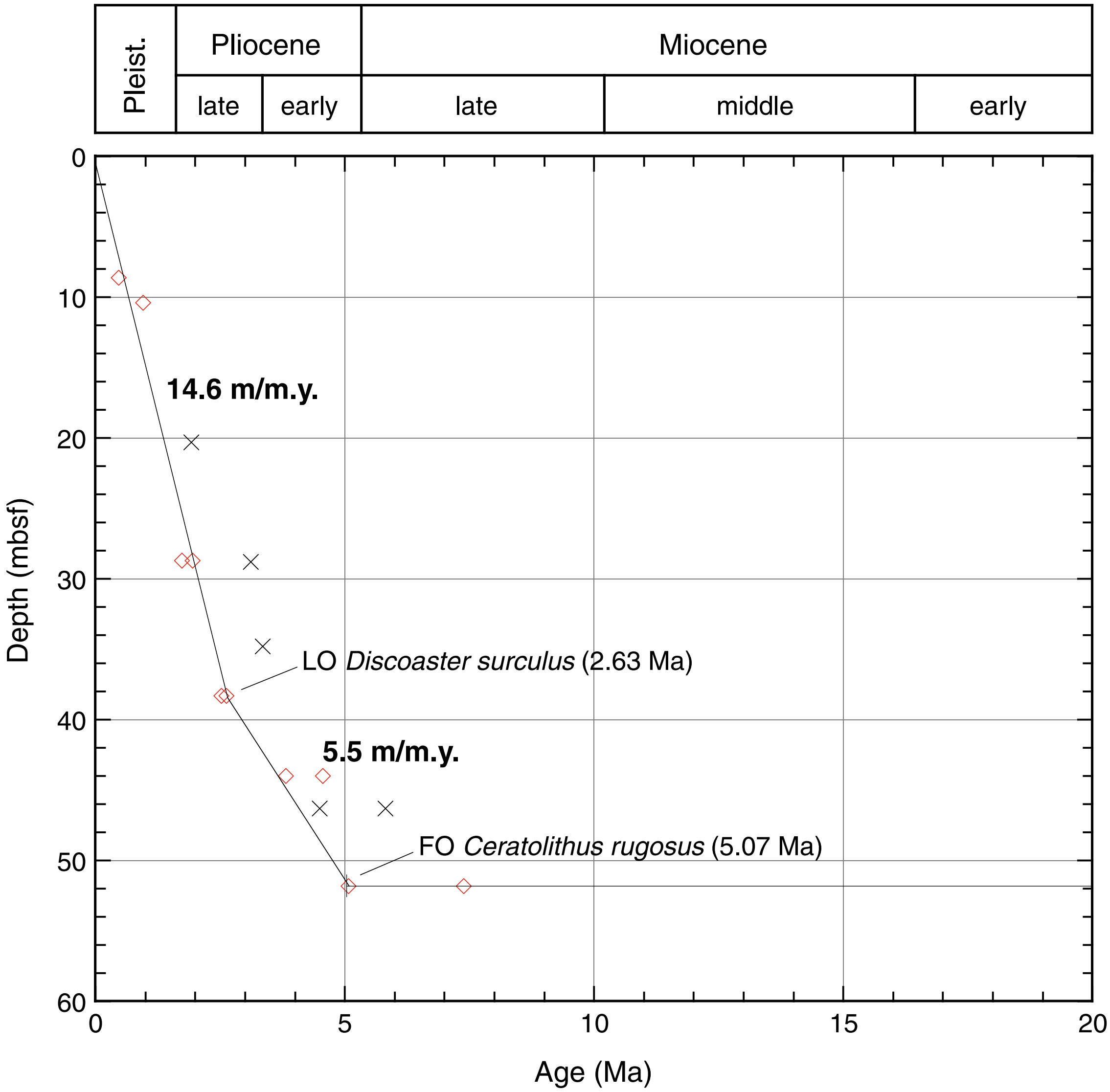

Figure F29. Age-depth plot of Late Cretaceous–latest Jurassic (mid- to late Cenomanian–late Tithonian) calcareous nannofossil (diamonds) and planktonic foraminiferal (crosses) datums at Site 1213, together with radiolarian zones (circles connected by a line mark the upper and lower limits of the Unitary Association Zones; boxes depict the stratigraphic range of radiolarian zones). Horizontal lines with truncated ends represent unconformities in the section (see discussion in text). Datum ages and depths are presented in Tables T5, p. 96, and T6, p. 97. FO = first occurrence, LO = last occurrence, OAE1a = Aptian Oceanic Anoxic Event.

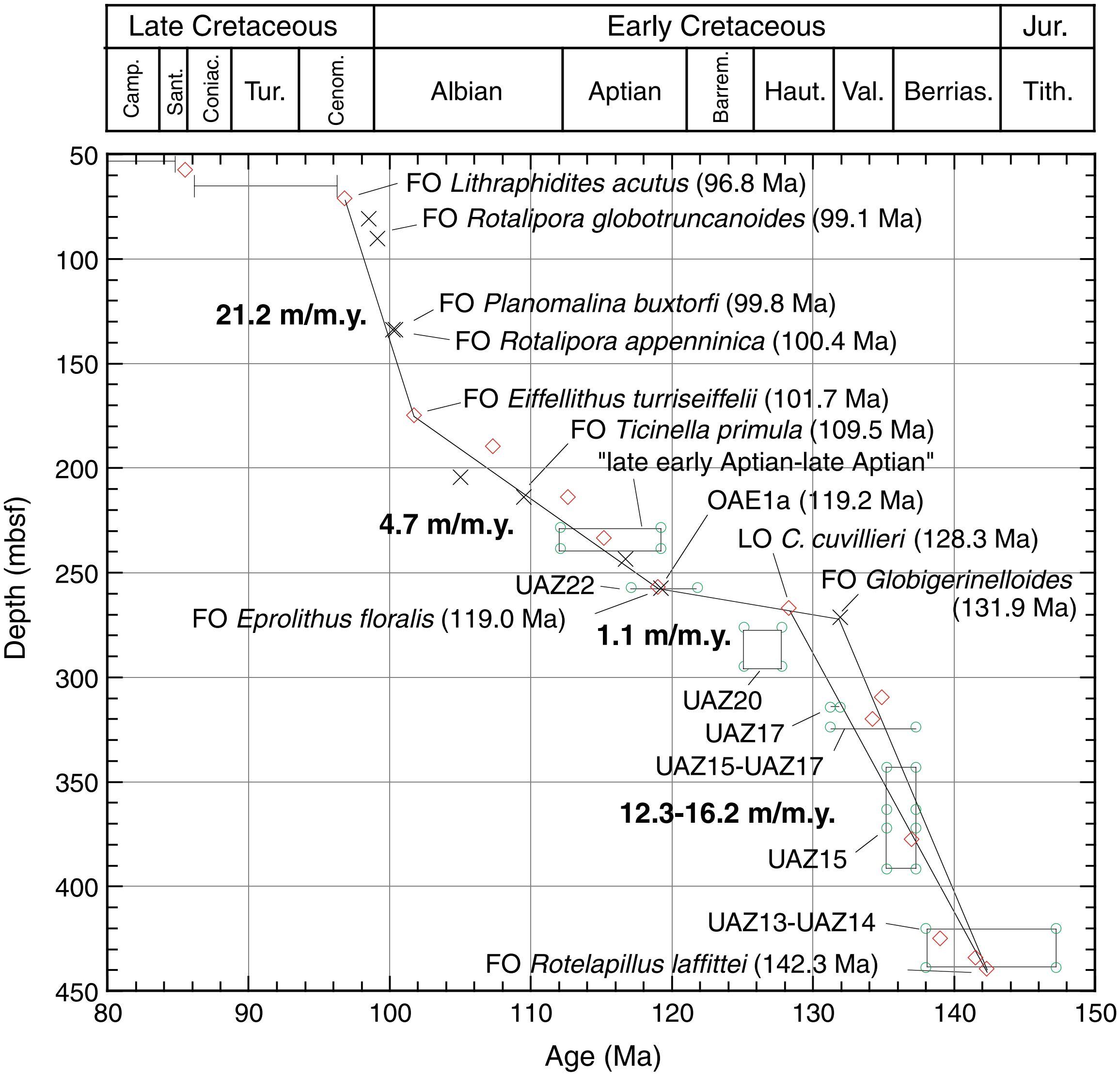

Figure F30. Downhole profile of carbonate content in Holes 1213A and 1213B and organic carbon content of samples from C_{org}-rich horizons in the lower Aptian (OAE1a) (Section 198-1213B-8R-1) and Valanginian (Samples 198-1213B-15R-1, 9–10 cm, and 19R-1, 112–113 cm).

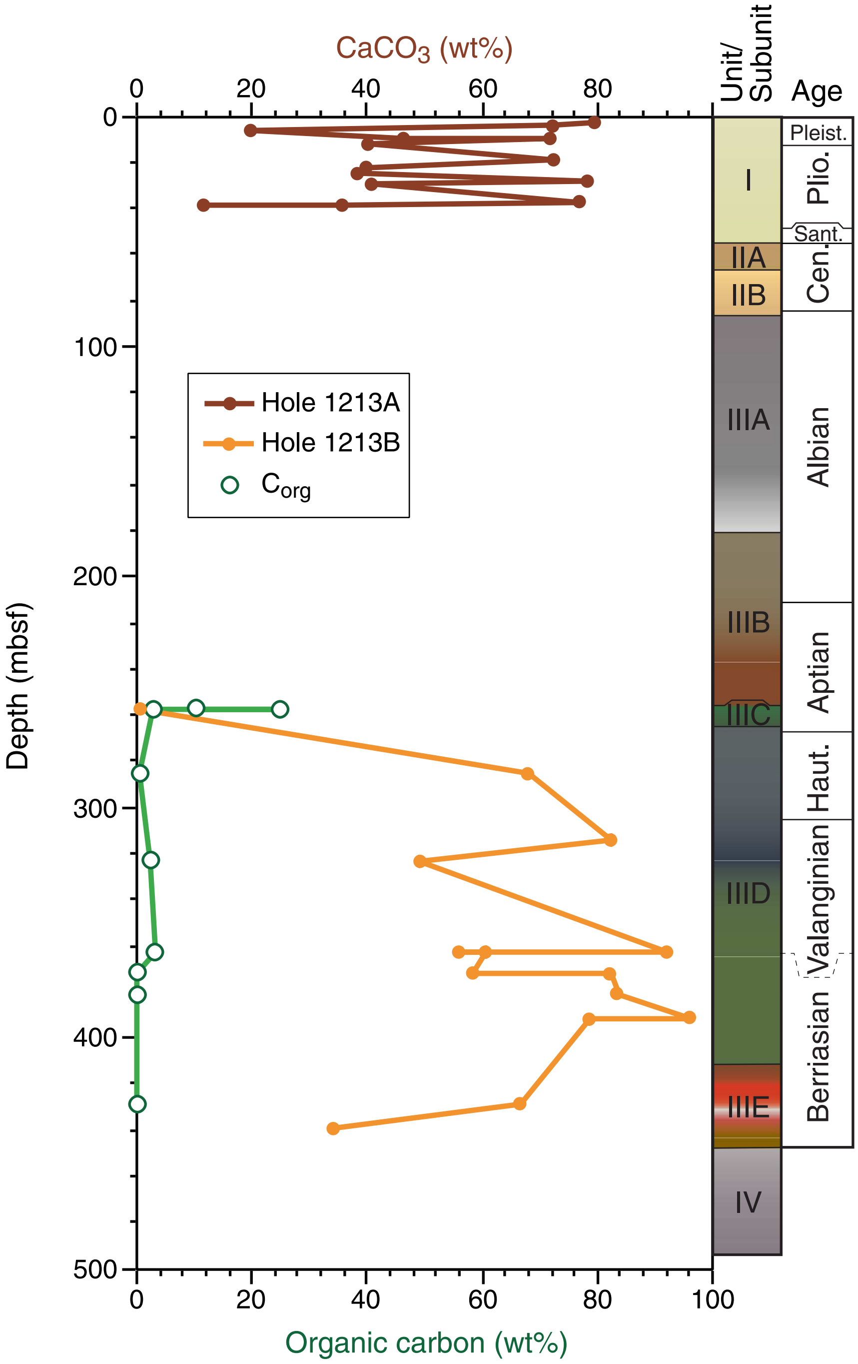

Figure F31. Oxygen and hydrogen indices for samples from the lower Aptian organic-rich horizon (OAE1a) (Table T12, p. 103) plotted on a modified van Krevelen diagram. The characteristics of organic-rich samples from Site 1207 and from the Aptian at Sites 463 and 866 in the mid-Pacific are also shown. The size of the data points is proportional to organic carbon content. The lines designated I, II, and III represent the evolutionary trends with thermal maturation of the three major kerogen types (Tissot et al., 1974). OI = oxygen index, TOC = total organic carbon.

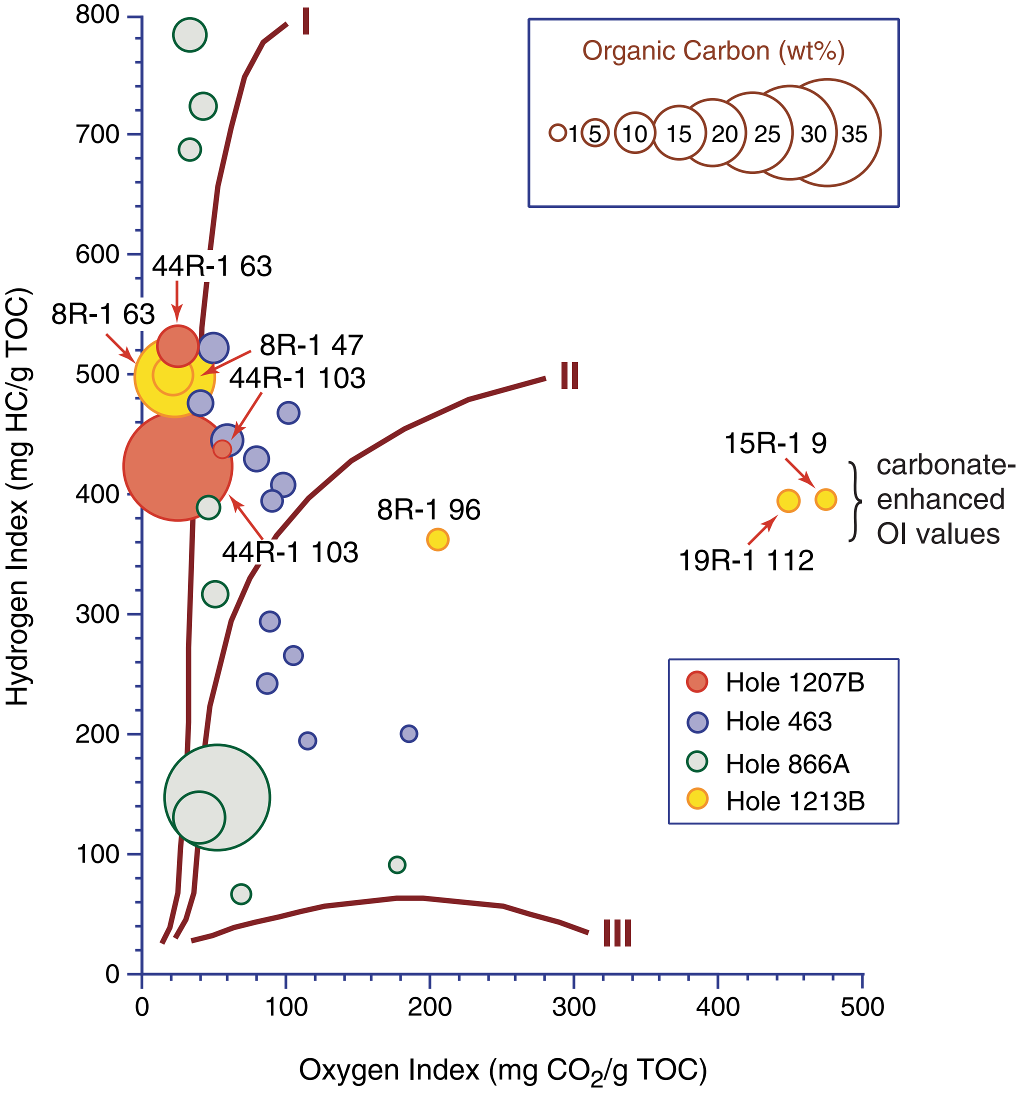

Figure F32. GC-MS traces of aliphatic hydrocarbons for samples from organic-rich intervals of Hole 1213B. Numbers refer to *n*-alkanes of the designated carbon number. Peak identities are given in Table T15, p. 106. (Continued on next page.)

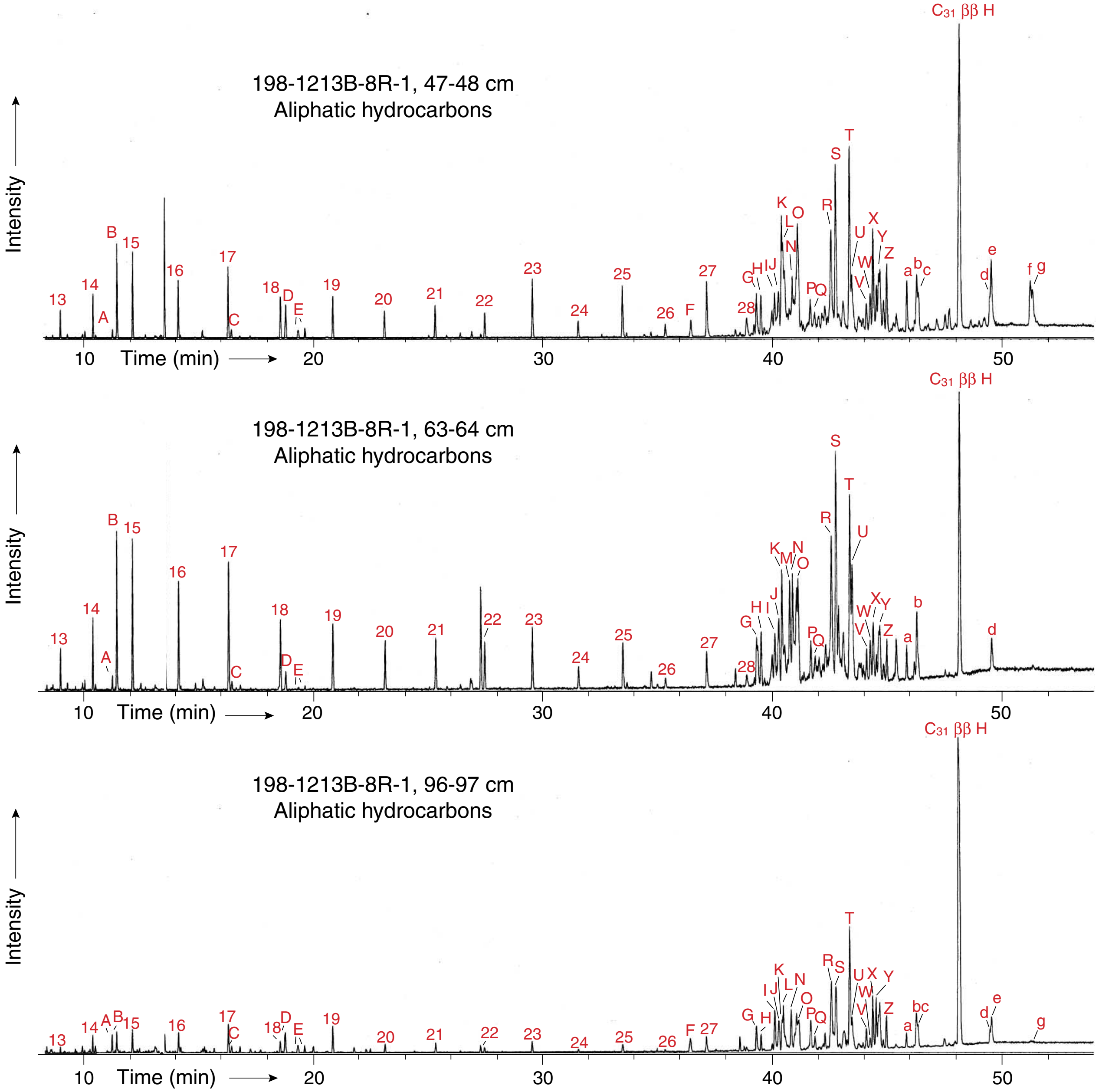

Figure F32 (continued).

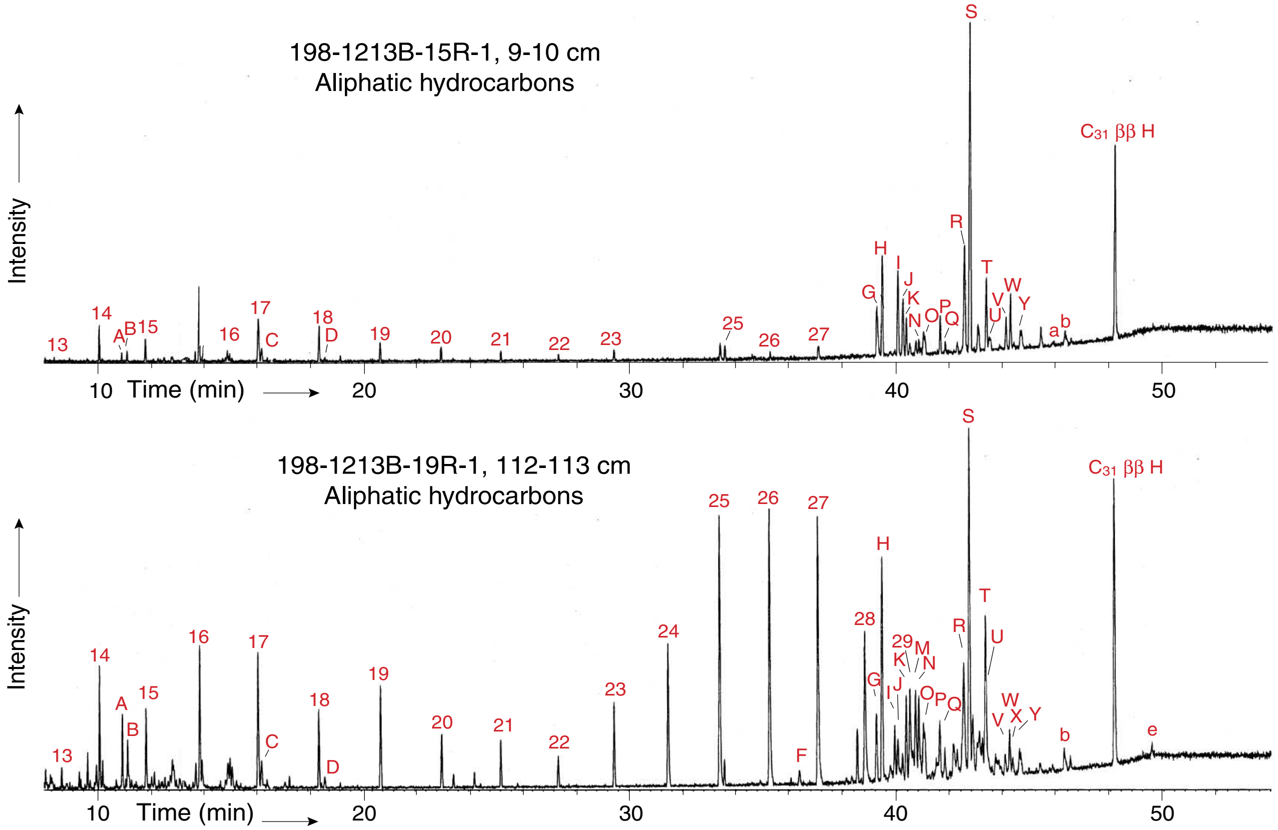

198-1213B-15R-1, 9-10 cm
Aliphatic hydrocarbons

198-1213B-19R-1, 112-113 cm
Aliphatic hydrocarbons

Figure F33. GC-MS traces of ketone fractions for samples from organic-rich intervals of Hole 1213B. Peak identities are given in Table T16, p. 107. (Continued on next page.)

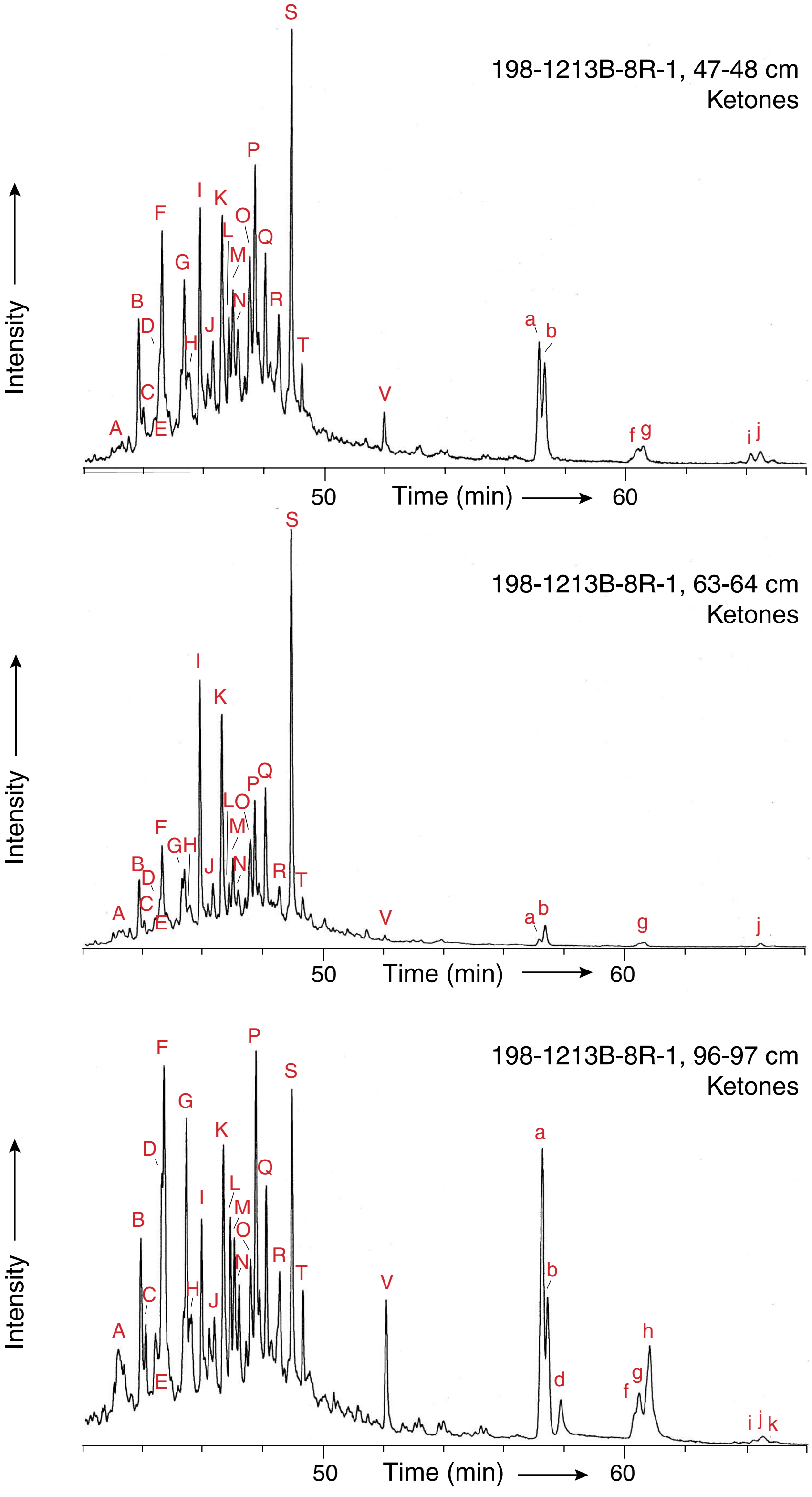

Figure F33 (continued).

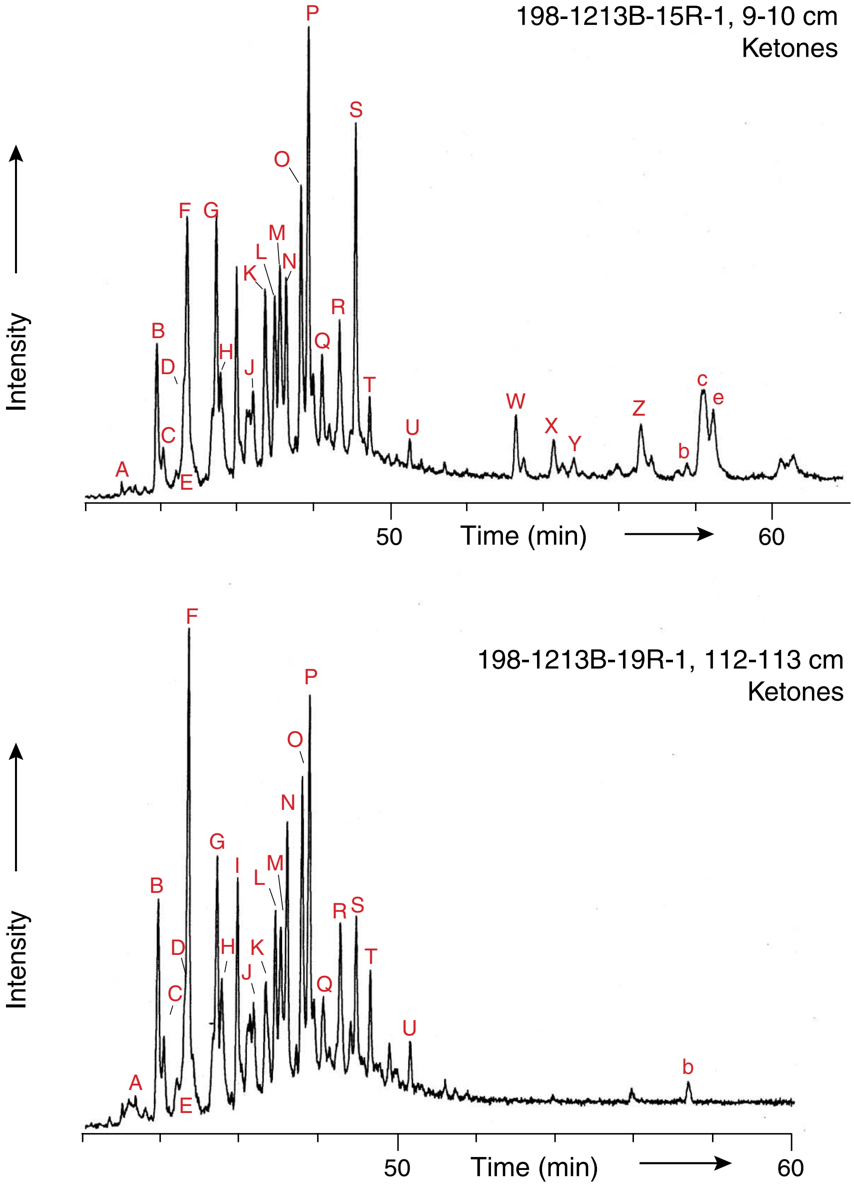

Figure F34. MST magnetic susceptibility measured in whole cores from Holes 1213A and 1213B plotted vs. depth. The accurate correction factor for these raw instrument values is 0.68 × 10^{-5}.

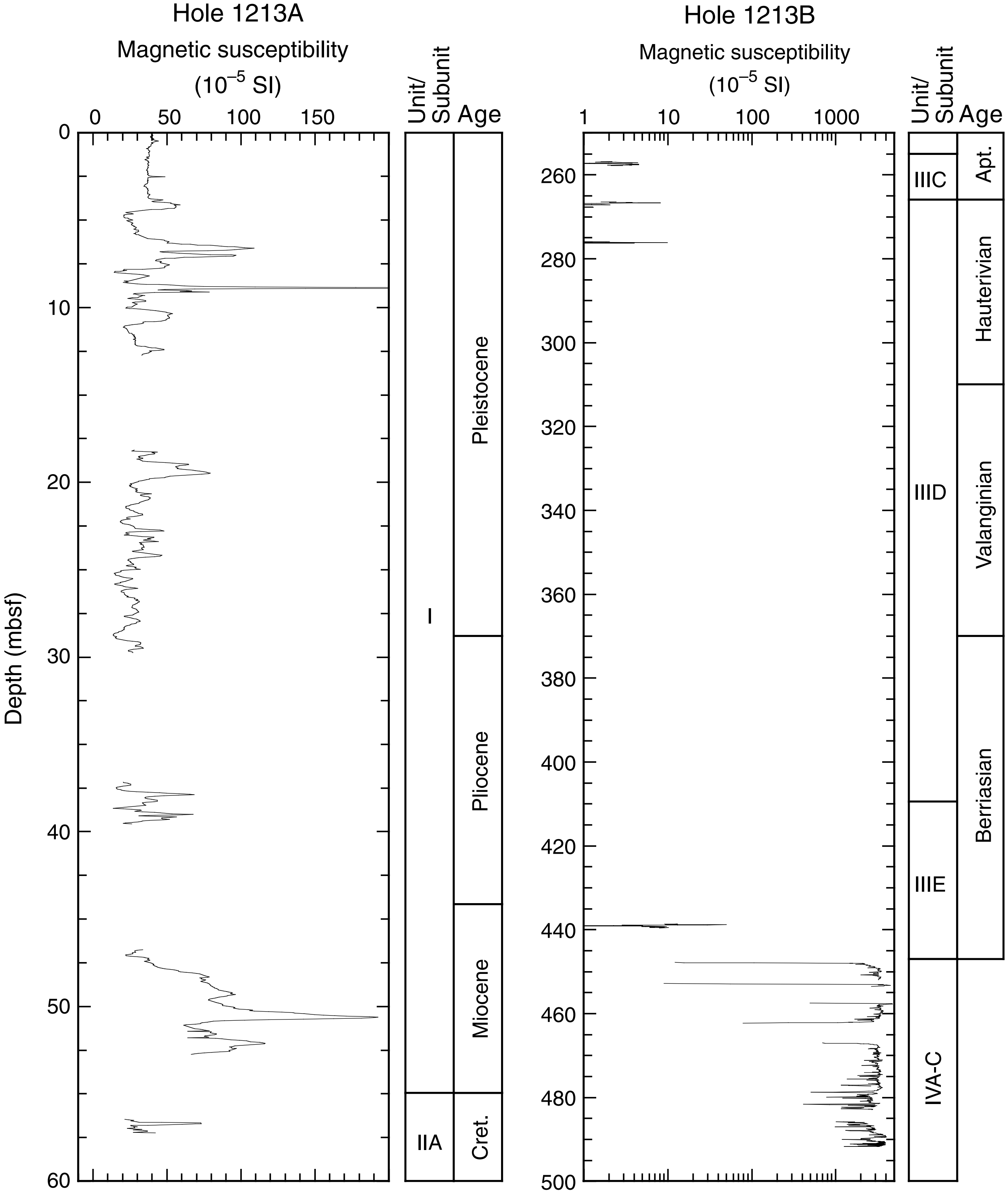

Figure F35. MST gamma ray attenuation (GRA) bulk density measured in whole cores from Holes 1213A and 1213B plotted vs. depth.

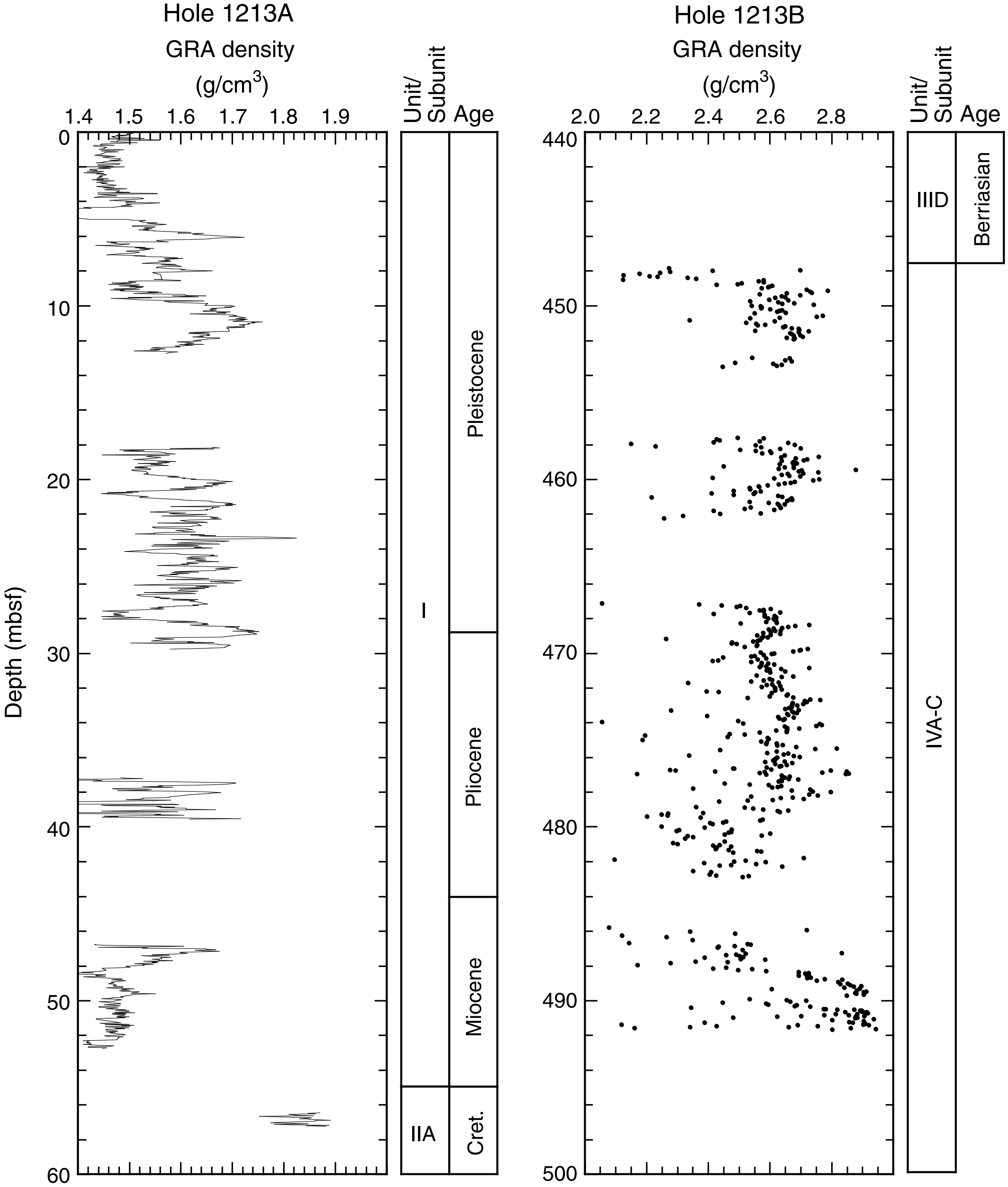

Figure F36. MST natural gamma radiation data for Hole 1213B plotted vs. depth.

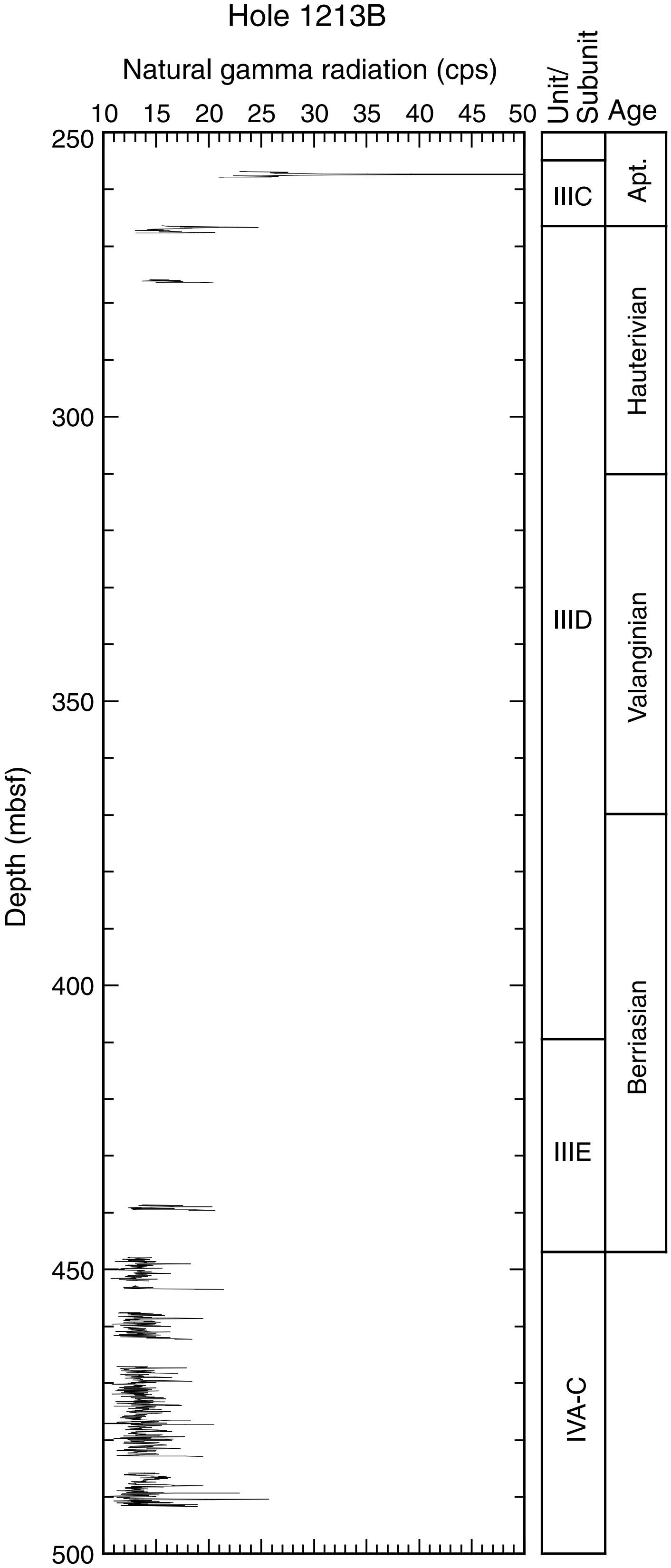

Figure F37. *P*-wave velocities for discrete samples from Holes 1213A and 1213B (see Table T18, p. 109, for data). Blue squares = porcellanite, black squares = radiolarite, green triangles = chalk and limestone, red circles = chert, blue circles = diabase, orange triangle = hydrothermally altered sediment.

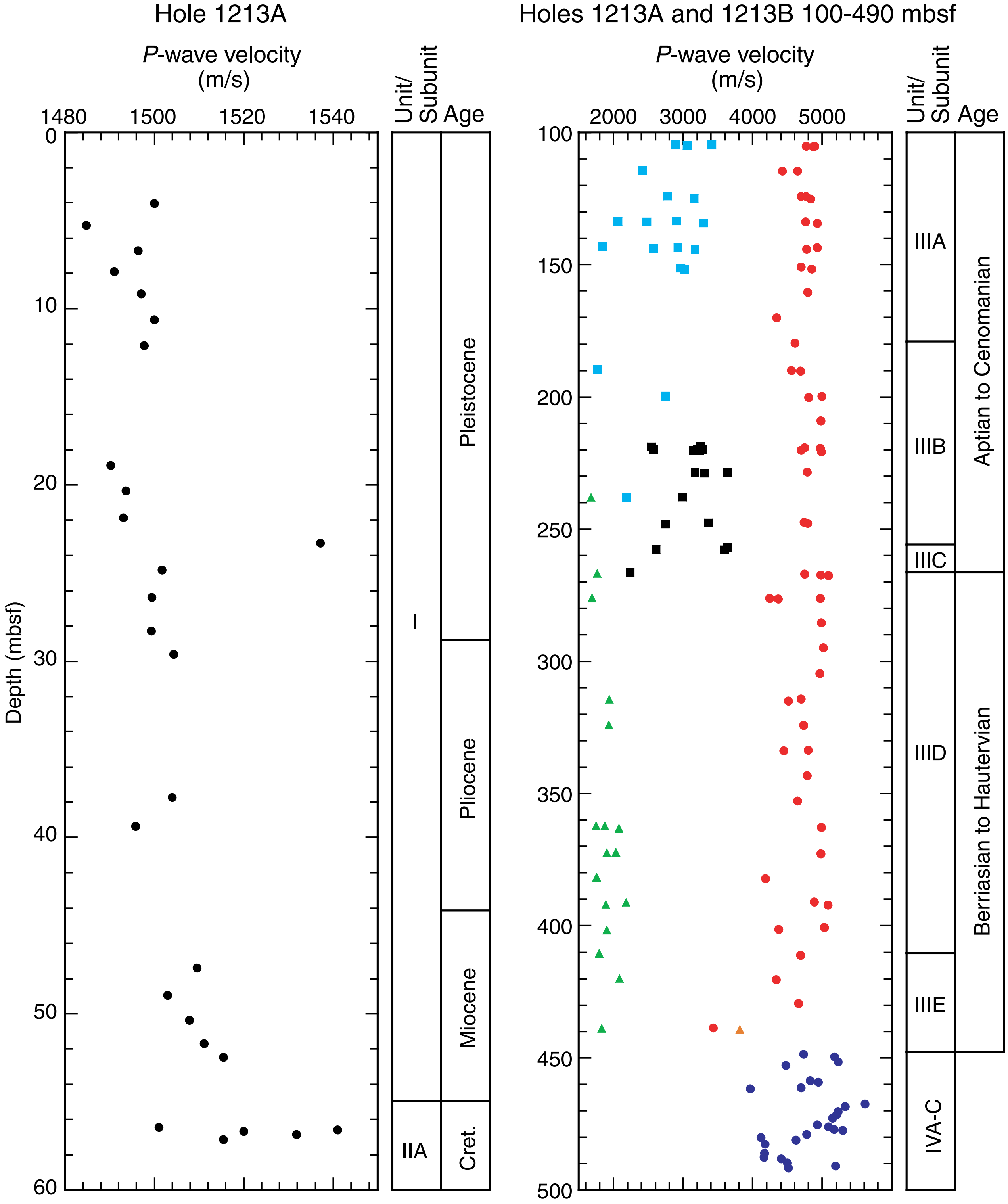

Figure F38. Geophysical logs and equivalent core physical properties measurements in Hole 1213B. Lith. = lithologic, PEF (corr.) = photoelectric effect (corrected for porosity).

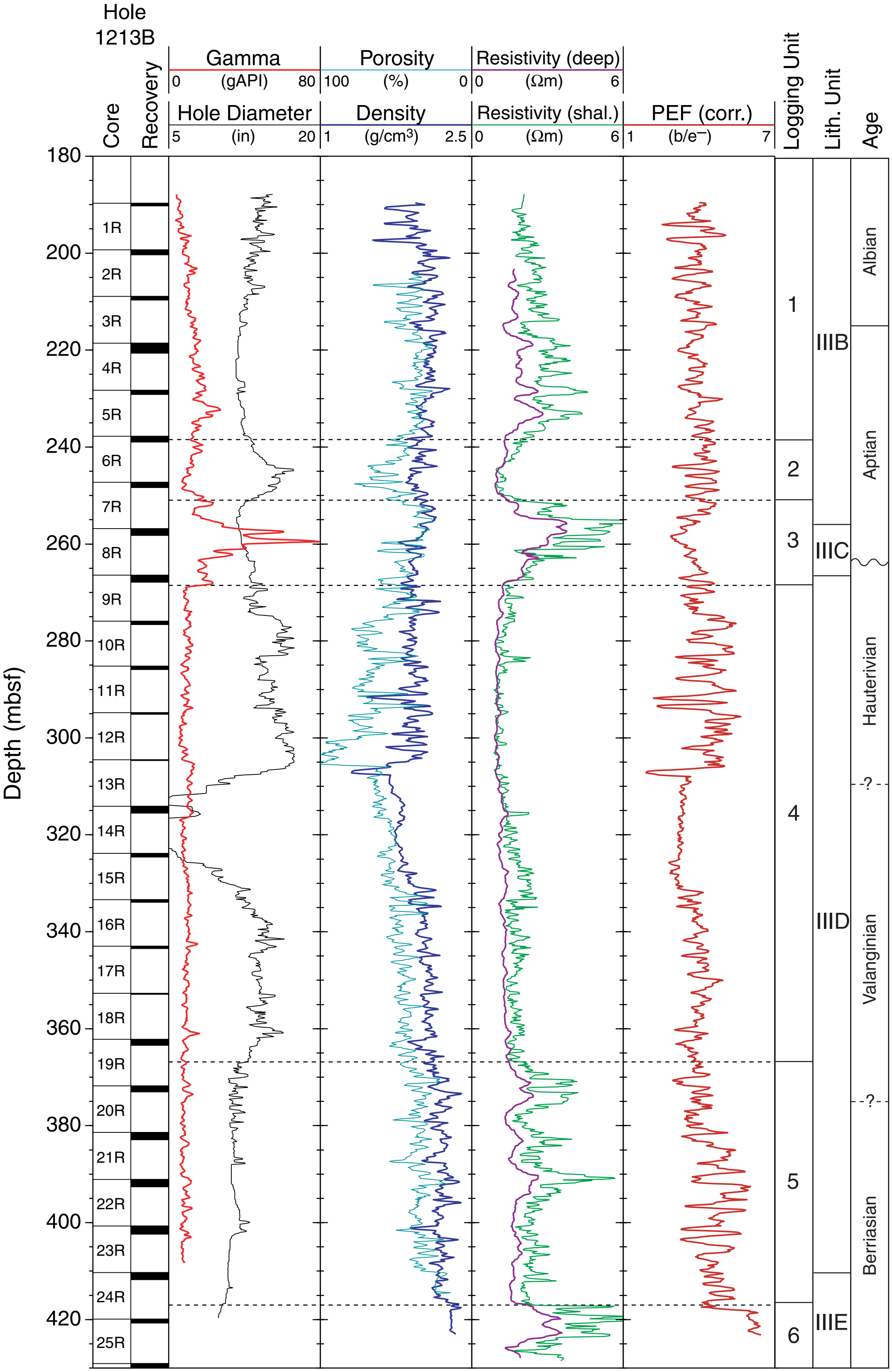

Figure F39. Geochemical logs in Hole 1213B. PEF (corr.) = photoelectric effect (corrected for porosity), lith. = lithologic.

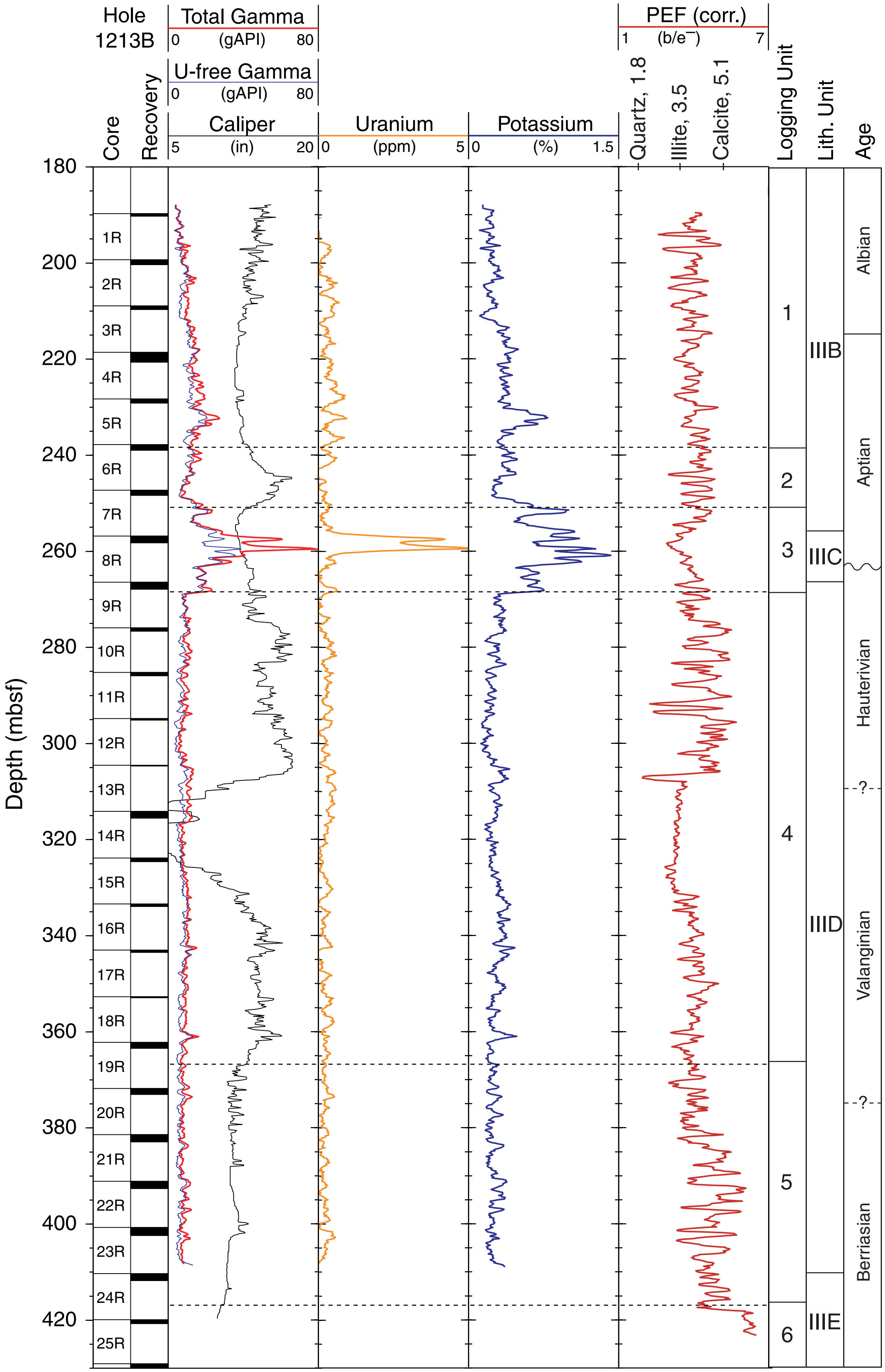

Figure F40. Gamma radiation and resistivity logs in the Aptian sediments from Holes 1213B and 1207B. Note the similar broad-scale resistivity pattern. Shall. = shallow.

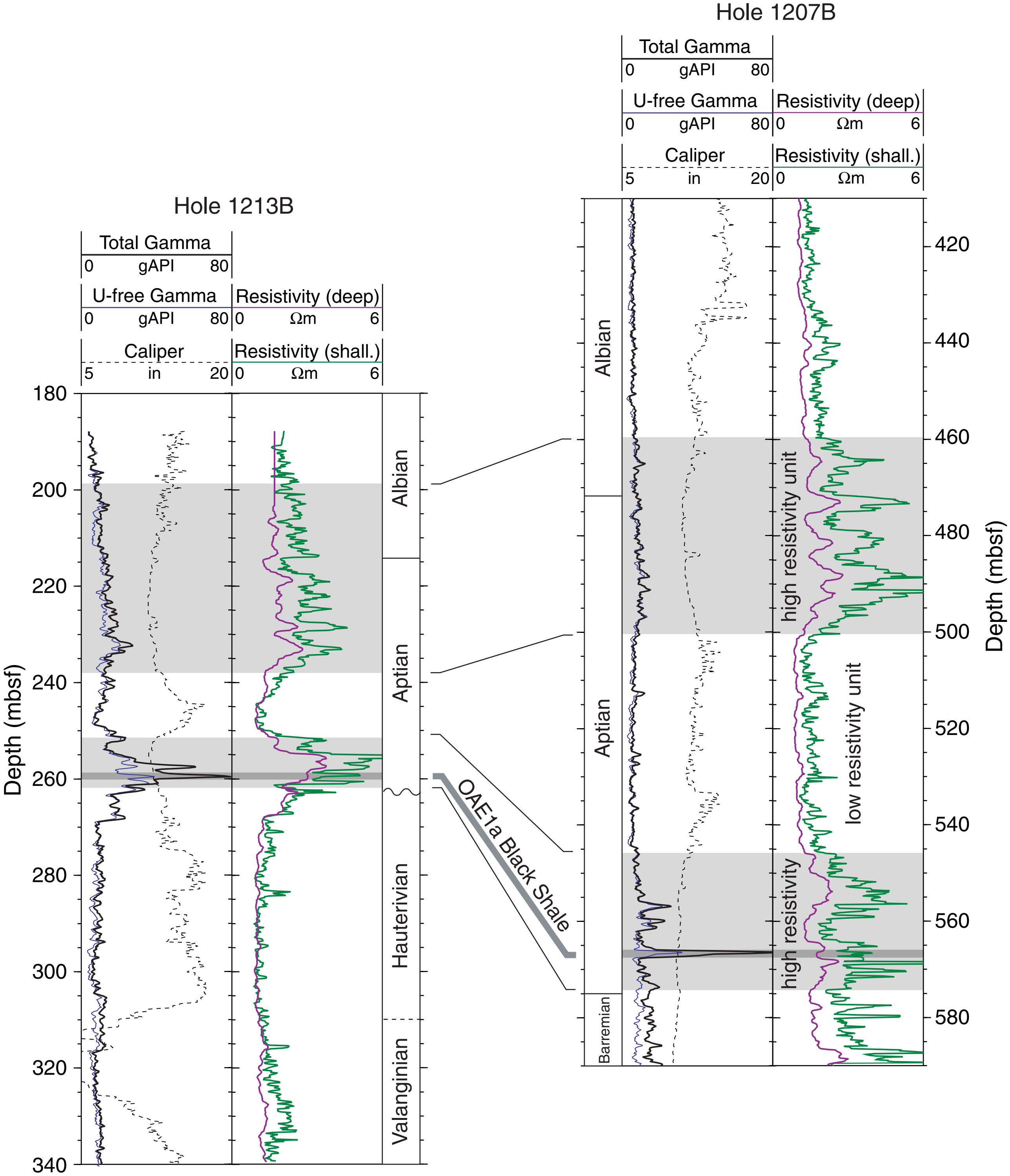

Figure F41. Detail of the gamma radiation, density, and porosity logs around the OAE1a black shale interval at 259.5 mbsf. HSGR = total spectral gamma ray, HCGR = computed gamma ray, HROM = high resolution bulk density, HALC = high resolution array porosity (limestone corrected).

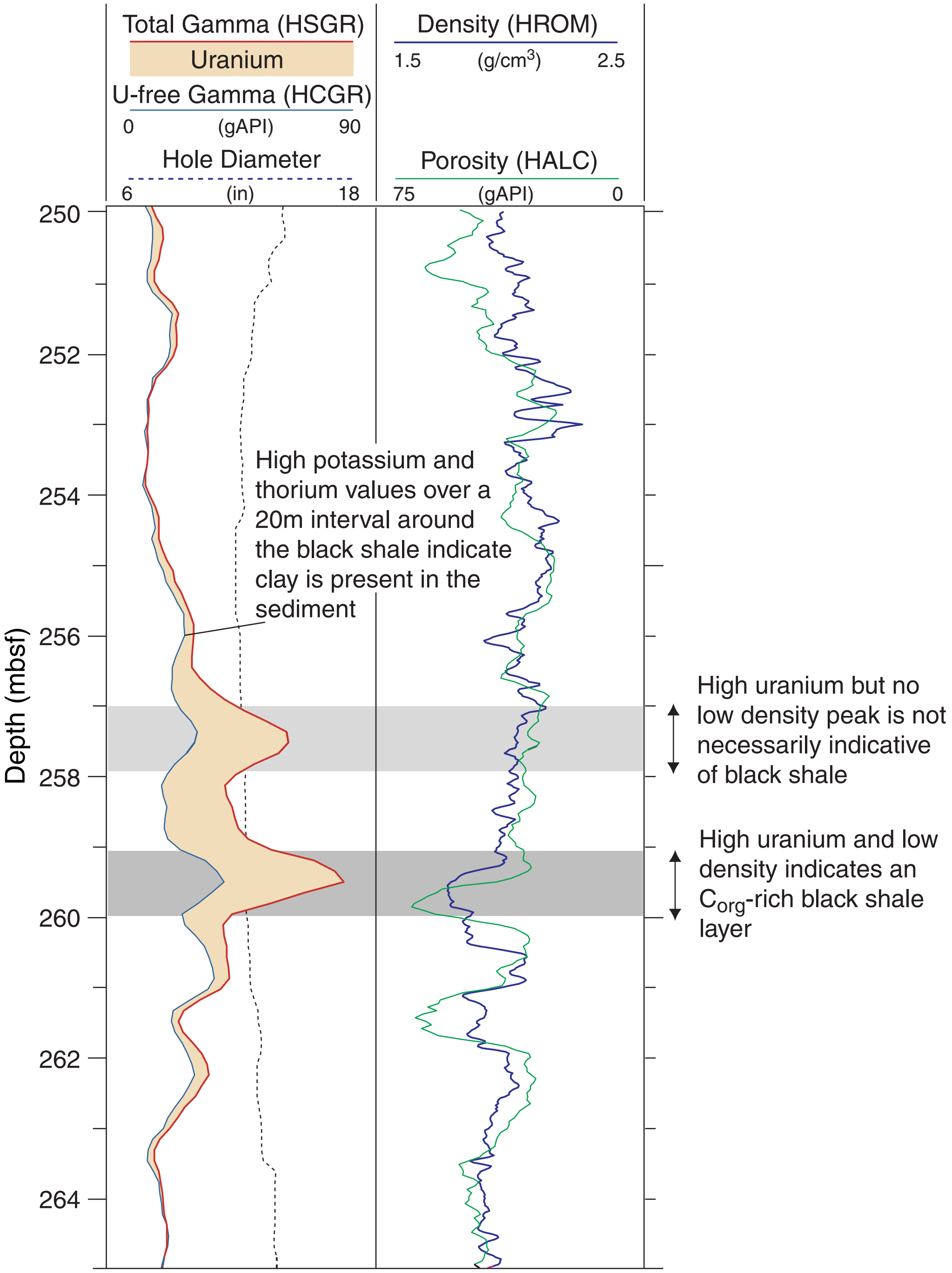

Table T1. Coring summary, Site 1213. (Continued on next page.)

Hole 1213A

Latitude: 31°34.6402′N
Longitude: 157°17.8605′ E
Time on site (hr): 181 (0600 hr, 2 Oct–1900 hr, 9 Oct 2001)
Time on hole (hr): 45 (0600 hr, 2 Oct–0300 hr, 4 Oct 2001)
Seafloor (drill pipe measurement from rig floor, mbrf): 3894.0
Distance between rig floor and sea level (m): 11.2
Water depth (drill pipe measurement from sea level, m): 3882.8
Total depth (drill pipe measurement from rig floor, mbrf): 4092.9
Total penetration (mbsf): 198.9
Total length of cored section (m): 198.9
Total core recovered (m): 43.09
Core recovery (%): 21.7
Total number of cores: 21
Total number of drilled intervals: 0

Hole 1213B

Latitude: 31°34.6576′N
Longitude: 157°17.8621′E
Time on hole (hr): 136 (0300 hr, 4 Oct–1900 hr, 9 Oct 2001)
Seafloor (drill pipe measurement from rig floor, mbrf): 3894.0
Distance between rig floor and sea level (m): 11.2
Water depth (drill pipe measurement from sea level, m): 3882.8
Total depth (drill pipe measurement from rig floor, mbrf): 4388.4
Total penetration (mbsf): 494.4
Total length of cored section (m): 304.7
Total core recovered (m): 60.46
Core recovery (%): 19.8
Total number of cores: 33
Total number of drilled intervals: 1

Core	Date (Oct 2001)	Local time (hr)	Depth (mbsf)		Length (m)		Recovery (%)
			Top	Bottom	Cored	Recovered	
198-1213A-							
1R	2	1510	0.0	8.4	8.4	8.43	100.4
2R	2	1640	8.4	18.1	9.7	4.56	47.0
3R	2	1728	18.1	27.5	9.4	9.55	101.6
4R	2	1820	27.5	37.1	9.6	2.45	25.5
5R	2	1905	37.1	46.7	9.6	2.59	27.0
6R	2	1955	46.7	56.4	9.7	6.27	64.6
7R	2	2100	56.4	66.1	9.7	1.14	11.8
8R	2	2155	66.1	75.8	9.7	0.25	2.6
9R	2	2305	75.8	85.4	9.6	0.20	2.1
10R	3	0010	85.4	95.0	9.6	0.18	1.9
11R	3	0110	95.0	104.6	9.6	0.14	1.5
12R	3	0230	104.6	114.3	9.7	0.91	9.4
13R	3	0340	114.3	123.9	9.6	0.69	7.2
14R	3	0500	123.9	133.4	9.5	1.10	11.6
15R	3	0640	133.4	143.1	9.7	0.87	9.0
16R	3	0800	143.1	150.7	7.6	1.14	15.0
17R	3	0922	150.7	160.3	9.6	1.12	11.7
18R	3	1020	160.3	170.0	9.7	0.45	4.6
19R	3	1115	170.0	179.6	9.6	0.24	2.5
20R	3	1210	179.6	189.3	9.7	0.34	3.5
21R	4	0230	189.3	198.9	9.6	0.47	4.9
			Cored totals:		198.9	43.09	21.7
198-1213B-							
		*****Drilled from 0.0 to 189.7 mbsf*****					
1R	4	2355	189.7	199.3	9.6	0.53	5.5
2R	5	0120	199.3	208.9	9.6	1.02	10.6
3R	5	0310	208.9	218.6	9.7	0.80	8.2
4R	5	0525	218.6	228.3	9.7	2.06	21.2
5R	5	0715	228.3	237.8	9.5	0.86	9.1
6R	5	0855	237.8	247.3	9.5	1.19	12.5
7R	5	1120	247.3	256.8	9.5	1.04	10.9
8R	5	1315	256.8	266.4	9.6	1.45	15.1
9R	5	1440	266.4	275.9	9.5	1.50	15.8
10R	5	1550	275.9	285.2	9.3	0.74	8.0
11R	5	1705	285.2	294.8	9.6	0.68	7.1

Table T1 (continued).

Core	Date (Oct 2001)	Local time (hr)	Depth (mbsf)		Length (m)		Recovery (%)
			Top	Bottom	Cored	Recovered	
12R	5	1810	294.8	304.5	9.7	0.30	3.1
13R	5	1915	304.5	314.1	9.6	0.19	2.0
14R	5	2035	314.1	323.8	9.7	1.40	14.4
15R	5	2200	323.8	333.4	9.6	0.80	8.3
16R	5	2340	333.4	343.0	9.6	0.50	5.2
17R	6	0105	343.0	352.7	9.7	0.47	4.8
18R	6	0220	352.7	362.2	9.5	0.22	2.3
19R	6	0455	362.2	371.8	9.6	1.25	13.0
20R	6	0645	371.8	381.4	9.6	1.24	12.9
21R	6	0840	381.4	391.1	9.7	1.50	15.5
22R	6	1010	391.1	400.7	9.6	1.50	15.6
23R	6	1200	400.7	410.3	9.6	1.70	17.7
24R	6	1400	410.3	419.9	9.6	1.45	15.1
25R	6	1515	419.9	429.1	9.2	0.80	8.7
26R	6	1650	429.1	438.6	9.5	0.85	8.9
27R	6	1845	438.6	447.8	9.2	1.00	10.9
28R	6	2330	447.8	452.8	5.0	4.10	82.0
29R	7	0345	452.8	457.4	4.6	0.71	15.4
30R	7	0840	457.4	467.0	9.6	5.00	52.1
31R	7	1550	467.0	476.6	9.6	10.19	106.1
32R	8	0225	476.6	485.7	9.1	6.21	68.2
33R	8	1515	485.7	494.4	8.7	7.21	82.9
				Cored totals:	304.7	60.46	19.8
				Drilled total:	189.7		
				Total:	494.4		

Table T2. Mineralogy and texture of diabase and basalt, estimated from thin section, Site 1213. (Continued on next page.)

Core, section, interval (cm)	Depth (mbsf)	Subunit	Name	Texture	Groundmass plagioclase		
					Percentage (%)	Size (mm)	Alteration
Igneous rocks:							
198-1213B-							
28R-1, 45–48	448.25	IVA	Diabase	Intersertal to intergranular to glomeroporphyritic	45	0.76^*, $0.29^\dagger$	To smectite along fractures (minor)
28R-3, 143–145	451.97	IVA	Diabase	Subophytic to intersertal	40	1.6^*, $0.6^\dagger$	
30R-2, 27–30	458.91	IVA	Diabase	Intergranular to intersertal to subophytic	45	1.8^*, $0.5^\dagger$	To smectite along fractures (minor)
30R-4, 39–41	461.94	IVA	Diabase (basalt?)	Intersertal to intergranular	45	1.6^*, $0.38^\dagger$	To smectite along fractures (minor)
31R-1, 7–10	467.07	IVB	Basalt	Seriate to slightly glomeroporphyritic	20	1.5^*, $0.29^\dagger$, some swallow-tail crystals	To smectite (moderate)
31R-3, 73–75	470.44	IVB	Diabase	Subophytic	48	1.5^*, $0.67^\dagger$	To smectite along fractures (minor)
32R-3, 72–75	480.26	IVB	Diabase	Subophytic to intergranular	50	1.4^*, $0.82^\dagger$ (some spherulites)	To smectite along fractures
33R-6, 106–108	492.79	IVC	Diabase	Intergranular (subophytic? prior to alteration)	45 (5% large phenocrysts)	0.5^*, $0.34^\dagger$ (some spherulites)	To smectite along cleavage and fractures (moderate)

Note: * = maximum, † = average.

Core, section, interval (cm)	Depth (mbsf)	Groundmass pyroxene			Groundmass olivine			Groundmass opaques	
		Percentage (%)	Size (mm)	Alteration	Percentage (%)	Size (mm)	Alteration	Percentage (%)	Size (mm)
Igneous rocks:									
198-1213B-									
28R-1, 45–48	448.25	7	$0.11^\dagger$		8	<0.67		10	$0.05^\dagger$
28R-3, 143–145	451.97	20	$0.2^\dagger$		10	$0.5^\dagger$	(Some inclusions)	10	$0.19^\dagger$
30R-2, 27–30	458.91	20	<0.57 (wide range)		5	<0.8 (wide range)	(Some inclusions)	10	$0.10^\dagger$
30R-4, 39–41	461.94	27	<0.6	To smectite (relict cleavage?)	3	<0.6	To smectite?	5	$0.08^\dagger$
31R-1, 7–10	467.07	2	$0.38^\dagger$	To smectite (relict cleavage?)	3	<0.67	(Some inclusions)	5	
31R-3, 73–75	470.44	2	$0.66^\dagger$	To clay + carbonate(?)	30	$0.66^\dagger$		10	$0.11^\dagger$
32R-3, 72–75	480.26	10	0.5^*, $0.29^\dagger$		2	0.5^*, $0.29^\dagger$		5	$0.17^\dagger$ (some skeletal)
		15	Pyroxene and olivine altered to smectite						
33R-6, 106–108	492.79	5	Remnants		?			5	$0.06^\dagger$ (some skeletal)
		35	Pyroxene and olivine(?) altered to smectite						

Table T2 (continued).

		Groundmass glass		Phenocrysts			
Core, section, interval (cm)	Depth (mbsf)	Percentage (%)	Alteration	Type	Veins	Vesicles	Glomerophenocrysts
Igneous rocks: 198-1213B-							
28R-1, 45–48	448.25	30	Devitrified, altered to smectite, altered to carbonate	None	Carbonate and green clay filled	None	Some
28R-3, 143–145	451.97	20	Devitrified, some fine plagioclase microlites	None	None	Amygdules or crystals altered to carbonate	None
30R-2, 27–30	458.91	30	Slightly devitrified (dark brown)		Brown clay filled	Plucked?	
30R-4, 39–41	461.94	20	Altered to clay and devitrified (dark brown)	None	None	None	None
31R-1, 7–10	467.07	70	Devitrified/altered fibrous bundles of microlites	Plagioclase	Smectite filled	>1-mm dark patches amygdules filled with smectite(?)	Some
31R-3, 73–75	470.44	5	Devitrified/altered		Carbonate, smectite, and quartz filled	None	Large (1.2 mm) composed of plagioclase crystals 2 mm and less + pyroxene + opaques
32R-3, 72–75	480.26	20	Devitrified/altered	None	None	None	None
33R-6, 106–108	492.79	5	Altered to clay minerals	Plagioclase (6.0–1.0 mm) severely altered to smectite and albite(?)	Carbonate and smectite filled		

Table T3. Mineralogy and lithology of metamorphosed sediment estimated from thin section.

Core, section, interval (cm)	Subunit	Name	Sericite	Volcanic glass	Groundmass quartz (and in burrows)	Phosphatic debris	Microfossils	Fe oxides	Dirty carbonate	Fibrous metamorphic mineral
Metamorphic rocks										
198-1213B-										
30R-4, 66–69	IVA/IVB	Meta-silicified shale (phyllite) with volcanic ash	55	10	30	Trace	Ghosts of radiolarians and foraminifers(?)	5		
32R-4, 71–74	IVB/IVC	Metachert			80		Ghosts of radiolarians and foraminifers(?)	10	5	5

Table T4. Downhole variation in colors of recovered chert.

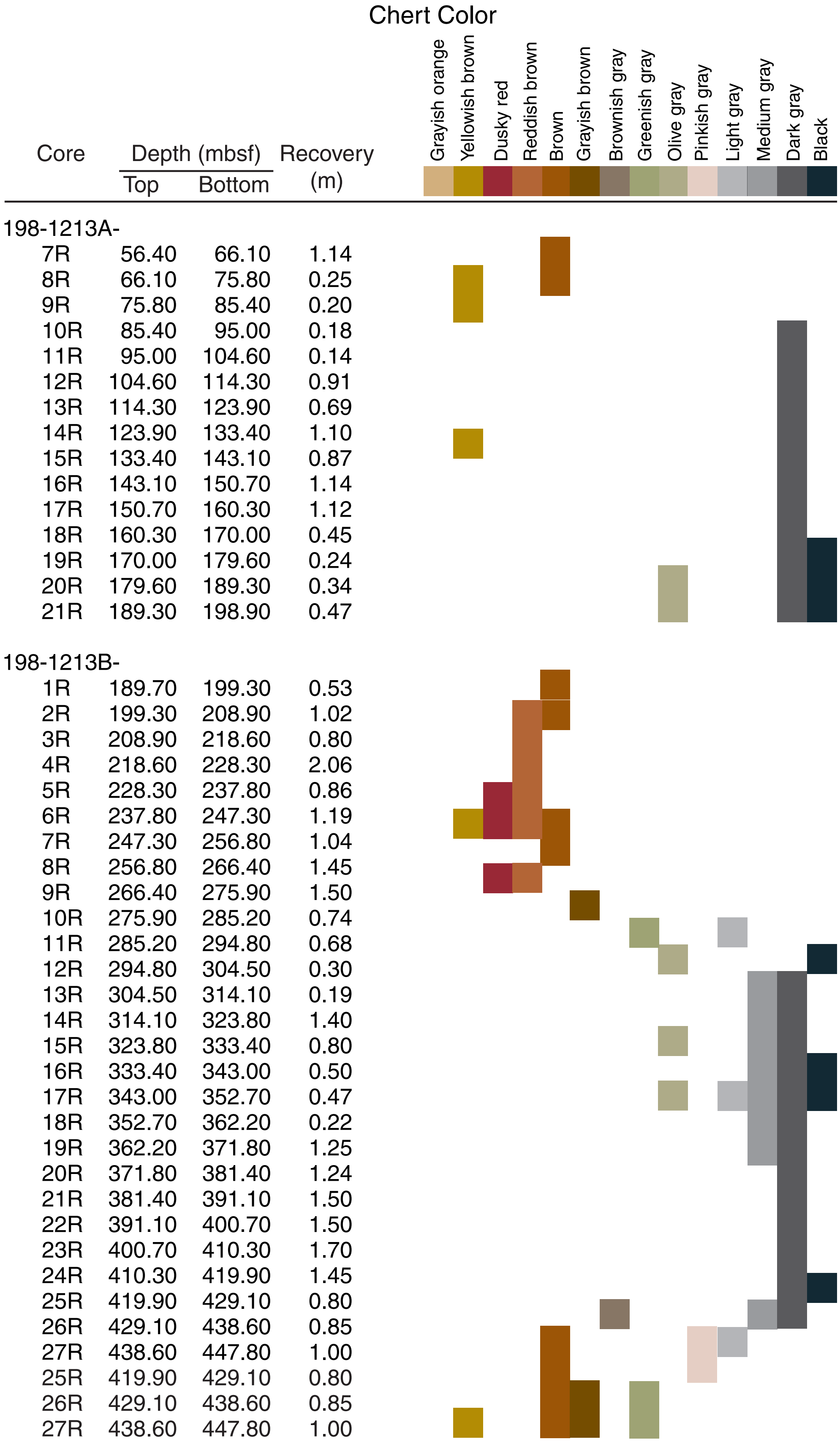

Core	Depth (mbsf)		Recovery	Chert Color													
	Top	Bottom	(m)	Grayish orange	Yellowish brown	Dusky red	Reddish brown	Brown	Grayish brown	Brownish gray	Greenish gray	Olive gray	Pinkish gray	Light gray	Medium gray	Dark gray	Black
198-1213A-																	
7R	56.40	66.10	1.14					■									
8R	66.10	75.80	0.25		■			■									
9R	75.80	85.40	0.20		■												
10R	85.40	95.00	0.18													■	
11R	95.00	104.60	0.14													■	
12R	104.60	114.30	0.91													■	
13R	114.30	123.90	0.69													■	
14R	123.90	133.40	1.10		■											■	
15R	133.40	143.10	0.87													■	
16R	143.10	150.70	1.14													■	
17R	150.70	160.30	1.12													■	
18R	160.30	170.00	0.45													■	■
19R	170.00	179.60	0.24													■	■
20R	179.60	189.30	0.34									■				■	■
21R	189.30	198.90	0.47									■				■	■
198-1213B-																	
1R	189.70	199.30	0.53					■									
2R	199.30	208.90	1.02				■	■									
3R	208.90	218.60	0.80				■										
4R	218.60	228.30	2.06				■										
5R	228.30	237.80	0.86			■	■										
6R	237.80	247.30	1.19		■	■	■	■									
7R	247.30	256.80	1.04					■									
8R	256.80	266.40	1.45			■	■										
9R	266.40	275.90	1.50						■								
10R	275.90	285.20	0.74								■			■			
11R	285.20	294.80	0.68									■					■
12R	294.80	304.50	0.30												■	■	
13R	304.50	314.10	0.19												■	■	
14R	314.10	323.80	1.40												■	■	
15R	323.80	333.40	0.80									■			■	■	
16R	333.40	343.00	0.50												■	■	■
17R	343.00	352.70	0.47									■		■	■	■	■
18R	352.70	362.20	0.22												■	■	
19R	362.20	371.80	1.25												■	■	
20R	371.80	381.40	1.24													■	
21R	381.40	391.10	1.50													■	
22R	391.10	400.70	1.50													■	
23R	400.70	410.30	1.70													■	
24R	410.30	419.90	1.45													■	
25R	419.90	429.10	0.80													■	■
26R	429.10	438.60	0.85							■					■	■	
27R	438.60	447.80	1.00					■					■	■			
25R	419.90	429.10	0.80					■					■				
26R	429.10	438.60	0.85					■	■		■						
27R	438.60	447.80	1.00		■			■	■		■						

Table T5. Calcareous nannofossil datums, ages, and depths, Site 1213.

Datum	Zone/ Subzone (base)	Core, section, interval (cm)	Depth (mbsf)	Core, section, interval (cm)	Depth (mbsf)	Age (Ma)
		198-1213A-		198-1213B-		
LO *Pseudoemiliania lacunosa*	CN14b	2R-1, 45	8.85		8.38	0.46
FO *Gephyrocapsa parallela*	CN14a	2R-1, 45	8.85		11.85	0.95
FO *Gephyrocapsa caribbeanica*	CN13b	4R-1, 45	27.95		29.45	1.73
LO *Discoaster brouweri*	CN13a	4R-2, 45	29.45		27.95	1.95
LO *Discoaster pentaradiatus*	CN12d	5R-2, 45	39.05		37.55	2.52
LO *Discoaster surculus*	CN12c	5R-2, 45	39.05		37.55	2.63
LO *Reticulofenestra pseudoumbilicus*	CN12a	6R-1, 15	48.15		39.62	3.82
LO *Amaurolithus* spp.	CN11	6R-1, 15	48.15		39.62	4.56
FO *Ceratolithus rugosus*	CN10c	6R-3, 94	50.64		52.92	5.07
FO *Amaurolithus* spp.	CN9b	6R-3, 94	50.64		52.92	7.39
FO *Lithastrinus grillii*	CC15	7R-1, 43	56.43		57.53	85.5
FO *Lithraphidites acutus*	UC3	8R-CC	66.34		76.04	96.8
FO *Eiffellithus turriseiffelii*	NC10c	19R-CC	170.13		179.61	101.7
FO *Tranolithus orionatus*	NC8c	21R-CC	189.30		190.12	107.3
FO *Prediscosphaera columnata*	NC8a			3R-1, 14	209.04	112.6
FO *Rhagodiscus achlyostaurion*	NC7c			5R-1, 2	228.32	115.2
FO *Eprolithus floralis*	NC7a			8R-1, 3	256.83	119.0
LO *Cruciellipsis cuvillieri*	NC5a			9R-1, 47	266.87	128.3
FO *Eiffellithus windii*				14R-1, 48	314.58	134.2
LO *Rucinolithus wisei*	NK3b			14R-1, 12	314.22	134.9
LO *Umbria granulosa*				21R-1, 150	382.90	137.0
FO *Diadorhombus rectus*				25R-1, 45	420.35	139.0
FO *Cretarhabdus octofenestratus*	NKJ–D			26R-1, 15	429.25	141.5
FO *Rotelapillus laffittei*	NKJ–C			27R-1, 38	438.38	142.3

Note: FO = first occurrence, LO = last occurrence.

Table T6. Planktonic foraminiferal datums, ages, and depths, Site 1213.

Datum	Zone (base)	Core, section, interval (cm)	Depth (mbsf)	Core, section, interval (cm)	Depth (mbsf)	Age (Ma)
		198-1213A-		198-1213B-		
FO *Truncorotalia truncatulinoides*	N22	2R-CC	12.91			1.92
LO *Sphaeroidinellopsis seminulina*		4R-CC	29.90			3.11
FO *Truncorotalia tosaensis*	N21	4R-CC	29.90			3.35
FO *Globorotalia puncticulata*		5R-CC	39.62			4.50
FO *Globorotalia tumida*	N18	5R-CC	39.62			5.82
LO *Costellagerina libyca*		9R-CC	76.04			98.5
FO *Rotalipora globotruncanoides*	KS17	10R-CC	85.43			99.1
FO *Planomalina buxtorfi*		15R-1, 6–8	133.46			100.2
FO *Rotalipora appenninica*	KS16	15R-1, 6–8	133.46			100.4
FO *Biticinella breggiensis*	KS14			2R-1, 33–35	199.63	105.0
FO *Ticinella primula*	KS13			3R-1, 14–15	209.04	109.5
FO *Hedbergella trocoidea*				6R-1, 83–84	238.63	116.7
Base of Selli event				8R-1, 56	257.36	119.2
FO *Globigerinelloides* sp.				9R-1, 17–18	266.57	131.9

Notes: FO = first occurrence, LO = last occurrence.

Table T7. Distribution of Cenozoic and Cretaceous benthic foraminifers, Hole 1213A.

Core, section, interval (cm)	Depth (mbsf)	Nannofossil zone/ subzone	Size fraction (µm)	Preservation	Benthic abundance	*Dentalina* spp.	*Pleurostomella* spp.	*Chrysalogonium longicostatum*	*Anomalinoides globulosus*	*Pullenia bulloides*	*Melonis barleeanus*	*Cibicidoides* spp.	*Cibicidoides wuellerstorfi*	*Oridorsalis tener*	*Cibicidoides bradyi*	*Cibicidoides subhaidingeri*	*Globocassidulina* sp.	*Gyroidinoides* spp.	*Cibicidoides mundulus*	*Pyrgo lucernula*	*Pyrgo murrhina*	*Uvigerina hispida*	*Uvigerina hispidocostata*	*Uvigerina senticosa*	*Uvigerina peregrina*	*Eggerella bradyi*	*Martinottiella* sp.	*Karreriella bradyi*	*Haplophragmoides* spp.
198-1213A-																													
1R-CC	8.38	CN14b	>250	G	C				R	R	R	T	R	C				R	R	R	F	A	A		R	R	R	T	T
3R-CC	27.60	CN13b–14a	>250	G	F					T		T	T	F	R	T	R	R	T	T	R	R	F	A	R	R		T	T
5R-CC	39.62	CN10a	>250	G	R	R	T	R	R	T	T	R	R	F						R	R	T	R			F	R		

Core, section, interval (cm)	Depth (mbsf)	Nannofossil zone/ subzone	Size fraction (µm)	Preservation	Benthic abundance	*Protosangularia cenomaniana*	*Gyroidinoides infracretaceus*	*Protosangularia albiana*	*Hanzawaia compressa*	*Conorotalites aptiensis*	*Gyroidinoides globosus*	*Lenticulina* spp.	*Marginulinopsis* spp.	*Pleurostomella* spp.	*Ramulina tappanae*	*Bulimina* spp.	*Dentalina* spp.	*Ellipsoidella* spp.	*Aragonia ouezzanensis*	*Nodosarella subnodosa*	*Nodosaria* spp.	*Oridorsalis umbonatus*	*Ramulina tetrahedralis*	*Dorothia gradata*	*Gaudryina dividens*	*Rhizammina* spp.	*Heterantyx cretosa*	*Tritaxia gaultina*	*Spiroplectinella excolata*	*Gaudryina pyramidata*	*Tristix* spp.
198-1213A-																															
7R-CC	57.53	CC14–16	>125	M	C						R					R	R	R	C	R	R	R	T							A	T
9R-CC	76.04	NC10a	>125	M	R		R	R	R	R							R												T		
21R-1, 0–1	189.30	NC8c–9a	>125	M	F	F	F	C				F	T	T	R	R								T	R	T	T	C			

Notes: Preservation: G = good, M = moderate. Abundance: A = abundant, C = common, F = few, R = rare, T = trace.

Table T8. Distribution of Cretaceous benthic foraminifers, Hole 1213B.

						Trochospiral						Other calcareous																		Agglutinated								
Core, section, interval (cm)	Depth (mbsf)	Nannofossil zone/ subzone	Size fraction (µm)	Preservation	Benthic abundance	*Gavelinella* spp.	*Hanzawaia* sp.	*Protosangularia albiana*	*Gyroidinoides globosus*	*Gyroidinoides infracretaceus*	*Protosangularia cenomaniana*	*Dentalina* spp.	*Lenticulina* spp.	*Ramulina tetrahedralis*	*Ramulina tappanae*	*Saracenaria* spp.	*Globulina* spp.	*Vaginulinopsis* spp.	*Lingulina loryi*	*Oolina globosa*	*Nodosaria* spp.	*Marginulinopsis* spp.	*Psilocitharella* spp.	*Frondicularia bettenstaedti*	*Astacolus* spp.	*Saracenaria triangularis*	*Buliminella* sp.	*Pleurostomella* spp.	*Marssonella praeoxycona*	*Dorothia praehauteriviana*	*Dorothia gradata*	*Spirillina* spp.	*Gaudryina dividens*	*Dorothia conula*	*Remesella* sp.	*Tritaxia gaultina*	*Pseudoclavulina* spp.
198-1213B-																																					
2R-1, 4–6	199.34	NC8a	>125	M	R			R		R	F	R					R														R		F	R	F		T
3R-1, 14–15	209.04	NC8a	>125	M	F			A		C	F	R	R			T										T							F	F	R	F	
5R-1, 0–2	228.30	NC7c	>125	P	T					T	T																						R	R		R	
6R-1, 83–84	238.63	NC7a-b	>125	M	F		R	R	C	A	F	F	R		T		T				R				R			T			R		C	C	F		
9R-1, 9–12	266.49	NC5/BC15	>125	M	R	T	C	T				T	R				R			T				T	R	T	A			C		T					
9R-1, 70–71	267.10	NC4	>125	M	A							R	F				T	T	R	T			T	T		T	R		F	R	R						
12R-1, 9–12	294.89	NC4	>125	P	R							R	R					R					T	R		T			C	F							
14R-1, 140–150	314.27	u. NK3a	>125	P–M	R							R	F				R					R	T			R			A	R							
16R-1, 12–14	333.52	NK2	>125	M	F							R	A	R				T				T		T	T				R								
19R-1,119–122	363.39	NK1	>125	P	R							R	R			R	R						T						A								
20R-1, 31–33	372.13	NK1	>125	P	T							R	R					T																			
21R-1, 148–150	382.88	NJK–D	>125	P	R							R	F		R							T															
23R-1, 20–21	400.90	NJK–D	>125	M	R							F	F			R	R	R	T		T																
24R-1, 38–39	410.68	NJK–D	>125	P	R							R	R	T	T	T	T																				
25R-1, 29–49	420.19	NJK–D	>125	P	R							R	R																								

Notes: Preservation: M = moderate, P = poor. Abundance: A = abundant, C = common, F = few, R = rare, T = trace.

Table T9. Concentrations of CH_4 in headspace gas, Hole 1213A.

Core, section, interval (cm)	Depth (mbsf)	CH_4 (ppmv)
198-1213A-		
1R-5, 0–5	6.0	2.1
2R-3, 0–5	11.4	2.1
3R-5, 0–5	24.1	2.0
5R-2, 0–5	38.6	1.8
6R-4, 0–5	51.2	1.9

Table T10. Carbonate content, Site 1213.

Core, section, interval (cm)	Depth (mbsf)	Total inorganic carbon (wt%)	$CaCO_3$ (wt%)
198-1213A-			
1R-2, 84–85	2.34	9.6	79.6
1R-3, 125–126	4.25	8.7	72.1
1R-5, 89–90	6.89	2.4	20.0
2R-1, 130–131	9.70	5.6	46.2
2R-2, 9–10	9.99	8.6	72.0
2R-3, 67–68	12.07	4.8	40.3
3R-1, 97–98	19.07	8.7	72.3
3R-3, 117–118	22.27	4.8	40.0
3R-5, 58–59	24.68	4.6	38.5
4R-1, 107–108	28.57	9.4	78.1
4R-2, 20–21	29.20	4.9	40.6
5R-1, 36–37	37.46	9.3	77.1
5R-2, 29–30	38.89	4.3	35.6
5R-2, 60–61	39.20	1.4	11.4
198-1213B-			
8R-1, 47–48	257.27	0.1	0.5
8R-1, 63–64	257.43	0.1	0.8
8R-1, 96–97	257.76	0.1	0.4
11R-1, 61–62	285.81	8.2	67.9
14R-1, 29–30	314.39	9.9	82.6
15R-1, 9–10	323.89	5.9	49.1
19R-1, 10–11	362.30	11.0	92.0
19R-1, 110–111	363.30	6.7	56.1
19R-1, 112–113	363.32	7.3	60.6
20R-1, 31–32	372.11	7.0	58.1
20R-1, 67–68	372.47	9.9	82.2
21R-1, 29–30	381.69	10.1	83.7
22R-1, 24–25	391.34	11.6	96.5
22R-1, 116–117	392.26	9.5	78.8
26R-1, 16–17	429.26	8.0	66.5
27R-1, 24–25	438.84	4.1	34.2

Table T11. Results from Shatsky Rise (Southern High) CNSH analysis of samples from OAE1a.

Core, section, interval (cm)	Depth (mbsf)	Organic carbon (wt%)	Nitrogen (wt%)	Sulfur (wt%)	Hydrogen (wt%)	C/N ratio (atomic)
198-1213B-						
8R-1, 47–48	257.27	10.23	0.37	2.00	1.72	23.6
8R-1, 63–64	257.43	25.20	0.83	4.36	2.92	25.9
8R-1, 96–97	257.76	2.87	0.14	0.76	1.02	17.2
11R-1, 61–62	285.81	0.41	0.05	0.31	0.30	7.0
15R-1, 9–10	353.89	2.54	0.12	2.86	0.45	17.9
19R-1, 112–113	363.32	3.13	0.18	5.18	0.51	14.9
20R-1, 31–32	372.11	0.11	0.03	0.69	0.23	3.1
21R-1, 29–30	381.69	0.03	0.01	0.24	0.16	4.3
26R-1, 16–17	429.26	0.00	0.01	0.06	0.41	NA

Note: NA = not applicable.

Table T12. Organic carbon contents and results from Rock-Eval pyrolysis.

Core, section, interval (cm)	Depth (mbsf)	TOC (wt%)	S_1 (mg/g)	S_2 (mg/g)	S_3 (mg/g)	T_{max} (°C)	PI (S_1/S_2)	HI (mg HC/g TOC)	OI (mg CO_2/g TOC)
Shatsky Rise (Southern High):									
198-1213B-									
8R-1, 47–48	257.27	10.23	2.54	51.30	2.14	418	0.05	501	20
8R-1, 63–64	257.43	25.20	6.97	127.59	5.87	404	0.05	506	23
8R-1, 96–97	257.76	2.87	0.39	10.49	6.08	422	0.04	365	211
11R-1, 61–62	285.81	0.41	0.05	0.96	10.27	427	0.05	234	2504*
15R-1, 9–10	323.89	2.54	0.19	10.30	12.13	424	0.02	405	477*
19R-1, 112–113	363.32	3.13	0.15	12.62	13.96	426	0.01	403	446*

Notes: TOC = total organic carbon. S_1 and S_2 = peaks corresponding to free and kerogen-bound HC, respectively, generated by Rock-Eval pyrolysis; S_3 = amount of CO_2 released by thermal cracking of kerogen. T_{max} = peak temperature of kerogen breakdown. PI = production index. HI = hydrogen index, HC = hydrocarbon. OI = oxygen index. * = values enhanced by carbonate contents (cf. Table T10, p. 101).

Table T13. Dominant biomarkers and compound ratios in organic-rich samples, Hole 1213B.

Biomarker feature	Core, section, interval (cm)				
	198-1213B-				
	8R-1, 47–48	8R-1, 63–64	8R-1, 96–97	15R-1, 9–10	19R-1, 112–113
Dominant hydrocarbons:					
Dominant component	$C_{31}\beta\beta$ H	$C_{31}\beta\beta$ H	$C_{31}\beta\beta$ H	$C_{29}\ \Delta^{17(21)}$ H	$C_{29}\ \Delta^{17(21)}$ H
n-alkane	C_{15}	C_{15}	C_{17}	C_{17}	C_{16}/C_{26}
Branched alkane	13-ME C_{15}	13-ME C_{15}	13-ME C_{15}	13-ME C_{15}	13-ME C_{15}
Acyclic isoprenoid	C_{16}	C_{16}	C_{16}	PR	PR
Sterene	$C_{29}\ \Delta^4$	$C_{29}\ \Delta^4$	$C_{29}\ \Delta^4$	$C_{29}\ \Delta^4$	$C_{29}\ \Delta^4$
Hopane	$C_{31}\beta\beta$	$C_{31}\beta\beta$	$C_{31}\beta\beta$	$C_{31}\beta\beta$	$C_{31}\beta\beta$
Hopene	$C_{30}\ \Delta^{17(21)}$	$C_{29}\ \Delta^{17(21)}$	$C_{30}\ \Delta^{17(21)}$	$C_{29}\ \Delta^{17(21)}$	$C_{29}\ \Delta^{17(21)}$
Methylhopane	ME $C_{34}\beta\beta$	NA	ME $C_{28}\ \Delta^{17(21)}$	NA	NA
Compound distributions:					
13-ME C_{15}/C_{15}	0.08	0.10	0.85	0.38	0.92
PR/PH	0.46	0.27	0.32	2.8	2.3
C_{27}:C_{28}:C_{29} in Δ^4-sterenes	30:18:52	27:18:55	33:17:50	37:5:58	36:13:51
C_{30}:C_{31}:C_{32}:C_{33} in $\beta\beta$ hopanes	13:65:14:8	18:73:8:1	9:83:7:1	18:77:5:0	10:78:10:1
C_{27}:C_{29}:C_{30}:C_{31} in $\Delta^{17(21)}$-hopenes	36:26:29:9	34:34:28:5	26:18:43:13	23:61:13:2	26:53:13:2
ME $\beta\beta$ H/H $\beta\beta$ H (C No.)	1.2 (C_{33}/C_{32})	NA	0.5 (C_{32}/C_{31})	NA	NA
$C_{29}\ \Delta^{4,22}/C_{29}\ \Delta^4$	0.30	0.27	0.44	0.34	0.52
$C_{29}\ \Delta^4/C_{31}\beta\beta$ H	0.33	0.50	0.22	0.54	0.39
Dominant ketones and tocopherol:					
Alkadienone	NA	NA	$C_{38:2}$ ET	NA	NA
Acyclic isoprenoid	C_{18}	C_{18}	C_{18}	C_{18}	C_{18}
Stanone	$C_{29}5\alpha$(H)	$C_{29}5\alpha$(H)	$C_{29}5\alpha$(H)	$C_{29}5\alpha$(H)	$C_{27}5\alpha$(H)
Stenone	$C_{29}\ \Delta^4$	$C_{29}\ \Delta^4$	$C_{29}\ \Delta^4$	$C_{29}\ \Delta^4$	$C_{27}\ \Delta^4$
Hopanone	$C_{31}\beta\beta$	$C_{33}\beta\beta$	$C_{31}\beta\beta$	$C^{30}\beta\beta$	$C_{30}\beta\beta$
Methylhopanone	ME $C_{34}\ \beta\beta$	ME $C_{34}\ \beta\beta$	ME $C_{34}\ \beta\beta$	NA	NA
Major tocopherol	α-T	α-T	α-T	α-T	α-T
Compound distributions:					
C_{27}:C_{28}:C_{29} in 5α stanones	41:11:48	37:9:54	45:8:47	35:7:58	53:6:41
C_{27}:C_{28}:C_{29} in Δ^4-stenones	41:11:48	35:9:56	32:8:60	35:5:60	51:6:43
C_{28}:C_{29}:C_{30} in 4-methylstanones	26:37:37	22:39:39	25:40:35	27:44:29	23:49:28
$C_{29}\ \Delta^4$ S/$C_{29}\ 5\alpha$ S	1.7	3.7	0.79	0.78	0.40
$C_{29}5\alpha$ S/4-ME C_{29} S	3.0	4.2	3.1	2.4	1.5
ME $C_{34}\beta\beta$ H/ $C_{33}\beta\beta$ H	0.81	0.31	0.47	NA	NA

Notes: NA = not applicable because of absence of methylhopanes or methylhopanones, and of alkenones in specific samples. Compound codes are described in Tables T15, p. 106, and T16, p. 107. Compound ratios and carbon number distributions are based on intensities in total ion chromatograms, except for steroidal and $\Delta^{17(21)}$-hopene carbon number ratios, which are based on distributions in diagnostic mass chromatograms.

Table T14. Biomarker carbon number ranges and relative abundances in samples from Hole 1213B and their putative biological source(s) and process of formation with references.

Biomarker class components (code)	Range	Relative abundance					Putative biological source(s)/process of formation	References
		8R-1, 47 cm	8R-1, 63 cm	8R-1, 96 cm	15R-1, 9 cm	19R-1, 112 cm		
n-Alkyl compounds:								
Lower alkanes with OEP	C_{13}–C_{19}	+++	+++	++	++	+++	Algae, bacteria, cyanobacteria	Han et al., 1968; Gelpi et al., 1970; Brassell et al., 1978
Higher alkanes with OEP	C_{23}–C_{33}	++	++	+	+	ND	Vascular plants	Eglinton and Hamilton, 1963; Simoneit, 1978
Branched compounds:								
Monomethylalkanes (MA)	C_{14}–C_{17}	+	+	++	+	++	Bacteria, cyanobacteria	Shiea et al., 1990; Dachs et al., 1998; Köster et al., 1999
Acyclic isoprenoids:								
TMTD, TMPD	C_{16}, C_{18}	+++	+++	++	++	++	Photoautotrophs	Didyk et al., 1978; Volkman and Maxwell, 1986
Pristane (PR)	C_{19}	++	+	+	+	++	Photoautotrophs	Didyk et al., 1978; Goossens et al., 1984
Phytane (PH)	C_{20}	+++	++	++	+	+	Photoautotrophs, methanogens	Didyk et al., 1978; Brassell et al., 1981
Hexamethyltetracosane (HMTC)	C_{20}	++	ND	++	ND	ND	Methanogenic bacteria	
Steroids:								
Δ^4- and Δ^5-sterenes	C_{27}–C_{29}	+++	+++	+++	+++	+++	Eukaryotes/sterol dehydration	Mackenzie et al., 1982; Peakman and Maxwell, 1988
$\Delta^{4,22}$- and $\Delta^{5,22}$-steradienes	C_{29}	++	++	++	+++	+	Eukaryotes/sterol dehydration	Rullkötter et al., 1984; Farrimond et al., 1986b
$\Delta^{3,5}$- steradienes	C_{27}–C_{29}	ND	+	ND	ND	ND	Eukaryotes/sterene rearrangement	Brassell et al., 1984; Peakman and Maxwell, 1988
A-ring monoaromatic	C_{27}–C_{29}	+	++	+	++	+	Eukaryotes/sterol aromatization	Hussler et al., 1981; Brassell et al., 1984
B-ring monoaromatic anthra-	C_{27}–C_{29}	+	+	+	ND	ND	Eukaryotes/sterol aromatization	Hussler and Albrecht, 1983; Rullkötter and Welte, 1983
Triterpenoids:								
17β(H),21β(H)-hopanes	C_{27}, C_{29}–C_{31}	+++	+++	+++	+++	+++	Prokaryotes	Ourisson et al., 1979, 1987; Rohmer et al., 1992
17α(H),21β(H)-hopanes	C_{27}, C_{29}–C_{31}	++	++	++	+	+	Prokaryotes	Ourisson et al., 1979, 1987; Rohmer et al., 1992
17β(H),21β(H)-methylhopanes	C_{30}–C_{33}	++	ND	++	ND	ND	Cyanobacteria, methylotrophs	Ourisson et al., 1987; Summons and Jahnke, 1990
Hopanes > C_{32}	C_{33}	+++	+	+	ND	ND	Bacteria, methylotrophs	Ourisson et al., 1979, 1987; Rohmer et al., 1992
Hop-17(21)-enes	C_{27}, C_{29}–C_{31}	+++	++	++	+++	++	Bacteria, anaerobic phototrophs	Brassell and Eglinton, 1983; Rohmer et al., 1984
Methylhopenes	C_{27}	++	ND	++	ND	ND	Cyanobacteria, methylotrophs	Ourisson et al., 1987; Summons and Jahnke, 1990
Aromatic hopanoid	C_{27}	ND	+	+	ND	ND	bacteria/aromatization	Greiner et al., 1976, 1977
Neohop-13(18)-enes	C_{27}, C_{29}, C_3	++	++	++	ND	+	Bacteria, anaerobic phototrophs	Brassell and Eglinton, 1983; Howard et al., 1984
Fernenes	C_{30}	++	++	+	+++	++	Bacteria, anaerobic phototrophs	Brassell and Eglinton, 1983; Howard et al., 1984
triterpene (dammaradiene?)C_{30}		ND	+++	ND	ND	++	Bacteria?	Brassell, 1984; Rullkötter et al., 1984
Ketones and ethers:								
Alkan-2-ones	C_{13}–C_{23}	+	+	+	+	+	Algae, bacteria/oxidation	Brassell et al., 1980
Alkadienones	C_{37}–C_{39}	ND	ND	++	ND	ND	Haptophyte algae	Brassell et al., 1986; Farrimond et al., 1986b; Marlowe et al., 1990
TMTD-2-one	C_{18}	+	++	+	+	+	Photoautotrophs; oxidation	Simoneit, 1973
5α(H)- and 5β(H)-stanones	C_{27}–C_{29}	+++	+++	+++	+++	+++	Eukaryotes/sterol oxidation	Gagosian and Smith, 1979; Robinson et al., 1984
4-methylstanones	C_{28}–C_{30}	++	+	++	++	+++	Dinoflagellates	Gagosian and Smith, 1979; Robinson et al., 1984
Δ^4-stenones	C_{27}–C_{29}	++	++	+++	++	++	Eukaryotes/sterol oxidation	Edmunds et al., 1980; Brassell et al., 1987
$\Delta^{4,22}$-stenones	C_{27}–C_{29}	++	+++	++.	++	++	Eukaryotes/sterol oxidation	Edmunds et al., 1980; Brassell et al., 1987
4-methyl-Δ^{22}-sterones	C_{28}–C_{31}	+	+	+	+	++	Dinoflagellates	Gagosian and Smith, 1979; Robinson et al., 1984
Hopanones	C_{27}, C_{29}–C_{31}	++	++	NA	++	++	Bacteria, algae/predation, oxidation	Dastillung et al., 1980
Methylhopanones	C_{30}–C_{33}	++	+	++	ND	ND	Bacteria, algae/predation, oxidation	Dastillung et al., 1980
Methylmethylhopanyl ether	C_{32}	++	+	+++	ND	ND	Bacteria	Dastillung et al., 1980; Rohmer et al., 1992
Other biomarkers:								
α-, β-, γ-, δ-tocopherols	C_{27}–C_{29}	++	++	++	+	+	Photoautotrophs	Brassell et al., 1983; Goossens et al., 1984
Sterol ethers	C_{27}–C_{29}, C_9	ND	ND	ND	+++	ND	Unknown	Boon and de Leeuw, 1979; Brassell et al., 1980

Notes: TMTD = 2,6,10-trimethyltridecane, TMPD = 2,6,10-trimethylpentadecane. +, ++, +++ = approximate relative abundances corresponding to major, minor, and trace amounts. ND = not detected. NA = not analyzed. OEP = odd/even preference.

Table T15. Identities of hydrocarbon components labeled with codes in Figure F32, p. 78.

Peak	Code	Identification
A	3-ME C_{15}	3-methyltetradecane (*anteiso*-C_{15} alkane)
B	TMTD	2,6,10-trimethyltridecane
C	PR	Pristane
D	PH	Phytane
E	ΔP	Phytenes
F	HMTC	Hexamethyltetracosane
G	$C_{27}\Delta^{4}S$	Cholest-4-ene
H	$C_{27}\Delta^{5}S$	Cholest-5-ene
I	$C_{28}\Delta^{4,22}S$	24-methylcholesta-4,22-diene
J	$C_{28}\Delta^{5,22}S$	24-methylcholesta-5,22-diene
K	$C_{27}\Delta^{17(21)}H$	22,29,30-trisnorhop-17(21)-ene
L	ME $C_{28}\Delta^{17(21)}H$	22,29,30-trisnormethylhop-17(21)-ene
M	C_{30} T	Unknown C_{30} triterpene (dammaradiene?)
N	C_{29} T	Unknown C_{29} triterpene
O	$C_{27}\beta H$	22,29,30-trisnor-17β(H)-hopane
P	$C_{29}\Delta^{4,22}S$	24-ethylcholest-4,22-diene
Q	$C_{29}\Delta^{5,22}S$	24-ethylcholest-5,22-diene
R	$C_{29}\Delta^{4}S$	24-ethylcholest-4-ene
S	$C_{29}\Delta^{5}S + C_{29}\Delta^{17(21)}H$	24-ethylcholest-5-ene + 30-norhop-17(21)-ene
T	$30\Delta^{17(21)}H$	Hop-17(21)-ene
U	$C_{29}\Delta^{3,5}S$	24-ethylcholesta-3,5-diene
V	$C_{30}\alpha\beta H$	17α(H),21β(H)-hopane
W	$\Delta^{8}F$	Fern-8-ene
X	$C_{30}\Delta^{13(18)}nH$	Neohop-13(18)-ene
Y	$C_{29}\beta\beta H$	30-nor-17β(H),21β(H)-hopane
Z	$C_{31}\Delta^{17(21)}H$	22S and 22R homohop-17(21)-ene
a	$C_{31}\alpha\beta H$	17α(H),21β(H)-homohopane
b	$C_{30}\beta\beta H$	17β(H),21β(H)-hopane
c	ME $C_{31}\alpha\beta H$	17β(H),21β(H)-methylhopane
$C_{31}\beta\beta H$	$C_{31}\beta\beta H$	17β(H),21β(H)-homohopane
d	ME $C_{33}\beta\beta H$	17β(H),21β(H)-methylbishomohopane
e	$C_{32}\beta\beta H$	17β(H),21β(H)-bishomohopane
f	ME $C_{34}\beta\beta H$	17β(H),21β(H)-methyltrishomohopane
g	$C_{33}\beta]\beta H$	17β(H),21β(H)-trishomohopane

Note: Pristane = 2,6,10,14-tetramethylpentadecane, phytane = 2,6,10,14-tetramethylhexadecane.

Table T16. Identities of ketone components labeled with codes in Figure F33, p. 80.

Peak	Code	Identification
A	β-T, γ-T	β- and γ-tocopherol
B	U	Unknown
C	$C_{27}\beta S$	5β(H)-cholestan-3-one
D	$C_{27}\beta H$	22,29,30-trisnor-17β(H)-hopan-21-one
E	α-T	α-tocopherol
F	$C_{27}\alpha S$	5α(H)-cholestan-3-one
G	$C_{28}\Delta^{22}S$	24-methylcholest-22-en-3-one
H	ME $C_{28}S$	4-methyl-5α(H)-cholestan-3-one
I	$C_{27}\Delta^{4}S$	Cholest-4-en-3-one
J	$C_{28}\alpha S$	24-methyl-5α(H)-cholestan-3-one
K	$C_{28}\Delta^{4,22}S$	24-methylcholesta-4,22-dien-3-one
L	$C_{29}\Delta^{22}S$	24-ethylcholest-22-en-3-one
M	$C_{29}\beta S$	24-ethyl-5β(H)-cholestan-3-one
N	ME $C_{29}S$	4,24-dimethyl-5α(H)-cholestan-3-one
O	ME $C_{30}\Delta^{22}S$ + $C_{28}\Delta^{4}S$	4,23,24-trimethylcholest-22-en-3-one + 24-methylcholest-4-en-3-one
P	$C_{29}\alpha S$	24-ethyl-5α(H)-cholestan-3-one
Q	$C_{29}\Delta^{4,22}S$	24-ethylcholest-4,22-dien-3-one
R	ME $C_{30}ETS$	4-methyl-24-ethyl-5α(H)-cholestan-3-one
S	$C_{29}\Delta^{4}S$	24-ethylcholest-4-en-3-one
T	$C_{30}T$ + ME $C_{31}\Delta^{22}S$	C_{30} triterpenone + 4,23-dimethyl-24-ethylcholest-22-en-3-one
U	C_{30}ßßH	17β(H),21β(H)-hopanone
V	ME $C^{32}\beta\beta H$ OME	Methyl, methyl-17β(H),21β(H)-homohopanyl ether
W	$C_{27}\Delta^{5}SE$	Alkylcholest-5-enyl ether
X	$C_{28}SE$	Alkyl-24-methylcholestadienyl ether
Y	$C_{27}SE$	Alkylcholest-5-enyl ether
Z	$C_{29}SE$	Alkyl-24-ethylcholestadienyl ether
a	ME $C_{34}\beta\beta H$	Methyl-17β(H),21β(H)-trishomohopan-32-one
b	$C_{33}\beta\beta H$	17β(H),21β(H)-trishomohopan-32-one
c	$C_{29}SE$	Alkyl-23,24-dimethylcholest-22-enyl ether
d	$C_{37:2}ME$	Heptaconta-15,22-dien-2-one
e	9-$C_{29}SE$	Nonyl-24-ethylcholestenyl ether
f	ME $C_{35}\beta\beta H$	Methyl-17β(H),21β(H)-tetrakishomohopan-33-one
g	$C_{34}\beta\beta H$	17β(H),21β(H)-tetrakishomohopan-33-one
h	$C_{38:2}ET$	Octaconta-16,23-dien-3-one
i	ME $C_{35}\beta\beta H$	Methyl-17β(H),21β(H)-tetrakishomohopan-34-one
j	$C_{35}\beta\beta H$	17β(H),21β(H)-tetrakishomohopan-34-one
k	$C_{39:2}ME$	Nonacontadien-2-one

Table T17. Geochemical data collected, Hole 1213A.

Core, section, interval (cm)	Depth (mbsf)	pH	Alkalinity (mM)	Salinity	Cl^- (mM)	SO_4^{2-} (mM)	Na^+ (mM)	Mg^{2+} (mM)	Ca^{2+} (mM)	K^+ (mM)	H_4SiO_4 (µM)	NH_4^+ (µM)	HPO_4^{2-} (µM)	Sr^{2+} (µM)	Fe^{2+} (µM)	Mn^{2+} (µM)	Li^+ (µM)	Ba^{2+} (µM)	H_3BO_3 (µM)
198-1213A-																			
1R-4, 145–150	5.95	7.55	3.3	35.0	552	28.6	472	53.1	10.5	12.2	637	25	6	89	51	144	20	0.4	449
2R-2, 145–150	11.35	7.40	4.0	35.0	560	28.4	479	53.1	11.4	11.9	595	13	4	95	5	110	18	0.3	480
3R-4, 145–150	24.05	7.42	3.9	35.0	559	28.5	479	52.9	11.4	12.2	625	18	2	92	23	85	18	0.7	455
5R-1, 145–150	38.55	7.39	3.9	35.0	561	28.0	479	53.3	11.3	11.7	581	13	1	90	3	88	21	0.3	443
6R-3, 145–150	51.15	7.46	3.3	35.0	561	29.2	480	53.2	12.1	11.9	468	8	1	91	8	35	24	0.2	453

Note: Drilling disturbance appears to have affected the geochemistry of samples.

Table T18. Discrete measurements of *P*-wave velocity for Site 1213.

Core, section, interval (cm)	Depth (mbsf)	Velocity (m/s)
198-1213A-		
1R-3, 104	4.04	1500.1
1R-4, 79	5.29	1484.8
1R-5, 73	6.73	1496.4
1R-6, 41	7.91	1491.0
2R-1, 75	9.15	1497.1
2R-2, 72	10.62	1500.0
2R-3, 70	12.10	1497.8
3R-1, 80	18.90	1490.3
3R-2, 73	20.33	1493.7
3R-3, 78	21.88	1493.1
3R-4, 72	23.32	1537.2
3R-5, 75	24.85	1501.8
3R-6, 77	26.37	1499.5
4R-1, 78	28.28	1499.3
4R-2, 62	29.62	1504.3
5R-1, 63	37.73	1504.0
5R-2, 78	39.38	1495.9
6R-1, 72	47.42	1509.6
6R-2, 77	48.97	1503.0
6R-3, 67	50.37	1507.9
6R-4, 49	51.69	1511.2
6R-5, 28	52.48	1515.5
6R-CC, 5	52.85	4526.9*
7R-1, 6	56.46	1501.0
7R-1, 20	56.60	1541.0
7R-1, 28	56.68	1520.0
7R-1, 46	56.86	1531.8
7R-1, 74	57.14	1515.5
8R-CC, 10	66.20	4472.5*
12R-1, 3	104.63	3408.0†
12R-1, 13	104.73	2893.4†
12R-1, 23	104.83	3053.7†
12R-1, 67	105.27	4892.3*
12R-1, 76	105.36	4767.2*
12R-1, 83	105.43	4873.0*
13R-1, 17	114.47	2414.1†
13R-1, 35	114.65	4647.1*
13R-1, 49	114.79	4425.7*
14R-1, 18	124.08	2775.6†
14R-1, 34	124.24	4693.2*
14R-1, 40	124.30	4768.5*
14R-1, 117	125.07	3159.3†
14R-1, 127	125.17	4835.0*
15R-1, 15	133.55	2898.8†
15R-1, 32	133.72	2058.9†
15R-1, 48	133.88	4761.2*
15R-1, 57	133.97	2477.4†
15R-1, 85	134.25	3289.9†
15R-1, 90	134.30	4931.6†
16R-1, 20	143.30	1837.9†
16R-1, 38	143.48	2923.6†
16R-1, 54	143.64	4930.3*
16R-1, 76	143.86	2572.8†
16R-1, 102	144.12	3170.1†
16R-1, 108	144.18	4779.7*
17R-1, 26	150.96	4695.0*
17R-1, 58	151.28	2964.3†
17R-1, 96	151.66	4847.5*
17R-1, 111	151.81	3018.9†
18R-1, 34	160.64	4789.2*
19R-1, 18	170.18	4349.1*
20R-1, 15	179.75	4610.2*
21R-1, 33	189.63	1770.5†
198-1213B-		
1R-1, 46	190.16	4561.8*
1R-1, 59	190.29	4689.0*
2R-1, 41	199.71	2743.3†
2R-1, 60	199.90	4993.8*
2R-1, 108	200.38	4808.6*
3R-1, 18	209.08	4979.9*
4R-1, 8	218.68	3249.6‡
4R-1, 21	218.81	2547.3‡
4R-1, 66	219.26	4749.3*
4R-1, 86	219.46	4972.0*
4R-1, 124	219.84	3279.7‡
4R-1, 134	219.94	3203.3‡
4R-2, 7	220.17	2572.9‡
4R-2, 17	220.27	3151.8‡
4R-2, 24	220.34	4694.8*
4R-2, 34	220.44	3239.8‡
4R-2, 47	220.57	3218.6‡
4R-2, 70	220.80	4988.0*
5R-1, 13	228.43	3638.9‡
5R-1, 23	228.53	4784.6*
5R-1, 48	228.78	3175.2‡
5R-1, 68	228.98	3308.6‡
6R-1, 3	237.83	2989.6‡
6R-1, 27	238.07	2185.9†
6R-1, 39	238.19	1676.8**
7R-1, 21	247.51	4741.6*
7R-1, 45	247.75	3359.0‡
7R-1, 56	247.86	4793.6*
7R-1, 85	248.15	2739.1‡
8R-1, 20	257.00	3643.1‡
8R-1, 81	257.61	2612.7‡
8R-1, 112	257.92	3593.8‡
9R-1, 15	266.55	2235.5‡
9R-1, 48	266.88	1766.1**
9R-1, 60	267.00	4747.6*
9R-1, 105	267.45	4982.2*
9R-1, 135	267.75	5092.4*
10R-1, 11	276.01	1686.9**
10R-1, 33	276.23	4977.0*
10R-1, 50	276.40	4247.1*
10R-1, 55	276.45	4369.1*
11R-1, 21	285.41	4992.0*
12R-1, 18	294.98	5012.4*
13R-1, 16	304.66	4970.0*
14R-1, 20	314.30	4699.9*
14R-1, 35	314.45	1944.3**
14R-1, 100	315.10	4513.2*
15R-1, 32	324.12	1936.1**
15R-1, 53	324.33	4734.5*
16R-1, 20	333.60	4796.9*
16R-1, 47	333.87	4452.0*
17R-1, 28	343.28	4787.3*
18R-1, 23	352.93	4648.5*
19R-1, 11	362.31	1749.9**
19R-1, 20	362.40	1873.5**
19R-1, 68	362.88	4986.3*
19R-1, 105	363.25	2080.1**
20R-1, 50	372.30	2034.8**
20R-1, 74	372.54	1900.5**
20R-1, 117	372.97	4979.5*
21R-1, 21	381.61	1759.2**
21R-1, 97	382.37	4184.5*
22R-1, 5	391.15	4885.6*
22R-1, 30	391.40	2176.6**
22R-1, 96	392.06	1886.5**
22R-1, 130	392.40	5080.5*
23R-1, 5	400.75	5033.4*
23R-1, 85	401.55	4377.4*
23R-1, 92	401.62	1905.0**
24R-1, 21	410.51	1796.0**
24R-1, 105	411.35	4685.5*
25R-1, 22	420.12	2088.7**
25R-1, 51	420.41	4339.8*
26R-1, 38	429.48	4655.0*
27R-1, 15	438.75	3435.8*
27R-1, 30	438.90	1831.2**
27R-1, 74	439.34	3813.3††
28R-1, 96	448.76	4731.1‡‡
28R-2, 73	449.78	5178.8‡‡
28R-3, 102	451.56	5228.2‡‡
29R-1, 20	453.00	4472.4‡‡
30R-1, 120	458.60	4830.7‡‡
30R-2, 65	459.29	4946.9‡‡
30R-3, 130	461.39	4697.2‡‡
30R-4, 28	461.83	3968.2‡‡
31R-1, 58	467.58	5613.0‡‡
31R-2, 15	468.49	5329.3‡‡
31R-3, 60	470.31	5230.1‡‡
31R-4, 50	471.69	5204.8‡‡
31R-5, 25	472.86	5149.3‡‡
31R-6, 135	475.34	4927.4‡‡
31R-7, 80	476.23	5091.0‡‡
31R-8, 33	477.00	5170.3‡‡
32R-1, 81	477.41	5289.4‡‡
32R-2, 98	479.08	4779.1‡‡
32R-3, 61	480.15	4115.0‡‡
32R-4, 22	481.11	4620.9‡‡
32R-5, 39	482.74	4177.7‡‡
33R-1, 44	486.14	4173.9‡‡
33R-2, 60	487.80	4164.7‡‡
33R-3, 14	488.20	4414.0‡‡
33R-4, 34	489.71	4501.3‡‡
33R-5, 64	491.07	5191.9‡‡
33R-6, 6	491.79	4512.5‡‡

Note: * = chert, † = porcellanite, ‡ = radiolarite, ** = chalk or limestone, †† = hydrothermally altered material, ‡‡ = diabase.

Table T19. *P*-wave velocities for the lithologies recovered from below 60 mbsf, Site 1213.

Lithology	Velocity (m/s)		
	Minimum	Mean	Maximum
Chalk and limestone	1676.8	1887.8	2176.6
Porcellanite	1770.5	2716.7	3408.0
Radiolarite	2235.5	3097.7	3643.1
Hydrothermally altered material	NA	3813.3	NA
Chert	3435.8	4724.4	5092.4
Diabase	3968.2	4804.0	5613.0

Note: NA = not available.